Cosmic String Searches in New Observational Windows

Rebecca Jean Danos

Department of Physics

McGill University

Montreal, Quebec

February 2011

A thesis submitted in partial fulfilment
of the requirements for the degree of Doctor of Philosophy

Doctor of Philosophy

Abstract

Placing observational limits on cosmic strings would provide important confirmation of or constraints on early universe models. Cosmic strings imprint the cosmic microwave background (CMB) with a distinct position space signature, leaving line discontinuities in the temperature maps due to a combination of gravitational lensing and the Doppler effect. To improve theoretical observational constraints, I wrote sky map simulations with and without cosmic strings, edge detection and counting algorithms, and programs to differentiate statistically between the ambient edges due to the inflationary background and the string signals. Our application of position space algorithms, specifically the Canny edge detection algorithm, was highly successful and allowed us to establish improved limits, by more than an order of magnitude, on the contribution of cosmic strings to the total fluctuation spectrum from simulated data.

We extended our analysis of the Canny algorithm to distinguish between abelian cosmic strings and cosmic superstrings through the presence of three-string junctions in cosmic superstring maps. To this end, I wrote the first simulations of maps with junctions and found a disparity in the density of edges in maps of string networks with and without junctions. This work resulted in a statistic to differentiate between different cosmic string models including string theory models and models with different numbers of cosmic strings.

I also modeled the position space polarization signal induced by cosmic string wakes. Due to the gravity of a moving string, matter falls into overdense two dimensional sheets of matter, wakes, behind the string. As photons propagate through the wakes, they encounter this overdensity of ionized matter which can polarize them. In our work we placed the first limits on the CMB polarization signature of cosmic strings including their signature nonlinear structures, wakes, and found they would produce an observable signal

when used in combination with an algorithm such as the Canny algorithm. The cosmic string wakes lead to a gradient in the intensity of polarization in the shape of the wake, greater at earlier positions of the string.

The overdense wakes produced by strings provide more opportunity for the 21 cm hydrogen spin flip as well, so we found that cosmic strings wakes can be observed as three dimensional wedges in maps of 21 cm radiation absorption. Our paper is among the first to study the cosmic string signature in 21 cm and the first to examine the influence of wakes on the 21 cm signal.

Résumé

La mise en place de limites d'observation sur les cordes cosmiques permettraient de confirmer, ou à tout le moins de contraindre de façon importante, les présents modèles de l'Univers primordial. Les cordes cosmiques imprègnent le fond diffus cosmologique (ou CMB) d'une signature distincte dans l'espace, sous forme de discontinuités linéiques dans les cartes de températures. Ces dernières sont dues à une combinaison des effets de lentilles gravitationnelles et de l'effet Doppler. Afin d'améliorer les contraintes observationnelles théoriques, j'ai écris des simulations de cartes du ciel avec et sans cordes cosmiques, des algorithmes de détection et de comptages des lignes de discontinuité, ainsi que des programmes permettant de distinguer de façon statistique les lignes de discontinuité produites naturellement dans le contexte de l'inflation cosmique de celles dues à la présence de cordes cosmiques. L'application d'algorithmes dans le domaine spatial (par opposition au domaine des harmoniques sphériques), en particulier l'application de l'algorithme de détection de discontinuités linéiques Canny, fut très réussie et nous a permis d'établir des limites améliorées de plus d'un ordre de grandeur sur la contribution des cordes cosmiques à l'ensemble du spectre de fluctuations pour les données simulées.

Nous avons étendu notre analyse utilisant l'algorithme Canny pour nous permettre de distinguer les cordes cosmiques abéliennes des supercordes cosmiques en analysant la présence de jonctions de trois cordes dans les cartes de supercordes cosmiques. À cette fin, j'ai écris les premiéres simulations de cartes incorporant ces jonctions et ai constaté une disparité dans la densité de lignes de discontinuité détectée dans les cartes de réseaux de cordes avec et sans jonctions. Ce travail m'a permis d'élaborer un modèle statistique permettant de différencier les différents modèles de cordes cosmiques, y compris les modèles provenant de la théorie des cordes et les modèles avec différents nombres de cordes cosmiques. J'ai aussi modélisé, dans le domaine spatial, le signal de polarisation induit par les sillages de cordes cosmiques. En raison de

la géométrie spécifique de son champs gravitationnel, une corde cosmique en mouvement cause l'accrétion de matière dans des régions de surdensité bidimentionnelles, ou sillages, derrière elle. Lorsque des photons se propagent à travers ces sillages, ils peuvent être polarisés par leur rencontre avec la région de surdensité de matiére ionisée qui s'y trouve. Par notre travail, nous avons imposé les premières limites sur la signature possible laissée dans le champs de polarisation du CMB, en incluant les effets de leur structures non-linéaires, c'est-à-dire de leurs sillons, et trouvé que ces dernières produiraient un signal détectable lorsqu'utilisées de concert avec un algorithme tel que l'algorithme Canny.

Les sillages d'une corde cosmique donnent naissance à un gradient d'intensité dans le spectre de polarisation présent dans la structure des sillages, la polarisation étant plus importante aux points les plus reculés dans l'histoire du déplacement de la corde. Les zones de surdensité produites par les sillages des cordes donnent également lieu à une gamme d'opportunités concernant la raie d'émission à 21 cm de l'hydrogène. Ainsi, nous avons découvert que les sillages de cordes pourraient être observé sous la forme de prismes triangulaires tridimensionnels dans les cartes d'absorption de la raie à 21 cm. Notre article est parmis les premiers à étudier la signature des cordes cosmiques dans le spectre d'absorption de la raie à 21 cm, et est le premier à examiner l'influence possible des sillages sur ce dernier.

Dedication

This thesis is dedicated to Andrew with all my love

Acknowledgements

I would like to thank with all my heart all of the people who have offered their support of me and made this long journey through graduate school possible. First and foremost I would like to thank my husband, Andrew R. Frey, for all of his unceasing support in every possible way for which I cannot express enough my eternal gratitude. Without his belief in me and nurture, completing this degree would be but a dream. Next I would like to thank with all my heart my co-advisors Robert Brandenberger and Keshav Dasgupta for all of their support, advice, discussions, and scientific and personal guidance. I am particularly indebted to the inspired guidance of Robert Brandenberger without which I would not have been able to complete this thesis; I am very grateful for his careful attention and insightful discussions. I am also indebted to Keshav Dasgupta for his understanding and caring encouragement.

I would like to thank those members of the McGill University physics department who made my tenure here memorable and meaningful including Jim Cline, Eddie Del Campo, Fang Chen, Hong Guo, Rhiannon Gwyn, Sangyong Jeon, Alex and Fergus Maloney, Paul Mercure, Guy Moore, Marcus Tassler, Tracy Webb, and Wang Yi. I would also like to thank Andrew Stewart and Stephen Amsel for useful discussions. I would especially like to thank Gil Holder and Matt Dobbs for many pedagogical and helpful discussions and for insightful comments on sections of my dissertation. I would also like to thank Alex van Engelen for useful discussions and comments on sections of my dissertation. I am particularly grateful to Laurence Perreault Levasseur for her careful translation of my abstract into French and useful discussions.

There have been many people who believed in me when I did not, and they deserve my heartfelt thanks. I would like to express my deepest gratitude to Norman Hoffman and Elaine Ransom-Hodges who have offered tremendous support and unending encouragement. I would also like to deeply thank my music teachers Eva Csarnay and Genevieve Levesque who taught me much about the art of living and believing in myself while I've been at McGill which has inspired my scientific endeavors as well as my musical ones.

I also have numerous friends and family who contributed to my experience at McGill University. I would like to thank Aunt Ginny McCloskey for all her optimism and helpful phone conversations, my dear friend Sugumi Kanno for all her caring encouragement and for serving as a mentor and big sister to me. I would also like to thank deeply my UCLA advisor Per Kraus and my internship advisor Ue-Li Pen for all of their support of my career, positive encouragement, and physical insight in stimulating discussions during my tenure at McGill. I would also like to thank my dear friends Anupam Mazumdar, Jonathan McDowell, Natasha Lepore, Judy Wong, and Richard Scalzo for their generous, spirited support and encouragement particularly in challenging times. I would also like to thank Linda and Don Frey who have truly become my family these last few years and who have offered so much understanding for which I am thankful.

I would also like to thank my dear friend Andrea Franke who gave me so much before she passed and always believed in me. Although she did not live to see my second go at graduate school, I remember her spirit and words, and she remains a dear sister in spirit in my heart. I would also like to thank the others who have passed who will not see me graduate Ya Ya and Omi.

I am also thankful for all the love I have received from Alicia, Cobe, and Anna, who have truly been important members of my family.

I would like to thank the people who have served as inspiration for me, who are many, but in particular include Andrew Lange.

During my tenure at McGill University I have received generous financial support from Robert Brandenberger, the Chalk-Rowles Fellowship, the Mary Louise Taylor Fellowship, the Principal's Fellowship, and the McGill University physics department. I am particularly grateful to Robert Brandenberger for supporting my academic travel which has been instrumental in my experience at McGill.

Preface

Statement of Originality

The work in the following chapters is original and published in the refereed journals listed below. Due to copyright reasons, some of the articles in this thesis could not be changed. Therefore to maintain consistency, virtually no changes were made in Chapters 3, 4, 5, and 6.

- **Chapter 3: Danos, Rebecca J.** and Brandenberger, Robert H., "Canny Algorithm, Cosmic Strings and the Cosmic Microwave Background," *Int.J.Mod.Phys. D* **19:**183-217 (2010).
- **Chapter 4: Danos, Rebecca J.** and Brandenberger, Robert H., "Searching for Signatures of Cosmic Superstrings in the CMB," *JCAP* **1002:033** (2010).
- **Chapter 5: Danos, Rebecca J.**, Brandenberger, Robert H., and Holder, Gilbert,"A Signature of Cosmic Strings Wakes in the CMB Polarization,"*Phys. Rev.* **D82**, 023513 (2010).
- **Chapter 6:** Brandenberger, Robert H., **Danos, Rebecca J.**, Hernandez, Oscar F.,and Holder, Gilbert P. "The 21 cm Signature of Cosmic String Wakes", *JCAP* **1006.2514** (2010).

Contribution of Authors

In each of the four papers above that comprise this manuscript based thesis, all of the contributing authors participated in discussions, calculations, and the drafts of the publications. For the paper in Chapters 3, I performed all of the research and programming which formed the basis of this paper and conceived the idea to write a new implementation of the Canny algorithm. I also wrote the majority of the paper. For Chapter 4 I also performed all of the research and programming, particularly inventing the means via a density distribution to distinguish between different types of strings and scaling solutions. I also wrote the entire paper with editing from my collaborator. For the papers in

Chapters 5 and 6, I was involved in all of the calculations, discussions, and contributed to the drafts.

Table of Contents

List of Figures

List of Tables

Chapter 1

Introduction

1.1 Overview

Cosmology is a branch of scientific history — a kind of scientific archaeological study — delving to unearth artifacts of the early universe. This thesis strives to ascertain the theoretical signature of cosmic artifacts, specifically cosmic strings, which, if discovered, would be of monumental import, conclusively demonstrating physics beyond the Standard Model. In this thesis we examine the cosmological traces of cosmic strings from the emerging observational probes of the Cosmic Microwave Background (CMB) in both temperature and polarization as well as the 21 cm redshifted spectrum.

Understanding the nature of the universe has fascinated humanity since humankind's nascent thoughts. Since the days of the ancient Greek philosopher, Heraclitus [152], the question of the existence of the eternal nature of the universe has not been answered. Heraclitus believed that an eternal fire existed, and, perhaps, the relic CMB photons from the Big Bang provide evidence for, if not an eternal fire, the existence of a radiation enduring 13.7 billion years.

We find the roots of cosmology in mathematics, specifically geometry, conceived in Ancient Greek traditions fathered by Pythagoras, which metamorphosed into the equally deductive mathematical tenets of general relativity as brought to light by Albert Einstein. Cosmic strings, proposed artifacts of symmetry breaking, in fact influence the geometry of space-time which results in cosmological imprints. Our goal in this thesis is to discern and quantify these imprints and to create the foundation for future experimental searches for cosmic strings. Although a discovery of evidence for cosmic strings would be of paramount importance, strict constraints of their presence would lead to considerable limits and even the elimination of many popular modern particle physics models.

We shall begin this journey by an introduction to Standard Cosmology and string-inspired cosmology, both of which hinge on the geometry of space and time. We then introduce the conditions, phase transitions, which produce cosmic strings, present a historical perspective of cosmic strings and their early role as a competitive theory to inflation, and finally introduce the observational probes we shall explore in this thesis, namely the CMB in temperature and polarization and the 21 cm redshifted spectrum. In Chapter 2 we present a brief introductory background on CMB and 21 cm physics to set the stage for the four following thesis body chapters presenting original work based on CMB analysis.

In Chapter 3 we present the original paper [52], in which we describe a new code to search for signatures of cosmic strings in CMB temperature maps. This code implements the Canny algorithm, an algorithm designed to search for edges, lines of steep gradients in images. Through the Doppler effect, cosmic string gravity produces such temperature discontinuities in position-space, which is known as the Kaiser-Stebbins effect. After locating edges, the code carries out statistical tests to determine if the edges are due to the presence of cosmic strings. We test the power of our new code to limit the tension of the cosmic strings by simulating and analyzing the simulated data with and without the presence of cosmic strings. Our results indicate sensitivities to the presence of cosmic strings more than an order of magnitude better than those from previous analyses.

Different models produce string networks with different properties. For example, models from string theory, known as cosmic superstrings, often possess three-string junctions which are generically absent in gauge theory models. In Chapter 4, we apply the Canny algorithm developed in [52] to simulated maps with and without junctions. In doing so, we present the first simulations of a toy model for cosmic superstrings. They were first published in our paper, [53]. By examining the density profile of edges, we find that we can distinguish various models of cosmic strings. This includes determining the presence of junctions as well as distinguishing among models with different numbers of cosmic strings per Hubble volume. This distinction is still possible but becomes more difficult in the presence of the dominant inflationary signal.

Chapter 5, based on [54] gives the first calculation of the CMB polarization signal due to the nonlinear structures of cosmic string wakes. Moving strings generate overdense regions, or wakes, in wedges behind the string. In brief, we find that ionization in wakes results in extra polarization in rectangular patches on the sky. The polarization signal is largest for string wakes produced at the earliest post-recombination time and also when CMB photons cross the wake soon after it begins to form. The nonlinear nature of the wake produces equal amounts of both types of polarization (E- and B-modes to be defined later), which is a distinct signature compared to polarization produced by inflationary perturbations. Cosmic string wakes can produce a polarization of up to 0.06μK in patches of a degree in scale for wakes laid down soon after recombination with string tensions of approximately $G\mu = 10^{-7}$.

In Chapter 6, we consider an emerging observational probe, the redshifted 21 cm spectrum. Following [29], we present the first calculation of the 21 cm signal from cosmic strings including wakes. In this paper we found that a cosmic string wake, for string tensions corresponding to approximately the present upper bounds, will possess a kinetic gas temperature of $T_K = 20$K and a differential brightness temperature signalling an absorption of $\delta T_b \simeq -160$ mK when observed at a redshift of $z+1 = 30$. The 21 cm emission or absorption from the wake, like the polarization signal, covers a rectangular region on the sky. Including redshift as a third dimension, the wake appears as a wedge with the string at the tip.

Finally, in Chapter 7, we summarize our results and suggest related future work.

1.2 Standard Cosmology

It seems universally accepted that there are three fundamental principles upon which standard cosmology is based: Hubble expansion, the nearly isotropic black body CMB, and nucleosynthesis [25]. These principles lead to the cosmological Standard Model. The questions that demand precise answers beyond the Standard Model include the nature and existence of dark matter, dark energy, and origin of structure [58].

In this thesis we shall not be concerned with the nature of nucleosynthesis, which is the study of the formation and abundances of light elements from thermonuclear fusion several minutes after the Big Bang. Studies indicate that theoretical models, based on early densities of baryons, are consistent with current baryon density measurements in old, high redshift and hence metal-poor objects, scaled according to the universe's expansion [58].

The universe's expansion was discovered in 1929 by Edwin Hubble who found a proportionality between the radial velocities of galaxies and their distances from Earth. This relation, dubbed Hubble's law, can be stated as

$$\boldsymbol{v} = H_0 \boldsymbol{r}, \tag{1.1}$$

in which H_0 is the Hubble parameter. In fact, what Hubble found was a relationship between galactic redshifts and their distance from Earth,

$$z = \frac{H_0 r}{c}, \tag{1.2}$$

but, when the binomial expansion is performed twice on the relativistic Doppler shift equation, this reduces to $z = \beta = v/c = H_0 r/c$ which implies that $v = H_0 r$, where v is the radial velocity of the light source and r is the galaxy's distance from Earth [153]. The Hubble constant has units of $[H_0] = [\frac{v}{r}] = kms^{-1}Mpc^{-1}$ with a value measured in the WMAP seven-year data as of 70.2±1.4 km/(s MPc) [100].

The Hubble expansion is interpreted as an expansion of the space-time background. To understand the expansion of space, we define comoving displacements, Δx_c, which are constant in time, typically defined as the physical distance between objects in the present era. To calculate the physical distance between objects at a different era we multiply the comoving displacement by the scale factor $a(t)$:

$$\Delta x_p = a(t)\Delta x_c, \tag{1.3}$$

so that the distance r_{12} between two objects is

$$r_{12}(t) = \frac{a(t)}{a(t_0)} r_{12}(t_0). \tag{1.4}$$

By using this relation in which r_{12} is the distance between two galaxies, differentiating to yield the velocity, assuming zero peculiar velocity, and inserting the definition of r_{12}, we see the relationship between the scale factor and the Hubble parameter,

$$\left.\frac{\dot{a}(t)}{a(t)}\right|_{t=t_0} = H_0. \tag{1.5}$$

Alternatively, it is easy to see, given the definition of redshift as $z = (\lambda_{now} - \lambda_{original})/\lambda_{original}$ that

$$\frac{1}{a} = \frac{\lambda_{now}}{\lambda_{original}} = 1 + z. \tag{1.6}$$

The dynamics of the scale factor plays a key role in our understanding of the expansion and evolution of the universe. General relativity plays an important role in this story as promised in the overview. In fact general relativity relates intimately to the scale factor. In a flat expanding universe we essentially have a Minkowski metric in which the distance matrix diagonal elements are replaced by the square of the scale factor, which gives us the

Friedmann-Robertson-Walker (FRW) metric:

$$g_{\mu\nu} = \begin{pmatrix} -1 & 0 & 0 & 0 \\ 0 & a^2(t) & 0 & 0 \\ 0 & 0 & a^2(t) & 0 \\ 0 & 0 & 0 & a^2(t) \end{pmatrix}. \tag{1.7}$$

In fact, the crucial equations that describe the dynamics of an expanding, homogeneous, and isotropic universe are the Friedmann-Robertson-Walker (FRW) equations, derived from the Einstein equations, with the continuity equation [25]. The Einstein equations connect the geometry (and expansion) to the energy density and pressure of the universe. In the remainder of the section we shall follow [40] and give a heuristic understanding of the FRW equations.

The Einstein equations can be derived from an action constructed from a scalar that contains second derivatives of the metric. Hilbert found a suitable action constructed from the Ricci scalar R, known as the Einstein-Hilbert action,

$$S_H = \frac{1}{16\pi G}\int \sqrt{-g} R d^4x. \tag{1.8}$$

in which

$$g = \det(g_{\mu\nu}), \tag{1.9}$$

and

$$R = g^{\mu\nu} R_{\mu\nu} \tag{1.10}$$

and $R_{\mu\nu}$ is the Ricci tensor. When the full action, which is the sum of the Einstein-Hilbert and matter actions, is varied with respect to the metric, the resulting equations are the Einstein equations

$$G_{\mu\nu} = R_{\mu\nu} - \frac{1}{2} R g_{\mu\nu} = 8\pi G T_{\mu\nu}. \tag{1.11}$$

in which the Einstein tensor is $G_{\mu\nu}$ and G is Newton's constant. The energy-momentum tensor is defined as

$$T_{\mu\nu} = -2\frac{1}{\sqrt{-g}}\frac{\delta S_M}{\delta g^{\mu\nu}}, \tag{1.12}$$

the variation of the matter action with respect to the metric. We see that the left hand side of this equation describes the geometry of the universe which relates to the right hand side containing information on the matter content of the universe.

The Cosmological Principle, or the Copernican Principle, states that the universe possesses the mathematical properties that it is isotropic (non-varying around a point in all directions) on large scales at every point and is hence homogeneous (the metric does not vary throughout the manifold), confirmed by the near isotropy of the CMB. The space-time metric that satisfies these conditions, though allows only spatial symmetry and not temporal symmetry, is the Robertson-Walker metric

$$ds^2 = -dt^2 + a^2(t)\left[\frac{dr^2}{1-\kappa r^2} + r^2 d\Omega^2\right] \tag{1.13}$$

such that the curvature parameter is $\kappa = k/R^2$ (in which the comoving curvature radius is R and $k \in (+1, -1, 0)$) and the coordinates r, θ, and ϕ are the comoving spherical coordinates in which $d\Omega = d\theta^2 + \sin^2\theta d\phi^2$.

Using the derivatives of the metric we get the Ricci tensor and scalar (the left hand side of the Einstein equation) and assuming a perfect fluid ($T^{\mu}{}_{\nu} = \mathrm{diag}(-\rho, p, p, p)$) for the energy-momentum tensor give the Einstein equations for this metric, known as the Friedmann equations:

$$\left(\frac{\dot{a}(t)}{a(t)}\right)^2 = H(t)^2 = \frac{8\pi G}{3}\rho(t) - \frac{\kappa}{a(t)^2} \tag{1.14}$$

and

$$\frac{\ddot{a}(t)}{a(t)} = -\frac{4\pi G}{3}(\rho(t) + 3p(t)). \tag{1.15}$$

Combined with the continuity equation and the equation of state we have the necessary equations to express the universe's evolution and dynamics. The continuity equation is

$$\frac{\dot{\rho}}{\rho} = -3(1+w)\frac{\dot{a}}{a}, \tag{1.16}$$

which can be derived from the first law of thermodynamics or conservation of energy. The parameter w is defined through the equation of state,

$$p = w\rho, \tag{1.17}$$

where p is pressure and ρ is energy density. For matter $w = 0$, for radiation $w = 1/3$, and for Λ $w = -1$.

In the rest of this thesis we assume zero spatial curvature, $\kappa = 0$, consistent with current observations of a flat universe.

1.2.1 Cosmological Constant

In this subsection we follow [40].

If the action includes a Lorentz-invariant constant, $-\Lambda/(8\pi G)$, then the Einstein equations become

$$R_{\mu\nu} - \frac{1}{2}Rg_{\mu\nu} + \Lambda g_{\mu\nu} = 8\pi G T_{\mu\nu} \tag{1.18}$$

in which there is a new term. If we consider a matter Lagrangian with an added vacuum energy density term, this would shift the energy-momentum tensor, derived by the variation of the action, by a term $-\rho_{vac}g_{\mu\nu}$. Since both an arbitrary constant and a vacuum energy density term affect the Einstein equations in equivalent ways, we can associate the constant term, or cosmological constant Λ, with the vacuum energy related by

$$\rho_{vac} = \frac{\Lambda}{8\pi G}. \tag{1.19}$$

1.3 Inflationary Cosmology

Inflation is a theory in which there is a period of exponential growth of the scale factor in the very early universe. This means, precisely, that in the inflationary scenario

$$a(t) = e^{Ht}. \tag{1.20}$$

The scale factor's growth could be driven by an effective cosmological constant in the action. Inflation was hypothesized to resolve several problems with the standard cosmological models, namely the flatness, horizon, monopole, and structure formation problem.

The flatness problem arises from the scaling of the curvature term compared to the scaling of the energy density term in the Friedmann equation. The matter energy density scales as a^{-3} and the radiation energy density scales as a^{-4} whereas the curvature scales as a^{-2}. Hence, as the universe evolves the curvature term eventually dominates over matter and radiation. Since curvature has not been observed, the curvature parameter would need to be unnaturally small in the very early universe, forming a fine-tuning problem. During an inflationary period, all three of these terms are exponentially suppressed due to the large growth of the scale factor. While the other terms approach zero, Λ remains a constant. At the end of the period of inflation the energy from Λ is injected into radiation and matter and not curvature, hence keeping the curvature term small in comparison at the end of inflation.

The horizon problem stems from the observation that the CMB is homogeneous on large scales despite that no signal could have crossed the visible universe within the age of the universe under standard cosmological assumptions. Inflation resolves this issue by hypothesizing that at an early era all of the currently observed universe was contained in a small patch in causal contact and that the rapid expansion of space-time caused the universe to grow large.

As we discuss later in this chapter, phase transitions can produce topological defects. A Grand Unified transition would produce a copious number of monopoles, types of topological defects, that are not observed today and which would overclose the universe. This could be remedied by inflation, which exponentially dilutes their number density.

Finally, the structure formation problem is that observers see specific unexplained patterns on super horizon scales on the sky [25]. The structure formation problem questions the cause of the deviations from homogeneity.

Inflation postulates that quantum fluctuations produce this deviation which is then expanded to form large scale perturbations, such as seen as low multipole moments of the CMB power spectrum.

The inflaton is the name given to the scalar field which drives inflation. For example, if we solve the Friedmann equation with a constant energy density, such as with a cosmological constant, then the scale factor grows exponentially as desired by inflation. Varying the Lagrangian for a scalar field yields the Klein-Gordon equations for an FRW metric,

$$\ddot{\phi} + 3H\dot{\phi} + \nabla^2\phi + \frac{dV}{d\phi} = 0, \tag{1.21}$$

where $V(\phi)$ is the potential energy density of the scalar field. This field can be separated to a classical part (unperturbed) and a quantum part (a small perturbation), which to first approximation is a free scalar field,

$$\phi(\boldsymbol{x}, t) = \phi(t) + \delta\phi(\boldsymbol{x}, t). \tag{1.22}$$

For most models of inflation the second order and higher correlation functions obey or are dominated by Gaussian statistics because the fluctuations are nearly free scalar fields. Hence, inflation produces Gaussian fluctuations.

Furthermore, the inflationary perturbations are scale-free, meaning they have equal power on all scales [194]. This is because the quantum fluctuations that cause the fluctuations in the gravitational potential are the same at all scales, due to the universe being in a steady state. The universe is in a steady state during inflation since the Hubble and cosmological constants remain constant, implying that the energy density remains constant as well. Since the Hubble constant governs the physics of fluctuations, and the Hubble constant remains essentially unchanged throughout inflation, then the amplitude of a fluctuation with a given physical wavelength is constant in time throughout the inflationary period. However, two perturbations with equal physical wavelength at different times will possess unequal comoving length scales, which is what we would observe as the physical wavelength today ($a_0 = 1$). We do not observe scale invariance in the CMB today because the perturbations cause matter to clump under the influence of gravity and the pressure of the baryon fluid. Hence, the universe after inflation is no longer in the steady state. Please see further details in Chapter 2.

1.4 Introduction to Phase Transitions and Cosmic Strings

This section roughly follows [28].

Many modern theories of particle physics assume a unification of the strong with the electroweak interactions, dubbed the Grand Unified Theory (GUT). In this scenario, the matter action (and thus the potential) is symmetric under an internal symmetry group, meaning it is not a symmetry of spacetime but a symmetry of the fields. The cooling of the universe due to its expansion leads to phase transitions which break the symmetry.

Let us review this scenario further. Let us assume there exist in the universe two scalar fields, ϕ and χ with a cross coupling $g\phi^2\chi^2/2$ and a symmetric double well potential for ϕ in the zero temperature Lagrangian. Suppose that χ can interact with other fields, hence allowing it to be in thermal equilibrium. This gives a simple effective potential which we obtain by replacing χ with T,

$$V(\phi, T) = \frac{1}{2}(gT^2 - \mu^2)\phi^2 + \frac{\lambda}{4}\phi^4. \tag{1.23}$$

We note that this potential possesses a symmetry such that

$$V(\phi) = V(-\phi). \tag{1.24}$$

When $\phi = 0$ the symmetry is maintained. There exists a critical temperature,

$$T_c = \frac{\mu}{\sqrt{g}} \tag{1.25}$$

above which there is a stable ground state and symmetry is preserved. As the universe expands and hence cools, T decreases below the critical temperature. Now the lowest energy state is no longer $\phi = 0$, and the symmetry is broken.

This simple model captures the essential physics of symmetry breaking as the temperature decreases. In the GUT scenario there may be one or more stages of symmetry breaking.

We rename the minimum of the potential $\phi_{min} = \eta$ and find that, at zero temperature,

$$\mu^2 = \lambda\eta^2 \tag{1.26}$$

($\phi = 0$ is a local maximum). Substituting in the first expression into the potential,

$$V = -\frac{\lambda}{2}\eta^2\phi^2 + \frac{\lambda}{4}\phi^4. \tag{1.27}$$

However, the expectation value $\langle\phi\rangle = \eta$, so particles come from small perturbations or oscillations around the minimum, $\delta\phi$. Given,

$$\phi = \eta + \delta\phi \tag{1.28}$$

we can rewrite the potential perturbatively as

$$V = -\frac{\lambda}{2}\eta^2(\eta + \delta\phi)^2 + \frac{\lambda}{4}(\eta + \delta\phi)^4. \tag{1.29}$$

The linear part of this equation in $\delta\phi$ vanishes leaving (up to second order in $\delta\phi$)

$$V = -\frac{\lambda}{4}\eta^4 + \lambda\eta^2(\delta\phi)^2. \tag{1.30}$$

The mass of fluctuations about the symmetry breaking minimum hence is given by

$$m^2 = \lambda\eta^2, \tag{1.31}$$

and the constant term,

$$-\frac{\lambda}{4}\eta^4, \tag{1.32}$$

gives the height of the bump of the potential.

Figure 1.4 illustrates $V(\phi)$ and how, as the temperature decreases, the scalar field, represented by a ball, rolls from $\phi = 0$ to the minimum of the double well potential, the true vacuum. This is the symmetry breaking which results from a phase transition.

Figure 1.1: Symmetry breaking to a true vacuum

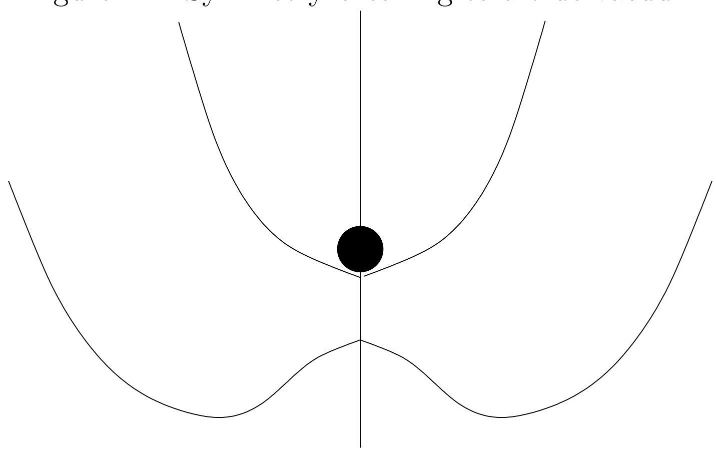

There are two types of phase transitions, first order phase transitions and second order phase transitions. The phase transition we just discussed is a second order phase transition and is also the type of phase transition typically discussed to produce cosmic strings. In a second order phase transition we see that the transition is smooth as the scalar field rolls down the potential as the temperature decreases. Furthermore, in a second order phase transition, $\langle\phi\rangle$ evolves continuously in time and homogeneously in space, except for the boundaries at which topological defects can form.

A first order phase transition leads to discrete bubbles that experience the phase transition at different times and in different places. In a first order phase transition the origin is still a local minimum for the scalar field and is a metastable vacuum state. Below the critical temperature, quantum fluctuations can cause the scalar field to tunnel in nucleating bubbles from the false vacuum to the true vacuum state. In a first order phase transition, $\langle\phi\rangle$ evolves discontinuously in time and inhomogeneously in space.

To generate a prototype potential for cosmic strings, we need to allow for ϕ to be complex and to rotate the double well potential in the resulting complex ϕ plane. Such a symmetric potential, the Mexican hat potential, is given by

$$V(\phi) = \frac{\lambda}{4}(\bar{\phi}\phi - \eta^2)^2 \tag{1.33}$$

which is invariant under $U(1)$ transformations,

$$\phi(x) \rightarrow e^{i\alpha}\phi(x). \tag{1.34}$$

However, even though the potential (and action) is symmetric, the ground state is not symmetric since under a $U(1)$ transformation,

$$\langle 0|\phi|0\rangle = \eta e^{i\theta} \rightarrow \eta e^{i(\theta+\alpha)}, \tag{1.35}$$

in which θ is an arbitrary phase factor. The fact that the ground state is not symmetric is known as symmetry breaking.

The Kibble mechanism arises from the causal nature of symmetry breaking. Above, we have discussed the symmetry breaking which leads to phase transitions. Consider a Mexican-hat potential in which the vacuum manifold is the set of points lying in the circle that traces the minimum of the potential. Causally disconnected regions of space must have different values of the scalar field on the vacuum manifold. Hence, the scalar field is at different locations along the circle (field space) at different spatial points. There is a probability of order one that if we follow some closed path in position-space on super-Hubble scales, we will trace out a full winding of the circle in the vacuum manifold. Given such a situation, consider shrinking the radius of the path. Since the field is continuous, at some point the field must shrink to zero, rolling over the central bump in the potential. This increase in potential, or trapped energy density, is the cosmic string. Hence, in the cores of topological defects the value of ϕ is not on the vacuum manifold and $V(\phi) > 0$. The Kibble mechanism states that there will be at least one cosmic string per Hubble volume which results in a network [96, 97]. In a model which admits cosmic strings, such strings will inevitably arise. We shall explore the network properties and evolution in brief in the next section.

The Compton wavelength determines the width of the cosmic string core [187]. Hence the width is

$$r \sim \frac{1}{m} \sim \frac{1}{\sqrt{\lambda}\eta}, \tag{1.36}$$

while the energy density is given by the difference in the potential between the maximum and minimum of the bump

$$\rho_{cs} = V(0) - V(\eta) \sim \lambda\eta^4. \tag{1.37}$$

The string tension can be found by integrating the energy density over the cross sectional area of the string, hence

$$\mu = \int \rho dA \sim \eta^2. \tag{1.38}$$

We therefore see that the string tension is given by the energy breaking scale in a GUT theory. The string tension is usually expressed as a dimensionless quantity

$$G\mu \sim (\eta/M_{Pl})^2 \sim (10^{16}/10^{19})^2(GeV/GeV)^2 \sim 10^{-6} \tag{1.39}$$

for the simplest GUT models. Since this value for the string tension is larger than current observational limits, we see that it is ruled out that such a GUT scenario contains cosmic strings. Cosmic strings are viable in more complicated GUTs and can be produced copiously in string theory scenarios, for example during reheating at the end of brane inflation.

Other types of topological defects include monopoles, domain walls, and textures. Monopoles are zero-dimensional (point-like) topological defects that form when potentials with three-dimensions in field space have broken symmetry. As in the Kibble mechanism for cosmic strings, after symmetry breaking there must be points in space where the field sits at the top of the potential. This is the trapped energy of the monopole. If one monopole is produced per Hubble volume at the time of GUT symmetry breaking, we would still expect a relic density of about one per cubic meter [194]. Since the mass is essentially the symmetry breaking scale $\eta \approx 10^{16}$GeV, this would be inconsistent with observational cosmology due to dominating over all other energy densities in the universe. One property of monopoles that can result from GUT breaking to the Standard Model is a pattern of radial magnetic fields pointing out of the monopole, in other words a magnetic monopole charge.

Domain walls are two-dimensional topological defects resulting from a one-dimensional double well potential. Their field varies only in one direction implying that there is trapped energy density in a two-dimensional wall. They are problematic in cosmology because their energy density does not redshift fast enough with the universe's expansion, so they dominate over matter and radiation.

Domain walls and monopoles pose cosmological problems because their energy density is so great that the universe will be overclosed, meaning their energy would dominate and $\rho/\rho_{crit} > 1$ so that the universe would be closed. Domain walls and monopoles also pose problems for nucleosynthesis. If monopoles and domain walls form, a mechanism must exist to destroy them, or as in the case of inflation, dilute them.

The other topological defects we have discussed already possess winding number which implies they are stable. Textures are defects localized in space and time which arise from potentials with three-dimensional vacuum manifolds. They are notably unstable with energy leaving them as they collapse.

1.5 Cosmic String Physics

In this section we introduce the cosmic string action, following [187], string network properties, following [25, 187], and cosmic string gravity, following [187].

Although cosmic string solutions arise from the full Lagrangian density for a gauge field A_μ and complex scalar field ϕ, found by Nielson and Olsen, most string dynamics can be examined using the Nambu-Goto action. The Nambu-Goto action is typically applied to cosmic strings since we normally consider strings where the curvature radius exceeds the string's core radius by many orders of magnitude. The Nambu-Goto action is equivalent to the area of the cosmic string worldsheet, the surface area the string sweeps out in space-time [187]. This is analogous to the point particle action which is equivalent to the proper time, or proper length, of the worldline, and which has Euler-Lagrange equations that are consistent for a point particle. This action can also be constructed by considering the constituent quantities relevant to cosmic strings and by considering dimensional analysis. The string tension and powers of the worldsheet curvature could give a general action. Since the worldsheet curvature is trivial compared to the string tension, it can be ignored. Hence, we can construct a string action from the string tension (to provide the correct units) and the worldsheet area as

$$S = \int \mathcal{L}\sqrt{-\gamma} d\sigma d\tau = -\mu \int \sqrt{-\gamma} d\sigma d\tau \tag{1.40}$$

in which μ is the string tension and (σ, τ) are the worldsheet parameterization coordinates, and the two-dimensional worldsheet metric is

$$\gamma_{ab} = g_{\mu\nu} \frac{\partial X^\mu}{\partial \sigma^a} \frac{\partial X^\nu}{\partial \sigma^b}. \tag{1.41}$$

The coordinates of the worldsheet in space-time at a given point in the worldsheet are given by $X^\mu(\sigma)$, $\sigma^a = (\tau, \sigma)$, and

$$\gamma = \det(\gamma_{ab}). \tag{1.42}$$

As was stated in the last section, topological defects such as strings are formed via the Kibble mechanism. By causality, if conditions exist such that they can form, there is an imperative that they do form. The correlation length, $\xi(t_c)$, at the time t_c the temperature passes critical, is an approximation for the initial separation distance among defects, and is less than the causal horizon. Hence, for any loop in space with a radius equal to the causal horizon, we should find a cosmic string or cosmic string loop. Numerical simulations estimate that initially the cosmic strings are divided into 80% horizon sized long strings and 20% loops.

Cosmic strings form networks of strings and loops. The loops can contract by gravitational radiation, and the strings can interact to form loops. Strings can also collide and reconnect (intercommutation). Hence, the Nambu-Goto action cannot be applied to a reconnection. Strings can also pass through each other without interacting.

There are several explanations for why cosmic string networks follow a one-scale model, or a scaling solution. An argument following [25] is as follows: suppose $\xi(t)$ is greater than the Hubble length, $\sim t$, then the string network is frozen, since the strings are separated too much to interact. In this case $\xi(t)$ scales at $a(t)$ with the expansion of the universe, either $t^{1/2}$ for radiation or $t^{2/3}$ for matter. Therefore $\xi(t)$ grows more slowly than the Hubble length and eventually the Hubble length will catch up. On the other hand, if ξ is less than the Hubble length, then the strings will intersect and chop off loops very efficiently, reducing the number of cosmic strings and increasing the correlation length (separation between strings). Hence, we see that $\xi(t)$ is driven toward the Hubble length.

Cosmic strings produce scale invariant power spectra. A scale invariant spectrum has constant $\delta M(k)/M(k)$ where δM is the root-mean-square mass fluctuation on a scale of $1/k$ and M is the mass inside that same radius. For a cosmic string, $\delta M \sim \mu t$ (the mass of a single string stretching through a horizon) and $M \sim t^3\rho$ but $\rho \sim 1/t^2$ (from the Friedmann equation). Here we see that $\delta M/M$ is constant where t is the horizon crossing time for the scale associated with k.

To understand how cosmic strings affect spacetime, we consider a time independent metric that is cylindrically symmetric. This will be boost invariant along the axis of the string since the string is boost invariant along the direction of the string. This metric can be given by

$$ds^2 = e^{A(r)}(dt^2 - dz^2) - dr^2 - e^{B(r)}d\theta^2 \tag{1.43}$$

in which the first factor is the product of the radial dependence and the Minkowski component. If we solved the Einstein equations where the stress-energy tensor is given by the string tension multiplied by a radial delta function (since the density is located at the core of the string) and the given metric, we would find that the solution is consistent with $A(r)$ constant and $e^{B(r)} = ar^2$

in which a is a constant,

$$a = 1 - 4G\mu. \tag{1.44}$$

Hence, the metric becomes

$$ds^2 = dr^2 + a^2 r^2 d\theta^2. \tag{1.45}$$

We see that if we travel 2π radians around a circle for this metric we travel a distance $2\pi ar$. Hence there is a deficit angle given by the difference between a and 1:

$$\delta = 2\pi(1 - a) = 8\pi G\mu. \tag{1.46}$$

1.6 String Theoretic Inspired Cosmology

Since this is not a thesis on string theory, we shall only give a conceptual introduction to those points particularly relevant to cosmic strings. In general, string theory is a unified theory of all interactions, dubbed the Theory of Everything (TOE). At present, string theory is the leading candidate for a theory of quantum gravity. String theory provides from first principles the parameters of low energy physics such as the masses and coupling constants of the Standard Model. In practice this is a very difficult problem. Other benefits that string theory provides are 1) renormalizable unions of gravity with the quantum theory (because the finite size of strings spreads out point-like interactions as are illustrated by worldsheets) and 2) the resolution of gravitational singularities (since strings behave differently than point particles in particular geometries) [141].

Since string theoretic interactions become important at high energies and temperatures which can be found in the early universe, it is natural to consider an embedding of cosmology in string theory. In the rest of this section, we will consider models of string cosmology that admit cosmic strings and we shall discuss briefly the physics of three-string junctions, which can be used to distinguish between models of gauge strings and superstrings.

In string theory, the fundamental object is a fundamental string (F-string). We can imagine a long, highly excited fundamental string. In [47], the authors asked if such a cosmic superstring, considering both F- and D-strings, could be stable over the lifetime of the universe. A D-string is either a one-dimensional D-brane, an object on which strings can end, or a higher dimensional brane in which some of the dimensions are compactified to yield a one-dimensional object in the four large spacetime dimensions. The energy to produce cosmic superstrings could arise from reheating at the end of inflation.

One inflationary scenario that gives rise to cosmic strings is brane inflation. In brane inflation, branes and anti-branes (branes with opposite charges) move around in the extra dimensions. The position of the branes provides the inflaton field. In the simplest models the inflaton potential comes from the Coulomb potential between the branes and anti-branes. Since the branes and anti-branes experience a Coulomb force, they experience an attractive force. At the end of inflation the brane and anti-brane pairs annihilate, because they behave like particles and anti-particles. Since the branes carry a $U(1)$ symmetry, the brane annihilation breaks the symmetry, creating cosmic strings, specifically F- and D-strings in the simplest models.

Since a D-string is an object where an F-string can have an end-point, D-strings and F-strings can come together in junctions. At the junction, F- and D-string charges are conserved, so the third string entering the junction must be a (1,1)-string, which is a bound state of one F-string and one D-string. More generally, one can have junctions of (p, q)-strings that are bound states of p F-strings and q D-strings with the string tensions added in quadrature. The angles between strings at a junction are determined by mechanical equilibrium. These junctions influence the network properties of cosmic strings. In particular, [48] found based on numerical simulations that the strings still follow a scaling solution, though with a higher density of strings per Hubble volume.

1.7 Brief Introduction to Cosmological Probes

In this thesis we concern ourselves with three observational windows, namely the temperature and polarization of the CMB as well as the redshifted 21 cm spectrum.

The Big Bang set the expansion of the universe in motion, cooling the initial radiation as the wavelength of photons expanded. Prior to a redshift of $z = 1100$ the universe consisted of a photon-baryon fluid. By a redshift of $z = 1100$, photons were no longer energetic enough to ionize the present hydrogen, signalling the decoupling of matter from radiation. Since these photons could no longer scatter, be absorbed, or emitted by electrons, the imprint of the state of the universe at this era is frozen in the CMB. In 1965 Penzias and Wilson discovered the CMB [132], with an explanation given by Dicke, Peebles, Roll, and Wilkinson [57], which provided the most solid confirmation, besides the expansion of the universe and light element abundances, of the theory of the Big Bang. In 1992 results from the COBE satellite, with 7 degree angular resolution, [167] indicated temperature anisotropies of 10^{-5} in the CMB temperature spectrum. The rich physics of inflation causes these deviations from smoothness. A number of CMB experiments followed COBE. These include small angular scale balloon experiment BOOM/NA and the mobile Chilean telescope, TOCO, [98] which resulted in precursor data to BOOMERanG [56], flying in 1998 with FWHM beam as good as 10 arcminutes. Notably, the NASA space satellite WMAP [15, 14] launched in 2001, with full sky coverage and a resolution as small as 0.21 degrees. Contemporary experiments of WMAP include the ground based small angular scale experiments South Pole Telescope operating since 2007 [151], Atacama Cosmology Telescope also operating since 2007, [101] and more recently the ESA space satellite Planck [175], with full sky coverage and angular resolutions as small as 5 arcminutes, launched in 2009.

With results published in 2000, BOOMERanG measured the amplitude and shape of the first acoustic peak of the CMB temperature anisotropy, caused by the oscillations in the photon-baryon fluid, to unprecedented accuracy [56]. Since cosmic strings are active sources of perturbations that do not produce CMB acoustic peaks, as their effects do not sum coherently throughout the different times of their influence on the CMB even after decoupling, BOOMERanG led to the the elimination of the theory that cosmic strings seeded most structure and provided positive support that the growth of gravitational perturbations via inflation resulted in most large scale structure. However, even shortly after the BOOMERanG results appeared, the importance of potential topological defects in mixed perturbation models, models admitting both inflation and topological defects, indicated that these results did not rule out topological defects [22]. Recent numerical simulations [139] indicate that cosmic strings can contribute at most 7-14% to the temperature spectrum of the CMB. More recent studies [60] indicate comparable constraints consistent with the lower limits for maximum contribution due to cosmic strings. In our work we will explore cosmic string signatures consistent with modern CMB position space in temperature and polarization signals.

Polarization experiments play a key role in more recent CMB endeavors and are based on the idea that various processes, either from primordial inflation or from intervening matter at various eras — such as the first stars at the advent of reionization or such as cosmic strings — between the last scattering surface and the observer, result in a polarization of CMB photons. Just as scalar perturbations in the metric cause density fluctuations that lead to a background of temperature anisotropies in the CMB, quantum fluctuations in the gravitational field can lead to a background of gravitational waves, tensor perturbations of the metric, that affect the pattern of certain types of polarization, specifically B-modes, in the CMB [10].

There are two patterns of polarization, named E-modes and B-modes. In E-modes, the direction of growth of the polarization vector length is at zero or ninety degree angles to the direction of the polarization vector. In contrast, for B-modes, the direction of growth of the polarization vector length is at a forty-five degree angle to the direction of the polarization vector. Further details will be discussed in Chapter 5.

The DASI team discovered the first evidence for CMB polarization, caused by anisotropic photon scattering at the decoupling era, in 2002 [103]. In their landmark experiment, they found the expected consistency between the temperature anisotropies evidenced in acoustic oscillations and the CMB polarization. As was expected due to the available precision, the DASI team only found E-mode polarization and detected zero B-mode polarization. The DASI team compared their polarization data points to the temperature anisotropies at various multipole moments and found that their polarization level was approximately 0.8 of the theoretical prediction of the concordance model. Such a correlation is expected [80, 196, 90], as polarization emerges from Thomson scattering by electrons coupled with a local quadrupole moment, caused either by a temperature anisotropy or by a relative velocity that results in Doppler shifting. Since the Doppler shifting contributes the most to the local quadrupole at decoupling, there is an expected correlation between the peaks of the temperature and E mode polarization spectra — in fact they are expected to be out of phase since the velocity of the density perturbations is greatest when the amplitudes of the density perturbations are minimized. Hence, CMB polarization experiments such as Planck [175], SPTPol [116], and ACTPol [123] usher in a new era probing this powerful observational window that can lead to understanding of reionization and structure formation and could lead to evidence of cosmic strings and new physics.

For work on CMB polarization expectations, see [20, 21, 88, 145]. Detections of polarization following DASI include CBI [146] in 2004 and BOOMERanG [119, 137] in 2005 which both also performed temperature and polarization cross correlations. The WMAP team, in 2003 [12], 2007 [126], and 2010 [100], presented their polarization results from WMAP's polarization-sensitive radiometers. In 2003 [12], WMAP presented evidence for polarization through the cross-correlation between temperature fluctuations and E-mode polarization. The dominant signal reported in [126], which measured the E-mode correlation, results from polarized foreground emission from Galactic synchrotron radiation and thermal dust emission at levels ranging from 0.06μK to 5μK. In comparison, CMB polarization levels are highly model-dependent but can be of the order of 0.3μK for E-mode polarization and 0.1μK for B-mode polarization. WMAP has measured E-mode polarization with high statistical significance, but the expected B-mode polarization lies below the limits measured by WMAP [100]. Specifically, the E-mode polarization signal is detected in cross correlations with the temperature anisotropies; in [100], the WMAP team detected tangential and radial polarization patterns around hot and cold spots of temperature fluctuations.

Other current polarization experiments include the balloon polarimeter EBEX [149], with an expected science flight in 2011. QUaD [68], another polarization experiment, is a ground based bolometer designed to improve upon DASI at the South Pole. The team published results in 2009 of improved parameter constraints and an improved upper limit for B-mode polarization of $0.57\mu K^2$. BICEP [44], is another CMB polarimeter operating at the South Pole. BICEP aims to detect inflationary B-modes from the CMB, and in 2009 published results measuring a zero B-mode spectrum and tensor-to-scalar ratio that constrains inflationary B-modes. Although this list of polarization experiments is by no means exhaustive, it indicates the great activity and interest in this fruitful field of research.

Another emerging observational field is the search for signals of 21 cm transitions in the dark ages. Specifically, 21 cm radiation in the CMB can flip the relative spin of the proton and the electron in the hydrogen atoms, leading to absorption or emission lines observed in the redshifted CMB spectrum.

With their access to three dimensions, with the depth being in redshift space, probes of redshifted 21 cm radiation will unveil the mysteries of the "dark ages" between recombination and reionization and may give us clues to understanding reionization and structure formation. The great advantage is that redshifted 21 cm radiation probes a long period rather than a single moment.

Proposed 21 cm experiments to observe redshifts of about 1, such as the Canadian Hydrogen Intensity Mapping Experiment [129] and the Square Kilometer Array (SKA) [39] would provide the best proposed means to measure baryon acoustic oscillations (BAO), whose characteristic length scale provides us with a "standard ruler." When measured at different redshifts, BAO maps the expansion history of the universe and thus helps us to understand dark energy, an outstanding enigma of cosmology. These experiments are ideal as they probe a range of redshifts higher than optical experiments. Along these lines, cross-correlation studies with the CMB could extract more information from observations.

Already, there has been some success with hydrogen intensity mapping which is the technique such that the collective afterglow of galaxies is studied as opposed to resolved features. In [105], Lah and collaborators detected 21 cm emission to redshift of $z = 0.24$. In 2008, Pen and collaborators [131] found the first evidence for cosmic structure in hydrogen intensity maps. Not long after, in [42], Chang and collaborators performed a three dimensional hydrogen mapping between redshifts of $z = 0.53$ and $z = 1.12$ with the Green Bank Telescope. Hence, as we see, 21 cm mapping has come of age and the next decade will usher in new telescopes with unprecedented precision which could constrain various structure and cosmological star formation models as well as shed light on dark energy models or even provide a means to search for cosmic strings, as we shall see in Chapter 7.

In this thesis we will utilize these observational probes, CMB temperature and polarization and the 21 cm redshifted spectrum, to search signatures of new physics, specifically cosmic strings.

Chapter 2

The Physics of the Observational Probes

2.1 Basic CMB Physics

The state of the very early Universe was one of thermal equilibrium at all points in space. This state of thermal equilibrium is reflected in the blackbody nature of the CMB, since blackbody emission results from objects in thermal equilibrium. A crucial point about black bodies is that their power versus frequency follows a Planck distribution. As the Universe expands, black bodies retain their distribution but the wavelengths stretch, therefore causing a cooling of the power. The CMB wavelengths have stretched to a peak of about 2 mm and cooled to a temperature of 2.725 K.

CMB anisotropies are caused by gravitational potential perturbations as first derived in [154]. Photons falling into and climbing out of gravitational potential wells are blueshifted and redshifted which changes the local temperature. At the end of the inflationary period the spectrum of density fluctuations was scale invariant which was followed by the gravitational collapse of matter. This gravitational collapse of matter with pressure causes the baryon acoustic peaks (or Baryon Acoustic Oscillations (BAO), named after the oscillation of the baryon-photon fluid in gravitational potential wells) and hence the CMB spectrum observed today, which is not scale invariant. Cosmic strings are active producers of scale invariant fluctuations, hence when matter collapses the constant production of perturbations interferes and there would be no coherent BAO peaks.

CMB anisotropies are typically expressed by their spherical harmonic expansion,

$$\frac{\Delta T(\theta,\phi)}{T} = \sum_{l,m} a_{lm} Y_{lm}(\theta,\phi) \tag{2.1}$$

where the a_{lm}s are the expansion coefficients of the spherical harmonics and (θ, ϕ) the polar angles on the sky.

Since the anisotropies can be expressed as tiny temperature differences from the average, T_0,

$$T(\theta,\phi) = T_0 + \Delta T(\theta,\phi) \tag{2.2}$$

and

$$T_0 = \frac{1}{4\pi}\int d\Omega T(\theta,\phi) \tag{2.3}$$

when we substitute in for $T(\theta,\phi)$ in Eqn. 2.3, we find that the temperature differentials sum to zero. Since the ΔT values center around zero, the a_{lm} are also drawn from a distribution centered at zero. Furthermore, since the orientation of the particular temperature multipole is given by m and the Universe is assumed to be isotropic, all the a_{lm}s for a given l have identical probability distributions. Hence, all the a_{lm}s with a given l have an approximately Gaussian probability distribution with a square of the width (standard deviation) given by

$$C_l = \langle |a_{lm}|^2 \rangle. \tag{2.4}$$

The power spectrum of the CMB is usually expressed as $l(l+1)C_l$ plotted against multipole moment, l (the multiplicative factor $l(l+1)$ normalizes the curve).

CMB experiments measure the angular correlation function written as a decomposition into Legendre polynomials by

$$\frac{\langle \Delta T(\theta,\phi)\Delta T(\theta',\phi')\rangle}{T_0^2} = \frac{1}{4\pi}\sum_l (2l+1)C_l P_l(\cos\gamma) \tag{2.5}$$

in which γ is the angle between T and T'.

Starting from first principles, the Boltzmann equation expresses the time evolution of the number density of photons per frequency interval. The rate in time of the number density of photons depends on local temperature variations, related to density fluctuations, as well as changes in the gravitational potential. Integrating the Boltzmann equation along the line of sight results in the theoretical prediction of the CMB power spectrum which is in good consistency with observation [165, 107]. The modelled CMB power spectrum can be seen in Fig 2.1 computed numerically by CAMB [107].

2.2 Cosmic String Effects on CMB

Cosmic strings would change the temperature of the CMB via the Kaiser-Stebbins (KS) effect [89]. We shall derive the KS effect here following [186].

Consider the Earth on one side of a cosmic string piercing through a plane. Then consider a photon from the CMB on the other side of the cosmic string as the Earth as in Figure 2.2. The cosmic string causes a deficit angle of δ, which causes the CMB to deflect by $\delta/2$ on either side of the cosmic string. In the string frame,

$$\boldsymbol{v}_{CMB} = v\cos\left(\frac{\delta}{2}\right)\hat{x} \pm v\sin\left(\frac{\delta}{2}\right)\hat{y}. \tag{2.6}$$

Since the string tension is small, we can impose the condition $\delta/2 \ll 1$ which causes the above to become

$$\begin{aligned} \boldsymbol{v}_{CMB} &= v\hat{x} \pm v\left(\frac{\delta}{2}\right)\hat{y} && (2.7)\\ &= v\hat{x} \pm \frac{v}{2}8\pi G\mu\hat{y}. && (2.8) \end{aligned}$$

Figure 2.1: Simulated CMB Power Spectrum with normalized C_ls as $C_l l(l+1)T_0^2/(2\pi)$ with parameters from CMBall [148], namely $\Omega_b h^2 = 0.0227$, $\Omega_c h^2 = 0.112$, $\Omega_m = 0.26$, $H_0 = 71.8$, $n_s = 0.965$, $w = -1$ (the equation of state for dark energy), $\Omega_\nu h^2 = 0$, $T_{CMB} = 2.726$ (the temperature of the CMB), $Y_{He} = 0.24$, and reionization optical depth, $\tau_{reion} = 0.093$.

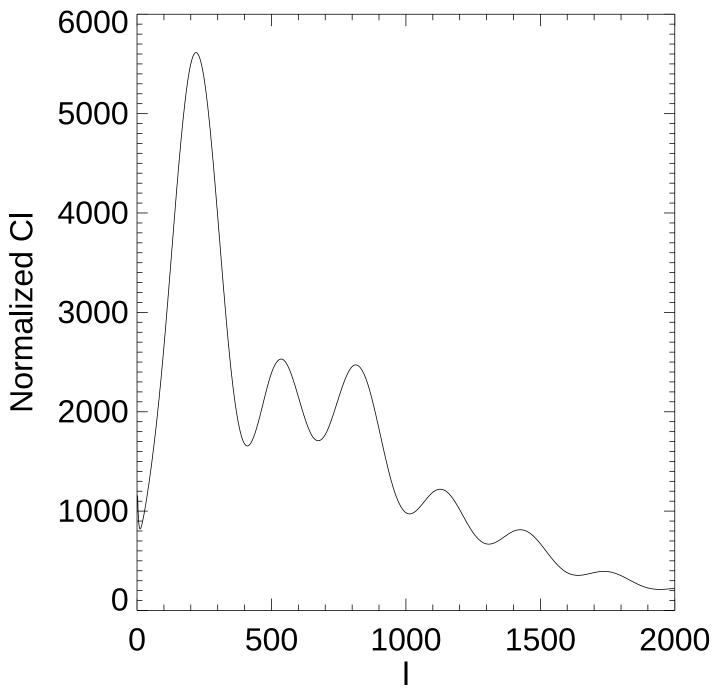

Figure 2.2: The CMB discontinuity caused by the string's deficit angle.

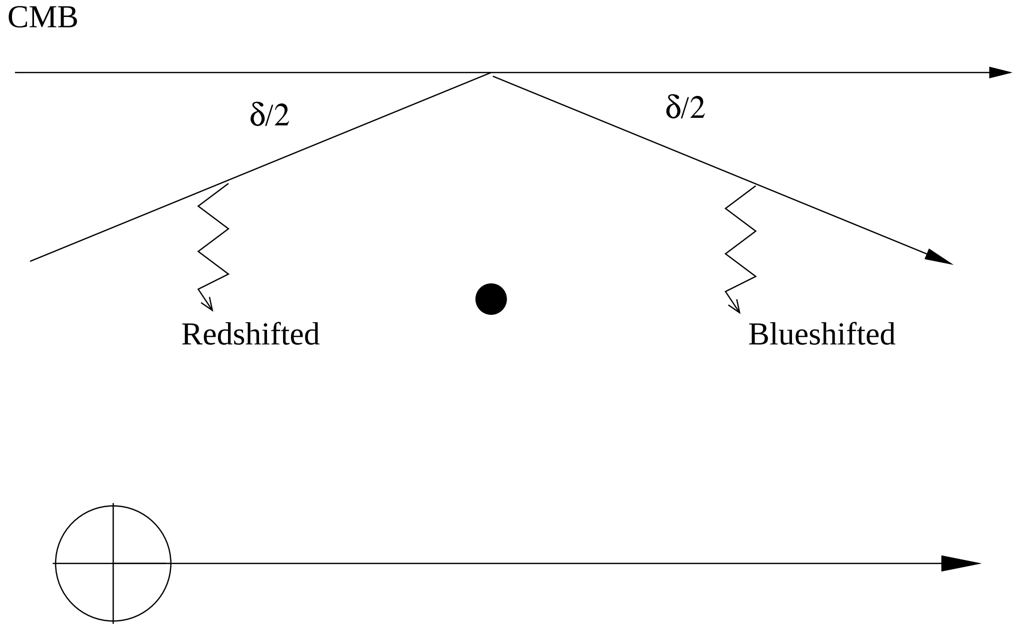

The velocity of the Earth in the string frame is

$$\boldsymbol{v}_E = v\hat{x}. \tag{2.9}$$

In the rest frame of the Earth we boost the velocities from the rest frame of the string. The velocity of the Earth in the rest frame of the Earth is obviously zero. Boosting v_{CMB} we have

$$v'_{CMB} = \gamma v_{CMBy}\hat{y}. \tag{2.10}$$

Then considering the Doppler effect,

$$\frac{\delta T}{T} = \frac{\delta \nu}{\nu} = \frac{v'_{CMB}}{c} = \pm\gamma\frac{v}{c}4\pi G\mu. \tag{2.11}$$

This is the signal on either side of the cosmic string, leaving a total temperature discontinuity as

$$\frac{\delta T}{T} = \gamma v 8\pi G\mu. \tag{2.12}$$

2.3 CMB Polarization

A photon's polarization is the direction of its electric field. Since photons are transverse waves, the polarization will be perpendicular to the direction of its propagation. Following [81] the direction of the electric field vector of a plane wave is its direction of polarization. A monochromatic wave described by

$$\boldsymbol{E}(\boldsymbol{x},t) = (\boldsymbol{\epsilon}_1 E_1 + \boldsymbol{\epsilon}_2 E_2)e^{i\boldsymbol{k}\cdot\boldsymbol{x}-i\omega t} \tag{2.13}$$

can be divided into two perpendicular components,

$$\begin{aligned} \boldsymbol{E}_1 &= \boldsymbol{\epsilon}_1 E_1 e^{i\boldsymbol{k}\cdot\boldsymbol{x}-i\omega t} && (2.14)\\ \boldsymbol{E}_2 &= \boldsymbol{\epsilon}_2 E_2 e^{i\boldsymbol{k}\cdot\boldsymbol{x}-i\omega t} && (2.15) \end{aligned}$$

with polarization vectors $\boldsymbol{\epsilon}_1$ and $\boldsymbol{\epsilon}_2$. E_1 and E_2 are complex numbers. If they are in phase then the wave is linearly polarized. If they are out of phase they are elliptically polarized. Circular polarization is where they have the same magnitude but differ in phase,

$$\boldsymbol{E}(\boldsymbol{x},t) = E_0(\boldsymbol{\epsilon}_1 \pm i\boldsymbol{\epsilon}_2)e^{i\boldsymbol{k}\cdot\boldsymbol{x}-i\omega t} \tag{2.16}$$

Another basis is

$$\boldsymbol{\epsilon}_\pm = \frac{1}{\sqrt{2}}(\boldsymbol{\epsilon}_1 \pm i\boldsymbol{\epsilon}_2) \tag{2.17}$$

A different way to describe the polarization state is to utilize the Stokes parameters, I, Q, U, and V. The Stokes parameters relate to sums and differences of measurable intensities.

In the linear polarization basis, the Stokes parameters for a single plane wave are:

$$\begin{aligned} I &= |\boldsymbol{\epsilon}_1\cdot\boldsymbol{E}|^2 + |\boldsymbol{\epsilon}_2\cdot\boldsymbol{E}|^2 && (2.18)\\ Q &= |\boldsymbol{\epsilon}_1\cdot\boldsymbol{E}|^2 - |\boldsymbol{\epsilon}_2\cdot\boldsymbol{E}|^2 && (2.19)\\ U &= 2Re[(\boldsymbol{\epsilon}_1\cdot\boldsymbol{E})^*(\boldsymbol{\epsilon}_2\cdot\boldsymbol{E})] && (2.20)\\ V &= 2Im[(\boldsymbol{\epsilon}_1\cdot\boldsymbol{E})^*(\boldsymbol{\epsilon}_2\cdot\boldsymbol{E})] && (2.21) \end{aligned}$$

Figure 2.3: Photons from a quadrupole scattering off an electron.

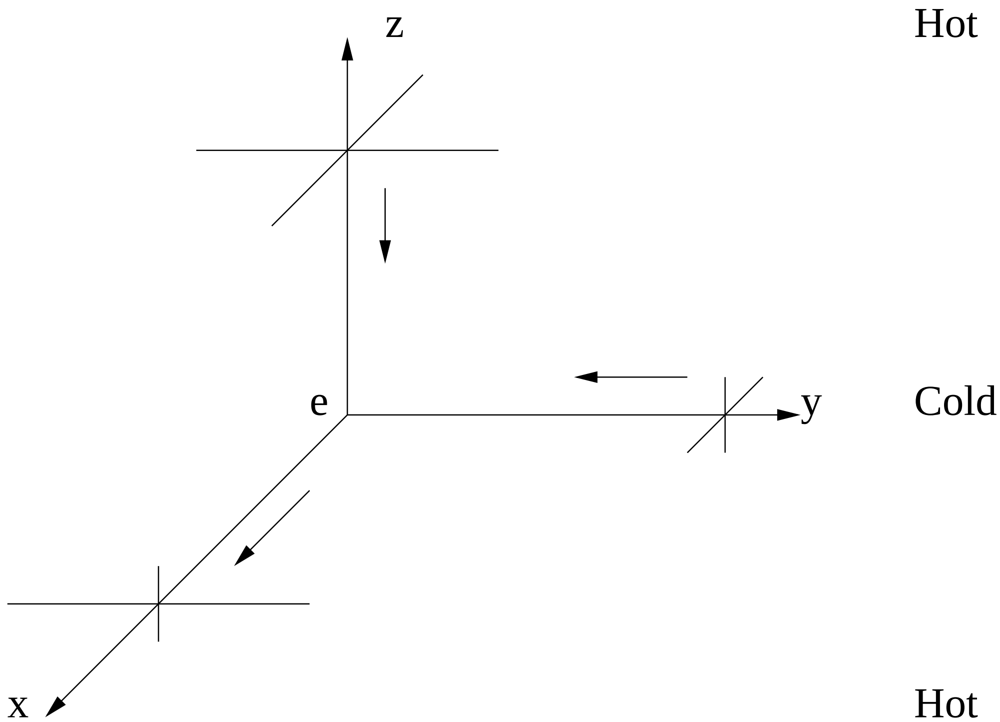

The following explains the Stokes parameters:

- I measures the relative intensity of the wave.
- Q measures how much more intensity is in the x direction than in the y direction
- U and V give the difference in the phases. If $E_1 = a_1 e^{i\delta_1}$ and $E_2 = a_2 e^{i\delta_1}$ $U = 2a_1 a_2 \cos(\delta_2 - \delta_1)$ and $V = 2a_1 a_2 \sin(\delta_2 - \delta_1)$.

On the sky, the Stokes parameters can be associated with each point. The strength of the polarization is given by the polarization amplitude [80],

$$P = \sqrt{Q^2 + U^2}. \tag{2.22}$$

Polarization patterns on the sky can be depicted by their behavior under parity (reflections about an axis). These patterns consist of two types, E-modes and B-modes. E-modes are symmetric under parity, possess the property that the gradient of the polarization amplitude lies either parallel or perpendicular to the polarization vector, and behave like gradients. Scalar (density) perturbations produce only E-modes at linear order. B-modes, which behave like curls, change under parity such that the slopes of their polarization vectors are reversed (negative slopes become positive and vice versa). B-modes possess the property that the gradient of the polarization amplitude lies at a 45 degree angle to the polarization axis. At linear order vector perturbations (in the velocity field of matter) produce E- and B-modes. Tensor perturbations also result in the production of B-modes. We emphasize that the Stokes parameters are a property of each point on the sky, while E- and B-modes describe the pattern of polarization vectors over a region. In position space, E- and B-modes can be derived from integrals of the Q and U Stokes parameters. In Fourier space, the E- and B-modes are local rotations of the Stokes parameters, Q and U.

Thomson scattering in the presence of a quadrupole, the pattern of hot and cold spots from the $l = 2$ decomposition of the CMB temperature in spherical harmonics, produces polarization. Please see Figure 2.3 for the following discussion. The quadrupole pattern has alternating hot and cold spots. For example, consider an electron sitting in the center of a quadrupole in the center of a cold region with hot regions above and below. Then consider that the hot regions are to the positive and negative z-axes and the cold regions lie in the $x - y$ plane. Photons originating from the y direction (cold) will have polarization vectors in the $x - z$ directions and photons originating from the z direction (hot) will have polarization vectors in the $x - y$ directions, since polarization is transverse. If the observer sees the scattered light from the x direction, the polarization vectors will be in the z and y directions. Since a hot photon will have a stronger intensity than a cold one, the z-axis polarization dominates over the y-axis polarization. Hence, the scattered photon is polarized. To first order density fluctuations result in E-mode polarization, although as we shall see at higher orders we can get B-modes as well. Whereas in inflationary models, the B-mode polarization is suppressed compared to the

E-mode polarization, cosmic string wakes contribute equally to the two, as we shall see.

2.4 21 cm Physics

The following review of 21 cm physics follows [65].

The power of the 21 cm redshifted spectrum lies in its ability to probe the "dark ages" of the history of the Universe between redshifts of the era of recombination and the era of reionization. In addition to this obvious advantage, emerging experiments are designed to test its power at even lower redshifts in measuring the length scale of baryon acoustic oscillations to study the dark energy problem.

21 cm radiation is either emitted or absorbed when the hydrogen proton and electron spins flip relative to each other. This absorption or emission is observed in the background CMB radiation. The wavelength of emission or absorption for this transition is a physical wavelength of 21 cm but its comoving wavelength is scaled depending on the redshift of the process.

The quantity that we measure in 21 cm observations is the differential brightness temperature which is the difference or contrast between the brightness temperature, or specific intensity of radiation from the high redshift hydrogen gas clouds, and the CMB at the redshift of the hydrogen gas. The differential brightness temperature, δT, is sensitive to fluctuations in gas number density, gas temperature, and the ionization fraction. It is given by

$$\delta T_b(\nu) = \frac{T_b(\nu) - T_\gamma(\nu)}{1+z} \simeq \frac{T_S(\nu) - T_\gamma(\nu)}{1+z}\tau_\nu \tag{2.23}$$

The second equality follows from expanding the exponential factor in Equation (2.24) below to linear order in the optical depth. In Equation 2.23 the brightness temperature, T_b, expresses the brightness of outgoing photons. This means, precisely, that background radiation with temperature T_γ entering a cloud with spin temperature of T_S and an optical depth of τ_ν will emerge with a temperature given by

$$T_b = T_S(1 - e^{-\tau_\nu}) + T_\gamma(\nu)e^{-\tau_\nu}. \tag{2.24}$$

The optical depth is given by the integral of the absorption coefficient, α_ν along the proper distance ds through the cloud, given by

$$\tau_\nu = \int ds\alpha_\nu. \tag{2.25}$$

The spin temperature gives the fraction of hydrogen in the excited state, or the relative number density of atoms in the hyperfine energy states through

$$\frac{n_1}{n_0} = 3e^{-T_*/T_S} \tag{2.26}$$

in which n_1 and n_0 are the different number densities of atoms in the hyperfine states with weights of 3 and 1 respectively and $T_* = E_{10}/k_B = 0.068K$ is the temperature corresponding to the energy splitting between the two states. The spin temperature depends on the kinetic gas temperature in the hydrogen cloud, coupling coefficients for collisions among free electrons, protons, and other hydrogen atoms, UV scattering, and absorption and emission of CMB photons.

To find the spin temperature, we consider an equilibrium system. Hence, the rate of excitation in hydrogen atoms must equal the rate of deexcitations. The equilibrium rate equation is expressed as an equality between the number of excited atoms that deexcite per unit time and the number of ground state atoms that excite per unit time. This equation is expressed below:

$$n_1(C_{10} + P_{10} + A_{10} + B_{10}I_{CMB}) = n_0(C_{01} + P_{01} + B_{01}I_{CMB}) \tag{2.27}$$

The equilibrium equation accounts for the collisional rate of deexcitation (C_{10}) and excitation (C_{01}). Hence, n_1C_{10} in the above equation expresses the number of atoms that deexcite per unit time due to collisions. The UV scattering, scattering by UV photons, is accounted for by the coefficients P_{10} and P_{01}. The total number per unit time of spontaneously deexcited atoms is given by n_1A_{10}.

B_{10} and B_{01} are the coefficients per atom in the representing the probability of stimulated deexcitation and excitation by CMB photons. Hence, when multiplied by the intensity of the CMB it represents the chance a hydrogen atom in the ground state will be excited upon encountering a CMB photon. These are the Einstein coefficients typically applied in laser physics. Further details can be found in Chapter 6.

Chapter 3

Application of the CANNY Algorithm to CMB Position Space Temperature Maps

3.1 Preface

In this chapter, we include [52], in which we statistically look for the presence of strings in the CMB based on the Kaiser-Stebbins effect. The Kaiser-Stebbins effect leaves a unique imprint of cosmic strings on CMB temperature position space maps. The nearly Gaussian inflationary perturbations dominate the signal, hence we need to look for the effect statistically. We use the Canny algorithm to search for the edges left by cosmic strings per the Kaiser-Stebbins effect and then apply statistics to the edgelengths.

3.2 Introduction

There has been a recent renaissance of interest in cosmic strings (see e.g [55, 156]) as a mechanism contributing to the spectrum of primordial cosmological perturbations and the corresponding anisotropies in cosmic microwave anisotropy (CMB) maps. In part this renewed interest is sparked by the realization that many supergravity models of inflation also lead to the production of strings at the end of the period of inflation [83, 84]. In addition, many models of inflation in the context of string theory predict the formation of a network of strings at the end of the inflationary phase [157]. The conditions under which these cosmic superstrings [193] are stable have been explored in [47]. Cosmic superstrings may also arise in other approaches to superstring cosmology such as the Ekpyrotic scenario [94] or string gas cosmology [34, 121, 31].

If matter is described by a particle physics model which admits stable strings forming after inflation, then by causality it is inevitable that a network of such strings will form during the cosmological phase transition which corresponds to the symmetry breaking which is responsible for the existence of the strings [97, 96]. It is inevitable that the network of strings contains "infinite" strings (strings crossing the entire volume). For applications in cosmology one divides the strings into "loops" (loops of cosmic string with a curvature radius smaller than the Hubble radius $H^{-1}(t)$, where $H(t)$ is the cosmological expansion rate) and "long strings" (infinite strings and loops with curvature radius larger than the Hubble radius). The causality argument [97, 96] (see also [187, 75, 28] for some standard reviews on cosmic strings and structure formation, and [95, 198, 184] for the original references) implies, in fact, that at all times after the phase transition a network of long strings with a correlation length (mean curvature radius) comparable or smaller than the Hubble radius will survive. It can be argued [188, 187, 75, 28] that a network of (non-superconducting) strings will approach a "scaling solution" for which at all late times t the correlation length of the network of long strings is a fixed fraction of the Hubble radius [1] .

Cosmic strings [122] are described by their mass per unit length μ which is usually quoted in terms of the dimensionless number $G\mu$, G being Newton's gravitational constant. A straight string has a tension which is equal in

[1] It is likely that the distribution of cosmic string loops also approaches a scaling solution; see e.g [4, 16, 5] for early simulations of cosmic string networks supporting the conclusion that the distribution of loops also scales, [191] for an opposing view based on field theory simulations and [183, 113, 150, 120, 143] for more recent work supporting scaling for string loops.

magnitude to μ. Hence, the effective action which describes the motion of a straight string is the Nambu-Goto action, the same action which describes fundamental strings. Since cosmic strings carry energy, they will lead to density fluctuations and cosmic microwave background (CMB) anisotropies.

The network of cosmic strings will generate a scale-invariant spectrum of cosmological perturbations [180, 158, 171]. More relevant to the current paper, cosmic strings generate a very specific signature in cosmic microwave background anisotropy maps, namely line discontinuities [89]. These line discontinuities arise since space perpendicular to a cosmic string is a cone with deficit angle given by [185]

$$\alpha \, = \, 8\pi G\mu \, . \tag{3.1}$$

Since the motion of cosmic strings is relativistic, photons passing on different sides of the string moving with a velocity v perpendicular to the plane spanned by the string direction and the line of sight between the observer and the string will be seen by the observer with a relative Doppler shift

$$\frac{\delta T}{T} \, = \, 8\pi\gamma(v)vG\mu \, , \tag{3.2}$$

where $\gamma(v)$ is the relativistic gamma factor (see Figure 3.1). Looking in direction of the string, we will see a line in the sky across which the CMB temperature jumps by the above amount. We will denote this effect, the Kaiser-Stebbins effect, as the KS effect in the rest of the paper.

The conical deformation of space induced by a "long" cosmic string has a length of the order the Hubble radius, i.e. of the order of t in direction of the string. Since cosmic strings are formed in a phase transition and the effects of the transition travel with the speed of light, the depth of the region affected by the string (in direction perpendicular to the string) is t, as shown in [112].

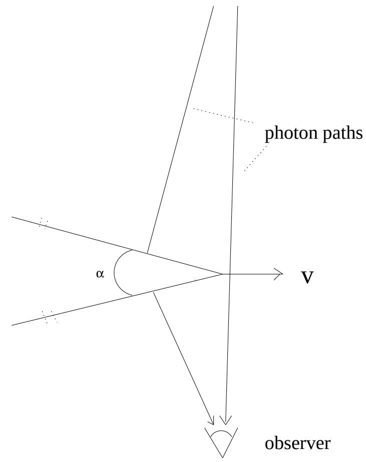

Figure 3.1: Geometry of the Kaiser-Stebbins effect: Photons passing on the two sides of the moving cosmic string obtain a relative Doppler shift for the observer who is at rest.

Hence, each string between t_{rec} and t_0 whose "zone of influence" [2] is intersected by the past light cone of the observer will induce a line discontinuity in the CMB temperature map with length gt, where g is a random number in the interval $0 < g < 1$ which takes into account the random angle of the velocity vector of the string relative to the plane determined by the string direction and the observer's line of sight to the string. The anisotropy pattern induced by a single string segment contains several edges. There is the central line discontinuity (3.2) coming from photons which pass on different sides of the string. Since the deficit angle in Figure 3.1 has finite depth (in direction $-v$), as explained in the previous paragraph there will be two edges (again sharp because the deficit angle sharply decreases to zero [112]) with half the value of δT. Finally, our modelling of the string network in terms of straight segments introduces the sharp "boundary" edges perpendicular to the central edge (see also Figure 3.3).

[2] By which we mean the region of space which is deformed due to the presence of the string.

To detect the line discontinuities in CMB maps produced by cosmic strings, it is important to have small angular resolution. Strings present in the universe between the time of last scattering and the present time contribute to the signal. However, according to the cosmic string scaling solution, the most numerous strings are those present at or shortly after last scattering. The Hubble radius at that time subtends an angle of about 1.8^o. If the angular resolution is not much smaller than this angle, then the anisotropies produced by these strings will not be distinguishable from anisotropies produced by Gaussian noise with the corresponding coherence length. On the other hand, full sky coverage is not essential. Thus, ground-based small angular resolution surveys such as ACT [102] or the South Pole Telescope [151] both of which have angular resolution of about $1^{\prime}$ are ideal to search for strings. The Planck satellite experiment [190, 125] with an angular resolution of about $5^{\prime}$ will also yield a good data set to use, in particular since the systematic errors in the data will likely be smaller.

The KS effect is a part of the "Integrated Sachs-Wolfe" [155] contribution to CMB anisotropies. The primordial cosmological fluctuations produced by strings also contribute to the regular Sachs-Wolfe effect. In contrast to cosmological fluctuations produced in inflationary cosmology, those produced by cosmic strings are "incoherent" and "active" as opposed to "coherent" and "passive" [3]. The string network is continuously seeding growing curvature fluctuations on super-Hubble scales, and therefore the fluctuations enter the Hubble radius not as standing waves. As a consequence, the angular power spectrum of CMB anisotropies does not have [135, 111, 130] the acoustic ringing associated with coherent passive fluctuations [174]. Since acoustic ringing has been observed with recent high precision CMB measurements [114, 13], it is now clear that cosmic strings cannot be the main source of cosmological fluctuations. Their contribution is bounded from the accurate measurements of the angular power spectrum of the CMB in the region of the first acoustic peak to be less than 10% [138, 195, 62, 164, 18, 19, 8, 9] which corresponds to a value of $G\mu$ of about 3×10^{-7}. In the literature, one finds slightly stronger constraints which come from pulsar timing data [23, 92, 176, 115, 109, 85]. However, pulsar bounds make use of estimates of the spectrum of gravitational radiation from cosmic string loops. Since there is still a lot of uncertainty about the distribution of cosmic string loops, and since the amount of gravitational radiation from a fixed loop is also rather uncertain, bounds on $G\mu$ coming from millisecond pulsar timing are not very robust. Much more robust signatures come from the long and straight strings, signatures which we are discussing in this paper.

Early work to identify the KS signal of cosmic strings in CMB anisotropy maps was presented in [118] which concluded that the angular resolution of WMAP would not be small enough to resolve the KS signature. After the release of the WMAP data [13], there were two sets of analyses introducing new algorithms to look specifically for the KS signature. Lo and Wright [108] applied a matched filtering method, whereas Jeong and Smoot [86] introduced new statistics such as one measuring the connectedness of neighboring temperature steps or another one proposing a decomposition of the temperature map into constant, Gaussian and straight string step components. Both groups applied their statistics to the WMAP data. From the null results of the searches, a direct upper bound on the string tension of $G\mu < 10^{-6}$ could be set, a bound not competitive with the existing bounds from the matching of the angular power spectrum.

In [6], it was proposed to make use of the Canny algorithm [36] to search for the KS effect, and the preliminary analysis showed that the statistic offers the promise to improve the limit on $G\mu$ from direct searches for the KS signal by a large factor. The Canny algorithm is an edge detection algorithm which was previously used in image recognition work and metallurgy. It looks for lines in a map across which there is a large gradient. Thus, the algorithm appears to be well suited to detect the KS signature. In this paper we present a new and improved implementation of the Canny algorithm and apply it to test data. In agreement with [6] (and with the followup paper [173]), we find the new analysis based on the Canny algorithm is able to find or rule out strings with a tension greater than an upper bound which is more than an order of magnitude smaller than previous bounds derived from looking for the KS signature of strings. We emphasize that the code on which this paper is based was developed completely independently from that used in [6] and [173]. It is different in structure and in fact is based on a different programming language. The fact that the results reported here agree with those in [173] presents a very important check on the methods.

The Canny algorithm works in position space. Starting from an anisotropy map, it first produces an "edge map", the edges corresponding to lines in the sky perpendicular to which the gradient of the anisotropy map is sufficiently large [3] . The edge detection algorithm must be able to take into account the fact that Gaussian noise superimposed on top of the cosmic string signal will produce large variations in the magnitude of the gradient along a cosmic string edge. Given the edge map, a second algorithm counts the number of edges of fixed length and produces a histogram of edge lengths. Both the edge detection and the edge counting algorithms contain various parameters and thresholds which can be set by the user and which can be tuned to give the algorithm maximal discriminatory power, and are improved over the original code presented in [6]. The values of the thresholds and parameters will depend on the specific data. The final step of the code is a statistical comparison between the histograms produced in the previous step for data with and without cosmic strings.

The outline of this paper is as follows: In the following section we discuss the construction of the test data maps - both the pure Gaussian maps and the maps containing cosmic strings. In Section 3.4 we present the new implementation of the Canny algorithm. We first describe the algorithm which takes the CMB temperature map and converts it into an edge map. Then, we turn to

[3] As detailed in Section 3.4, a new aspect of the present code is to search for gradients in a range tuned to the expected KS signal.

the separate algorithm which is used to produce a histogram of edge lengths. Section 3.5 presents the results from the application of the Canny algorithm to the test maps. We conclude with a summary of the method and results, focusing on refinements of the code which can be made to improve the code's discriminatory power, and give a preview of future applications.

3.3 Simulations

In this section we describe the codes which were used to create the simulated temperature maps. The maps have two components, firstly a Gaussian map with an angular power spectrum corresponding to the inflationary "concordance model", the second a map of anisotropies produced by long cosmic strings according to the KS effect. These simulation routines have been created from scratch, without using any input from the existing code [6]. The simulation routines are written in Interactive Data Language (IDL). Both for the inflationary fluctuations and the cosmic string maps, the theory predicts ensemble averages from which particular classical realizations are drawn. To obtain firm predictions, a large number of simulations must therefore be run.

Since we have in mind applying our code to surveys with small angular resolution but only partial sky coverage, we work in the "flat sky" approximation [192] in which a segment of the sky is approximated by a rectangle. This approximation is made because of computational ease, since the basis solutions of the wave equation in flat space, the Fourier modes, are much easier to work with than the basis functions on a sphere, the spherical harmonics.

3.3.1 Gaussian Map

First we create a square grid temperature map of the Gaussian inflationary perturbations. The grid size is set by the angular resolution and by the angular size of the survey which we want to simulate (the number of grid points along an axis is $N_{max} = L/R$, where L is the extent of the survey along the axis being considered, and R is the angular resolution). The map is constructed based on the angular power spectrum of CMB fluctuations computed using one of the standard codes used in the literature (see below).

A differential temperature value, $\Delta T/T$, (corresponding to the temperature with the monopole subtracted) is assigned to each grid point (n, m) (n and m are integers) of the map, where each grid point represents a position in the window of the observed sky. If L is the length of a side of the window of observation in degrees in the first coordinate direction, then the angular distance of a grid point (n, m) from the edge is $x = nL/N_{max}$. The two dimensional vector is designated by $\boldsymbol{x}$.

The code is designed to construct a square grid. If rectangular areas are needed, we can construct a larger square temperature map and cut out the appropriate rectangle from this larger grid. The applicable scales are less than 60° indicating the applicability of the "flat sky" approximation.

In general, the temperature anisotropy of the CMB is expressed in terms of spherical harmonics $Y_{lm}(\theta, \phi)$, θ and ϕ being latitude and longitude, respectively:

$$\frac{\Delta T}{T}(\theta, \phi) = \sum_{l,m} a_{lm} Y_{lm}(\theta, \phi) \tag{3.3}$$

where a_{lm} are the coefficients of the expansion. However, since the observed window will be less than 60 degrees (we will take it to be approximately 10 degrees), plane waves can be substituted for Y_{lm} per the flat sky approximation:

$$\frac{\Delta T}{T}(\boldsymbol{x}) = \sum_{k} T(\boldsymbol{k}) e^{i\boldsymbol{k}\cdot\boldsymbol{x}}. \tag{3.4}$$

(N.B. In the following equations $T(\boldsymbol{x}) = \Delta T(\boldsymbol{x})/T$ and $T(\boldsymbol{k}) = \Delta T(\boldsymbol{k})/T$) Comparing these equations, it is obvious that the coefficients $T(\boldsymbol{k})$ correspond to a_{lm} so that:

$$\langle T(\boldsymbol{k})^2 \rangle = \langle a_{lm}^2 \rangle \equiv C_{l(k)}, \tag{3.5}$$

in which the angular brackets stand for ensemble averaging, and the C_l give the angular power spectrum of the CMB. According to the ergodic hypothesis, the ensemble average is equivalent to the spatial average. Thus,

$$\langle a_{lm}^2 \rangle = \frac{1}{2l+1} \sum_{m=-l}^{l} a_{lm}^2, \tag{3.6}$$

which, as indicated in (3.5) is the square of the width of a Gaussian distribution, namely $T(\boldsymbol{k})$. The probability of a given $T(\boldsymbol{k})$ follows a Gaussian distribution just as the a_{lm} follow a Gaussian distribution.

The temperature map in Fourier space, $T(\boldsymbol{k})$, is arranged into a grid in which each grid point is assigned physical angular coordinate values k_x and k_y, which are related to the numerical k_{xn} and k_{yn} values (each ranging between 0 and $N_{max} - 1$) by

$$\begin{aligned} k_x &= \frac{2\pi}{L}(k_{xn} - k_{max}) \\ k_y &= \frac{2\pi}{L}(k_{yn} - k_{max}) \end{aligned} \tag{3.7}$$

in which the k_x and k_y values run from $-k_{max}$ to k_{max}. The value of k_{max} corresponds to the angular resolution of the data set. Note that this setup requires us to have an odd number of pixels in our Gaussian map. If an even number of pixels is required, the Gaussian map can be stripped of a row and column once it is constructed.

Using

$$\lambda = \frac{360°}{l} = \frac{2\pi}{k}, \tag{3.8}$$

in which the wavelength, λ is measured in degrees and the wavenumber k is measured in inverse degrees, we compute the dependence of the degree of the spherical harmonic (mode number) $l(k)$ on the magnitude k of $\boldsymbol{k}$. Once this is done, we can look up the corresponding C_l for each $\boldsymbol{k}$ from the output of a standard CMB simulation code (see below). Since $l(k)$ is not necessarily an integer, for each value of k, the program then determines the value $C_l(k)$ by linear interpolation between the C_l values of the two closest values of l corresponding to each $l(k)$.

Given the C_l values determined as described above, the Fourier space temperature map $T(k)$ can be determined by

$$T(k_x, k_y) = \sqrt{C_{l(k_x,k_y)}/2}(g_1(k_x, k_y) + ig_2(k_x, k_y)) \tag{3.9}$$

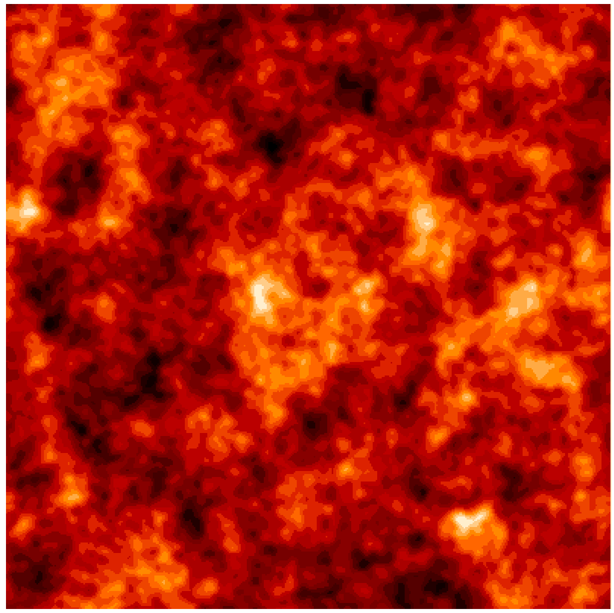

Figure 3.2: Figure of the gaussian temperature map with a window of 10° and a resolution of 1.5 arcminutes.

where $g_1(k_x, k_y)$ and $g_2(k_x, k_y)$ are randomly generated numbers obtained from a Gaussian distribution with variance one and mean of zero.

Since the position space temperature map $T(\boldsymbol{x})$ must be real, then $T(\boldsymbol{k})$ must satisfy $T(\boldsymbol{k}) = T^*(-\boldsymbol{k})$.

In summary, we derive $T(\boldsymbol{k})$ from the values of C_l determined as described above, and $T(-\boldsymbol{k})$ making use of the Hermitian property. Finally, to compute $T(\boldsymbol{x})$, we perform a Fast Fourier Transform on $T(\boldsymbol{k})$. Figure (3.2) shows the output of a temperature map with pure Gaussian noise.

We use the Code for Anisotropies in the Microwave Background (CAMB) [107] to generate the CMB temperature map generated by inflationary perturbations. CAMB, like the code on which it is based, CMBFAST [165], employs the line of sight integration prescription to compute CMB anisotropies. The advantage of using CAMB is that it computes C_l's for higher l's. Whereas CMBFAST can at best compute the power spectrum to $l = 3000$, corresponding to a resolution of 10 arcminutes, we use a power spectrum generated by CAMB up to $l = 22000$, corresponding to a resolution of 1.39 arcminutes. Simulations with higher resolution will enable us to place lower bounds on the string tension of cosmic strings. Additionally, high resolutions are necessary to apply our algorithm in the future high resolution CMB experiments such as ACBAR [104] and the South Pole Telescope [151].

The parameters we use for our simulations are standard ΛCDM concordance parameters based on fitting the model to a multi-experiment data set CMBall [148], namely $\Omega_b h^2 = 0.0227$, $\Omega_c h^2 = 0.112$, $\Omega_m = 0.26$, $H_0 = 71.8$, $n_s = 0.965$, $w = -1$ (the equation of state for dark energy), $\Omega_\nu h^2 = 0$, $T_{CMB} = 2.726$ (the temperature of the CMB), $Y_{He} = 0.24$, and reionization optical depth, $\tau_{reion} = 0.093$.

3.3.2 Temperature Map from pure Cosmic Strings

Next we generate a temperature map of superimposed straight line segments representing the effects of long cosmic strings obeying the scaling solution. As in the Gaussian simulation, each grid point is assigned a temperature fluctuation $\Delta T/T$.

For simplicity we do not include the effects of string loops or of the small scale structure on the strings. According to the current status of cosmic string simulations, the effects of long strings dominate the cosmic string CMB sky. Small-scale structure on the long strings would maintain the KS effect (albeit with slightly reduced amplitude). Thus, in terms of searching for the KS signature of strings, the simplifications we use can be justified as a first step. Going beyond this approximation would require much more involved simulations (like those of [63]) with many more parameters. [4] In future work we

[4] Although in principle cosmic string models are determined by a single parameter, namely μ, the cosmic string evolution cannot be followed either analytically or numerically without making additional assumptions, in particular on how cosmic strings interact. The results obtained in different numerical analyses concerning the string loop distribution vary by orders of magnitude (see e.g. the different results obtained in [4, 16, 5]), whereas the results for the distribution of long strings are comparable. Thus, whereas limits based on long strings are robust, those which include effects of string loops are not.

plan to apply our Canny algorithm code to temperature maps obtained from more sophisticated simulations that include more detailed structure of cosmic strings.

In contrast to the Gaussian string map which is set up in Fourier space and transformed to position space via a Fourier transform, the string maps are set up directly in position space. As explained in the Introduction, each long string whose region of influence intersects the past light cone of the window in the sky we are considering will contribute a KS signal. We assume that the area in the sky affected by the temperature discontinuity of a single straight string segment per the KS effect is a rectangular box on each side of the string. The depth of the box (length perpendicular to the string) is equal to the Hubble length [112]. The size of the box in direction of the string is taken to be the product of the Hubble length and a length coefficient γ. The Hubble length corresponds to the time at which the past light cone intersects the region of influence of the string. We apply the KS signature by adding a positive temperature fluctuation to grid points in the box on one side of the string, and by adding the corresponding negative temperature fluctuation to the grid points in the box on the other side of the string.

We are using a toy model for the cosmic string distribution first introduced in [133, 134] and also used by Pogosian et al. in [138, 195, 62, 164, 18, 19, 8, 9]. It is based on a simple representation of the distribution of long strings as described by the scaling solution. According to this solution, the distribution of long strings is at all times like a random walk with a step length which is of the order of the Hubble radius at that time. We will denote this length by γH^{-1}, where γ is a constant factor of order one. Physically, this length represents the mean curvature radius of the string network. In the toy model, this distribution is approximated by a collection of straight string segments of length γH^{-1}.

One can argue that the curvature radius of the network of long strings must be of the order of the Hubble radius. If the curvature radius is larger than the Hubble radius, the strings will sit there as the universe expands until the Hubble radius catches up. If the curvature radius is less than the Hubble radius, then the strings will oscillate wildly, intersect and split off string loops (which then decay by gravitational radiation) until the curvature radius catches up to the Hubble radius. So the curvature radius will always be of order of the Hubble radius. The key ingredients in this argument are, firstly, that the effective action for a cosmic string is the Nambu-Goto action and hence the string dynamics is relativistic, and secondly that when strings cross they will intercommute, i.e. exchange ends, thus allowing the production of string loops.

Since the strings are relativistic, the distribution of strings will have changed after one Hubble time. Snapshots of string distributions at time steps separated by Hubble time intervals will, when rescaled to the Hubble radius, look like independent realizations of a stochastic process. Hence, in our toy model of the distribution of long strings, we take the string segments to be independently distributed over time intervals greater than a Hubble time.

The input parameters for the string map generating function are the number of pixels on each side of the window, the number of degrees the window subtends, the number of strings per Hubble volume per the scaling solution, the string tension, $G\mu$, and the length coefficient γ.

The procedure to simulate cosmic strings is to follow the past light cone in time intervals $t_{n-1} \leq t < t_n$, where $t_{n+1} = \alpha_1 t_n$, from the time of last scattering to the present time. If $\alpha_1 = t_{n+1}/t_n = e$ then there are approximately 15 time intervals.

Next we project all strings present in one Hubble time interval to a fixed time hypersurface at the center of the time interval. This is done for all time intervals. On the microwave sky, the Hubble length in degrees corresponding to the comoving distance of the Hubble radius in space at the n'th time interval can be shown to be (making use of the equation of state and of the Friedmann equation)

$$d_c(t_{n+1}) \, = \, d_c(t_n)\alpha_1^{1/3}\,, \tag{3.10}$$

in which $d_c(t)$ is in degrees. This recursion relation starts with $d_c(t_0) = 1.8$.

We need to find all of the strings which for a fixed time interval influence the CMB temperature map of the observed window. Instead of simulating only strings in the observed window, we must consider all strings in an extended window. This protects us from missing strings that start outside of the observed window but extend into it. At each time interval, the extended window is a square with each side subtending the degrees of the observed window added to twice the Hubble distance for that time step. The observed window is the central section with one Hubble length on either side.

Next we compute the number of Hubble volumes the extended window subtends at each time step, and the number of strings in each extended window. The number of Hubble volumes is obtained as the square of the number of degrees subtended by each extended window divided by the degrees subtended by each Hubble distance. The number of strings expected in the extended window for each time step is the rounded product of the strings per Hubble volume (determined as an input parameter based on the scaling solution) and the fraction/number of Hubble volumes a window subtends for each of the 15 time intervals.

Next we loop through each time step and each expected string in the extended window to determine where the string should be placed in the extended window and to place it by constructing a temperature differential. This is completed in a separate function in the program.

To simulate the strings, the program randomly places a line segment with a length given by $\gamma \cos \alpha H^{-1}$, where the Hubble length H^{-1} is in radians for the given time step. The angle α runs from 0 to $\pi/2$. Multiplying by $\cos \alpha$ accounts for a projection from three to two dimensions. Although technically the length of the string should be multiplied by a coefficient given by projecting a geodesic on a sphere onto a plane, since we are dealing with small window sizes and the flat sky approximation is appropriate, this complication is unnecessary. The location of the beginning of the string and its direction are determined randomly. The location of the beginning of the string is given by taking the product of a random number between 0 and 1 for both directions on the grid and the length of the extended window in radians. The direction of the placement of the string, i.e. the angle θ of the string, is chosen by a randomly generated number between $-\pi/2$ and $\pi/2$. This is the direction of the string as given by the angle from the x-axis. Finally, a binary flag is used to determine which side of the string will be a positive temperature fluctuation and which side will be a negative temperature fluctuation. The value of the flag is randomly determined.

Next the code computes (from the location of the start of the string and the direction of the string) the end point of the string and each corner of the box around each side of the string and each slope for each boundary of the box.

The routine loops over each pixel in the observed window, starting in the lower left hand corner, to determine if the pixel lies within the box affected by the cosmic string. If it does, the temperature is changed by δT. The sign of δT is determined by the temperature flag delineated above. The temperature fluctuation is given by

$$\frac{\delta T}{T} = \tilde{v} r 4\pi G\mu \tag{3.11}$$

in which $T = 2.726$ is the background CMB temperature. In the above, $\tilde{v}$ represents the root mean square (over all strings) value of $v\gamma(v)$, where v is the transverse velocity of the string and its relativistic γ factor is $\gamma(v)$. Also, r a random number between 0 and 1 which adjusts the velocity to take into consideration the different velocities that the string might have as well as the projection of the velocity of the string onto the plane perpendicular to the line of sight. Based on recent cosmic string evolution simulations we use the value $\tilde{v} = 0.15$.

Figure 3.3 shows the temperature map produced by a simulation with a few test cosmic strings (not a scaling solution). The temperature boxes produced by the individual strings are clearly visible. Figure 3.4 demonstrates the corresponding results from a full string simulation with $N = 1$, i.e. one string per Hubble volume. The straight line temperature discontinuities produced by

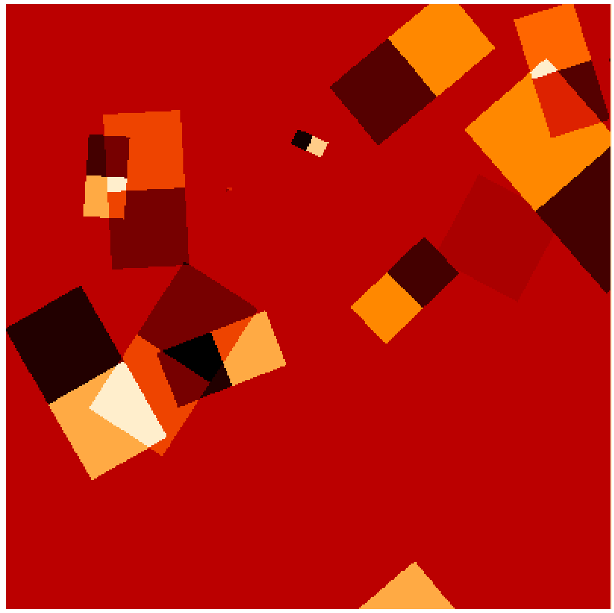

Figure 3.3: A cosmic string simulation for a few strings. The light areas represent where the temperature fluctuation is positive and the dark areas represent where the temperature fluctuation is negative.

individual strings are still visible. However, there are a lot of overlap regions since a given photon will during its trajectory pass close to several strings. The overlapping problem gets worse for $N = 10$, as clearly visible in Figure 3.5.

As a further test of the algorithm described in this subsection we show the resulting angular power spectrum of temperature anisotropies. The figure (Figure 3.6) is for a pure cosmic string map with $N = 10$ and $G\mu = 6 \times 10^{-8}$. The range of l values are limited from below by the angular size of the simulation box, and from above by the angular resolution we have chosen. The error bars are standard errors of the mean based on 100 runs. As theory predicts [180, 158, 171, 179], the angular power spectrum is approximately scale-invariant on large angular scales (the deviation from scale-invariance at the lowest values of l is presumably a boundary effect), and its amplitude is consistent with what is expected.

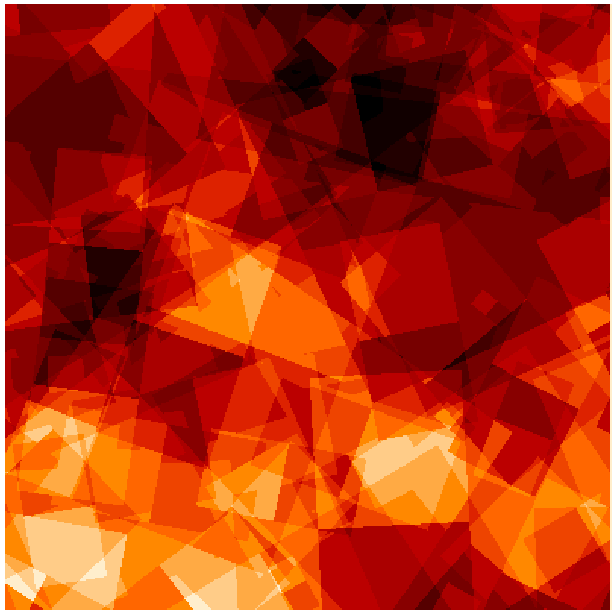

Figure 3.4: The CMB temperature anisotropy map produced by a scaling cosmic string simulation with $N = 1$. The discontinuity lines in the maps produced by the KS effect are clearly visible, but there are a lot of overlap regions where a number of strings affect the temperature at a fixed point.

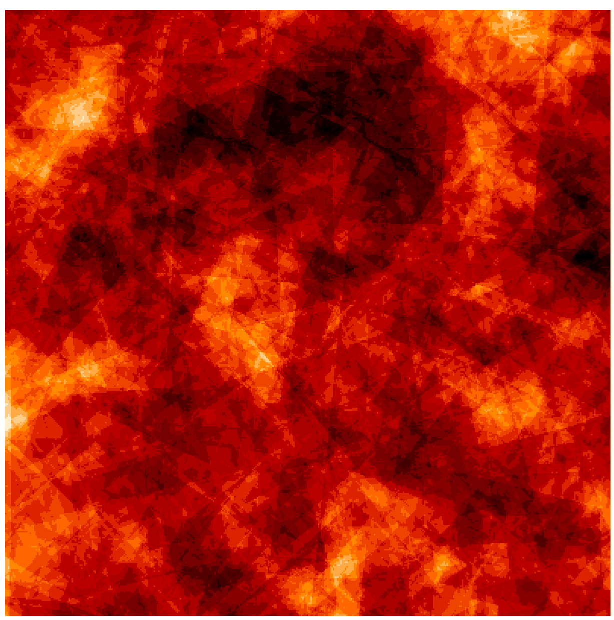

Figure 3.5: The CMB temperature anisotropy map produced by a scaling cosmic string simulation with $N = 10$. In this case the effects of overlaps is much more pronounced.

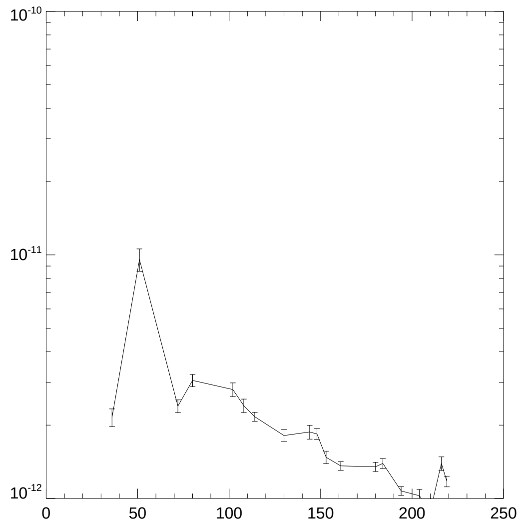

Figure 3.6: The angular power spectrum of the CMB anisotropy maps of pure cosmic string simulations with values $N = 10$ and $G\mu = 6 \times 10^{-8}$. The horizontal axis is l, the vertical axis is $l(l+1)C_l$.

3.3.3 Sum of Gaussian Map and Cosmic String Map

Our goal is to test if the Canny algorithm is able to pick out the KS signature from strings even if the strings are a subdominant component to the CMB fluctuations. To test this, we need to produce temperature maps which contain both cosmic strings for some value of $G\mu$ and a spectrum of Gaussian fluctuations like in the concordance ΛCDM model, except with an amplitude of the Gaussian noise which is reduced such that the total angular CMB power spectrum remains consistent with either simulations or observations.

Here we describe how to find the coefficient, a, for each map which will be used to add the pure string map to the pure Gaussian map to get a Gaussian map with superimposed strings,

$$T_{G+S}(\boldsymbol{k}) \;=\; aT_G(\boldsymbol{k}) + T_S(\boldsymbol{k}), \tag{3.12}$$

with T_{G+S} as the temperature of the Gaussian map plus pure string map and T_G and T_S as the temperature maps of the concordance Gaussian and string simulations respectively. Alternatively, we could use the temperature map of the best current data, the five year results of WMAP [99], for T_G. It is important to use consistently either the temperature map from experimental data or from theoretical simulations for both T_G and T_{G+S} since the C_l's for the two models are not identical.

We want the model to give the best possible agreement with the data, either experimental or simulated. Hence, the plan is to adjust the coefficient a so that the combined string and Gaussian map, $T_{G+S}(\boldsymbol{k})$, fits the data best. This means that we adjust the Gaussian map so that the corresponding C_l's of $T_{G+S}(\boldsymbol{k})$ give an optimal fit to the data. Since the error bars on the observed angular power spectrum C_l are smallest relative to the signal in the range from $l_{min} = 10$ to $l_{max} = 220$ we shall fit the C_l's within this range. Note that this range includes most of the first Doppler peak region. Now for values of l comparable or larger than that corresponding to the first Doppler peak, the contribution from strings is dominated not by the Kaiser-Stebbins effect from strings between t_{rec} and t_0, but from string-induced fluctuations at last scattering which are not included in our analysis. Thus, there is an intrinsic inaccuracy in the determination of the value of a. If we were to take l_{max} to be the value where the Kaiser-Stebbins effect ceases to be dominant (a value much smaller than 220), then we would obtain a smaller value for a and hence a better discriminatory power of our algorithm. However, this procedure would be worse than the one we have adopted, since we would be working with a power spectrum which is a much worse fit to the observations in the Doppler peak region than the one we are using. Our choice of l_{max} can thus to be considered to be a conservative one.

The first step is to find the C_l values from the pure string map. To do this, the routine initially takes the inverse FFT of the temperature fluctuation $T(\boldsymbol{x})$ to compute $T(\boldsymbol{k})$. Then, using $k = 2\pi l/360$, the routine computes the wave number magnitudes $k(l)$ for all values of l in the our range. Then the value of δk corresponding to $\delta l = 1/2$ is found.

Next, the map summation routine finds the wavenumber magnitude k for all values of $\boldsymbol{k}$ (whose components range from $-k_{max}$ to k_{max}). For each value of l in the range between l_{min} and l_{max} the code finds the components k_x and k_y of all waves for which the magnitude of k lies within δk of $k(l)$. Knowing k_{xn} and k_{yn} we can find the corresponding $T(\boldsymbol{k})^2$ for each of the wavenumbers. Once all of the $T(\boldsymbol{k})^2$ values are found for each l, we find the average to get $\langle T(\boldsymbol{k})^2 \rangle$ for each l. These values are the C_l values of the pure cosmic string map for all l between l_{min} and l_{max}.

Since

$$T_{G+S}(\boldsymbol{k}) \;=\; aT_G(\boldsymbol{k}) + T_S(\boldsymbol{k}) \tag{3.13}$$

we obtain

$$\langle T_{G+S}(\boldsymbol{k})^2 \rangle \;=\; a^2 \langle T_G(\boldsymbol{k})^2 \rangle + \langle T_S(\boldsymbol{k})^2 \rangle + 2a \langle T_G(\boldsymbol{k}) T_S(\boldsymbol{k}) \rangle\,. \tag{3.14}$$

However, $\langle T_G(\boldsymbol{k}) T_S(\boldsymbol{k}) \rangle = 0$ because the Gaussian and string temperature fluctuations are independent. Hence

$$C_{l(G+S)} \;=\; a^2 C_{l(G)} + C_{l(S)}. \tag{3.15}$$

Now that we have the C_l values for the simulated CAMB data, $C_{l(G+S)}$, the C_l's we found for the pure cosmic string map, $C_{l(S)}$, and the C_l's for the simulated gaussian map from CAMB, $C_{l(G)}$, we can compute a^2 for each l by viewing (3.15) as a defining relation for a^2. Obviously, for each value of l we will get a different answer. To compute a single coefficient a which best fits all of the l's from l_{min} to l_{max} we perform a linear fit on the coefficients, a, for each l. We use the best fit $y-$intercept of a linear model fit by minimizing the χ^2 error statistic for a. The y-intercept can be used because the slope of the best fit to the linear model is negligible.

Once a is found for a particular string image, the result is averaged over all of the generated simulated string images to obtain the final value for a which is then used for all the string maps of a given $G\mu$.

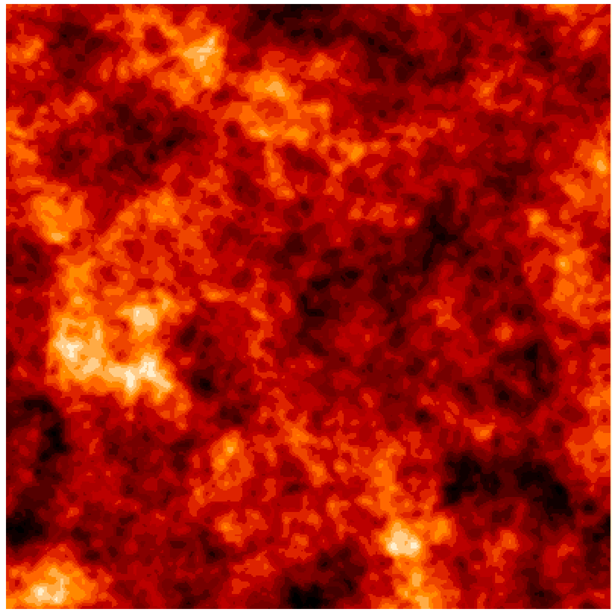

Figure 3.7: The smoothed CMB temperature anisotropy map produced by a simulation with both Gaussian noise and cosmic strings with $G\mu = 3.5 \times 10^{-7}$ and$N = 10$. In this case the KS discontinuity lines are visible.

Figure (3.7) shows the resulting CMB anisotropy map in a simulation with a large value of $G\mu$ chosen such that the strings play an important role. Comparing the map to the pure string map of Figure (3.5) we see that the string-induced line discontinuities are still visible. However, in the case of a lower value of $G\mu$ the effects of the strings are not visible by eye and we need to resort to a statistical analysis to study whether the map is distinguishable from that of pure Gaussian noise (Figure (3.8)).

We use the algorithms described in this section to generate maps with and without cosmic string signals. The main question we would like to address now is down to what value of $G\mu$ the Canny edge detection algorithm is capable of distinguishing between these two sets of maps in a statistically significant way. In the following section we describe our realization of the Canny algorithm

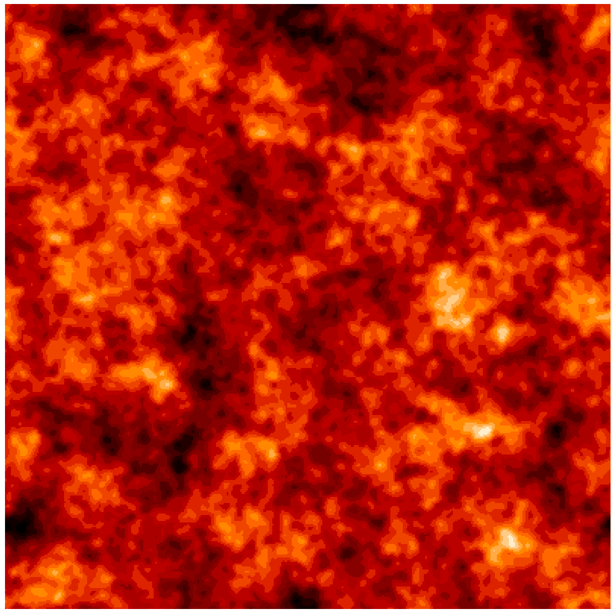

Figure 3.8: The CMB temperature anisotropy map produced by a simulation with both Gaussian noise and cosmic strings with a smaller value of $G\mu$, namely $G\mu = 2 \times 10^{-8}$ and $N = 10$. In this case the KS lines are not visible by eye.

routine which turns a microwave temperature map into an edge map, the edges standing for lines across which the gradient is a local maximum.[5]

3.4 Implementation of the Canny Algorithm

In this section we describe our implementation of the Canny algorithm. In its original version [36], the Canny algorithm is intended to find lines in the map with maximal gradients across the line. In this way, the algorithm can be applied to the image of a face and returns a map where only the pixels of the map with the strongest features are shaded in. Similarly, the algorithm could be applied to find crystal defect lines on metallic surfaces. Our original work applying the Canny algorithm to CMB maps [6] also was based on this idea.

[5] In our realization of the algorithm, we impose an additional requirement, namely that the gradient magnitude is tailored appropriately to the expected cosmic string signal.

However, to look for cosmic strings we are less interested in the local maxima of the gradient map which overall have maximal amplitude. Rather, we are interested in local maxima of the gradient for which the amplitude of the gradient is in correspondence to the expected KS signal. Thus, in contrast to the original Canny routine which uses two thresholds, we here introduce a modified algorithm in which three gradient thresholds are made use of (as in [173]). The use of the thresholds is described below.

We will first give a brief overview of how the algorithm works. First, an optional part of the Canny algorithm is to smooth the map in order to eliminate shot noise. The second step in the algorithm is to construct a map of the temperature gradients. Next, locations must be identified which correspond to local maxima of the gradients. The maximal average gradient of the pure string map determines the three thresholds used. The fourth part of the algorithm involves selecting among the grid points identified as local maxima those which have the right range of magnitudes. Gradients larger than some upper threshold are not due to single strings and will hence be discarded. Those above a second threshold quite close to the expected edge strength will be kept. To take into account the fact that Gaussian noise may well decrease the amplitude of some pixel along a string edge below the above-mentioned threshold, we introduce a third (the lowest) threshold and keep the pixels whose gradient is larger than that threshold, provided that the pixel is connected to a pixel with gradient amplitude above the second threshold (and provided that the gradient directions are appropriate and that the pixel is connected to a pixel in one of the allowed directions relative to the gradient). The pixels thus selected form the Canny edge map. Given the pixel edge map, a next step in the algorithm is to identify the edges in the pixel edge map. The length of each edge is found, and a histogram of edge lengths is produced. The analysis part of the algorithm then checks if for a fixed value of $G\mu$ the histograms of a pure Gaussian noise map and of a noise map including a contribution of cosmic strings (and appropriately reduced amplitude of the Gaussian noise) are statistically significantly different.

In implementing the Canny algorithm, several (three) choices must be made beyond fixing the three thresholds used. We look for the set of choices which give the best differentiation between maps with and without strings.

The first step in our implementation of the Canny algorithm is the filtering of the data. This filtering is intended to eliminate point source noise. In studies like the present one in which we are dealing with simulated data which has no noise, the maps can be used without smoothing. In order to eliminate point sources, smoothing should be used in the case of real data. We have explored the effects which smoothing has.

The routine first produces an un-normalized filter map $\tilde{F}(i,j)$ (i and j are integer labels running from 1 to N_f indexing the pixels of the filter map)

$$\tilde{F}(i,j) \;=\; e^{-\frac{x^2+y^2}{2\sigma^2}} \tag{3.16}$$

in which $x = i - (N_f - 1)/2$, $y = j - (N_f - 1)/2$, $\sigma = 0.5N_f$, and N_f is the number of pixels along one direction of the filter map, an input parameter in the smoothing routine. The normalization is the sum of all of the unnormalized weights

$$C_1 \;=\; \frac{1}{\sum_{ij} \tilde{F}(i,j)}\,. \tag{3.17}$$

Now we can determine the normalized filter map as

$$F(i,j) \;=\; C_1 \tilde{F}(i,j). \tag{3.18}$$

Finally, we convolve the input temperature map with the filter map to obtain the filtered data map. If $M(i,j)$ denotes the initial map, then the filtered map $FM(i,j)$ is given by

$$FM(i,j) \;=\; \sum_{k,l=1}^{N_f} M(i-x, j-y) F(k,l)\,, \tag{3.19}$$

where x and y are determined from k and l as indicated below (3.16). Boundary points require special treatment. We repeat the points at the boundary.

The second part of the algorithm involves constructing the gradient maps. Two arrays are created, the first containing the magnitude of the gradient at each pixel of the map, the second containing the information about the direction of the gradient.

We compute the lattice derivatives by shifting the temperature map in each of the eight directions and looking for the maximal difference. Instead of using the usual lattice gradient which is defined by

$$
\begin{aligned}
\hat{G}(x,y) &= \frac{G(x+\epsilon,y)-G(x-\epsilon,y)}{2\epsilon}\hat{x} \\
&+ \frac{G(x,y+\epsilon)-G(x,y-\epsilon)}{2\epsilon}\hat{y}\,,
\end{aligned} \tag{3.20}
$$

(where the grid spacing is ϵ), we shall use the following as our definition of the magnitude of the gradient:

$$
G(x,y) \;=\; \max|\Delta G| \tag{3.21}
$$

and the direction is taken to be that for which the maximum value of $|\Delta G|$ occurs. ΔG is given by the discrete gradient

$$
\Delta G(x,y) \;=\; \frac{G(n(x,y))-G(x,y)}{d(x,y)}\,, \tag{3.22}
$$

where $n(x,y)$ denotes the neighboring point to (x,y) and $d(x,y)$ is the distance between $n(x,y)$ and (x,y). For neighboring points not on the diagonal, the distance between the neighboring point and the point (x,y) is 1, for points along the diagonal the distance is $\sqrt{2}$.

The gradient of the image is then stored as an array with a dimension containing the two dimensional pixel array with the edge strengths and a dimension containing the two dimensional pixel array with the edge directions as the values.

The next step is to find the pixels of the map which correspond to local maxima in the direction of the gradient. We first shift the map one unit forwards and backwards in each of the four directions (along the coordinate axes and along the two diagonals, respectively). For each of these four shiftings we focus on points for which the absolute value of the gradient is greater than at the two neighboring points on either side. For all points selected, we check if the gradient is in the direction of the shifting. Pixel points which pass this test are kept. The others are assigned a value of 0. Boundary pixels are stripped from the list of local maxima since their magnitudes are influenced by boundary effects. In Appendix A we discuss the local maxima doubling problem which the code has to deal with.

As mentioned at the beginning of this section, our implementation of the Canny algorithm makes use of three thresholds t_u, t_l and t_c. Their values are chosen to correspond to the amplitude of the KS effect of a single string since it is this effect which we want to identify.

Thus, to set the thresholds for a given value of $G\mu$, we first run the code on a number of pure string simulations for that value of $G\mu$. We determine the maximal gradient (amplitude) $G_{max,i}$ for each simulation, and define the "string maximal gradient" G_m as the average of the individual maxima $G_{max,i}$.

Returning to our list of candidate local maxima, then if the amplitude is larger than $t_c G_m$ the point is discarded since it is not due to a typical string gradient. For amplitudes in the range

$$t_u G_m < \mathcal{A} \leq t_c G_m \tag{3.23}$$

then the pixel coordinates and gradient directions are stored in arrays. Later on, the edge pixel map will be constructed by marking all pixel points in the above-mentioned coordinate array as 1. These are pixels for which the gradient is in the right range to be due to the KS effect from a cosmic string. Pixels with a slightly lower gradient amplitude might still be due to the KS effect from a string with amplitude slightly reduced by noise. It is advantageous for the success of the Canny algorithm to take into account this possibility. Thus, if the amplitude of the local maxima is in the range

$$t_l G_m < \mathcal{A} \leq t_u G_m \tag{3.24}$$

then the coordinates and gradient directions of such pixels are stored in arrays corresponding to pixel points marked 1/2. Arrays are created to store the indices of the points marked as 1 and 1/2 and separate arrays are created to store the directions of the corresponding indices.

The next step is the "edgefinder" routine which decides whether grid points marked as 1/2 belong to an edge or not. Roughly speaking, points marked as 1/2 are considered as belonging to an edge if they are direct or indirect neighbors to points labelled by 1 and the gradients are in a similar direction. To specify the routine, there are three choices which can be made for this algorithm, as will emerge below. We start from a point labelled 1 (an option in the program is to start with a point labelled 1/2 - the first of the three choices mentioned above)[6] . The program then searches in all eight directions for a contiguous point labeled as 1/2 or 1. For each direction, we check if it lies in the six directions (or 2 directions) perpendicular or near perpendicular (or just perpendicular - the second of the choices mentioned above) to the original point's gradient and check if the gradient is in the appropriate parallel or near parallel (or just parallel - the third choice) direction to that at the original 1 (or 1/2). If a point labeled as 1/2 is found, and the direction is in one of the allowed six (or two), then we mark the coordinates of that point and repeat the search starting from that point. We stop if a 1 is found, in which case we convert all of the 1/2s found on the way to 1. If we do not find another point labelled 1/2, we stop and do not change the labelling of the points encountered on the way. Then, we move on to the next point labelled by 1 which has not already been covered by the search. In the variant of the code in which the search starts with points labelled by 1/2, we search for points labelled by 1/2 or 1 as described above, mark the coordinates of the points found, and continue until either a point marked 1 is found (in which case all of

[6] Note that the algorithms starting from 1 or 1/2 are in fact different. This is also noted in footnote 7.

the 1/2 found are converted to 1), or else no new point is found, in which case the 1/2 are considered not to belong to a common edge and are not relabelled.

The output of the "edge-finder" routine is a list of coordinates of the pixels marked by 1 and of the corresponding gradient directions. The result of the algorithm can be represented by two maps. The first is a map of pixel points originally labelled as 1 and 1/2 (different shades), the second is an initial "edge pixel map", the map of the set of pixels labelled at the end of the "edgefinder" routine by a 1.

The final part of the Canny algorithm is an "edge-counting" routine (this part of our method goes beyond the standard Canny algorithm). This routine creates a second "edge pixel map" and a histogram of number of edges as a function of the edge length. Starting with the first entry in the list of pixels marked by 1, the routine searches in directions perpendicular or near perpendicular (or exactly perpendicular only) to the gradient direction to find other pixels labelled as 1. If such a pixel is found, then the routine checks if the gradient direction of the new pixel is near parallel or parallel (or exactly parallel only) to the direction of the gradient at the initial pixel. If this is the case, the routine considers the new pixel as part of the edge it is following. Once no further pixel is found, the routine considers the edge to have ended and saves the result. The program then moves to the next pixel labelled by 1. Pixels are only allowed to be counted in one edge. After all edges are found, the lengths are tallied and can be made into a histogram. To take into account the fact that a pixel may be missing from a string edge due to a large influence of the Gaussian component, there is an option for the "edge-counting" routine to allow for a gap in an edge of a certain length. This skipping length parameter is a further input parameter which the user of the algorithm has to set. As should also be obvious from the discussion in this paragraph, the same choices of "perpendicular exactly or nearly perpendicular" or "perpendicular exactly" and "parallel exactly or nearly parallel" or "exactly parallel" as in the "edge-finding" routine are open to the user in this part of the program.

Let us conclude this section by reminding the reader of the various parameters which have to be chosen and choices which have to be made in our Canny algorithm implementation. First of all, in our "edgefinder" routine there are the three thresholds t_c, t_u and t_l which are used in the labelling of the local maxima. Next, in our routine to turn 1/2 pixels into 1 pixels, there are three choices to be made, first whether one starts with 1 or 1/2 pixels, second whether one searches for neighboring 1s and 1/2s in direction perpendicular or in directions nearly perpendicular or perpendicular to the direction of the gradient, and third whether one demands that at the selected neighboring site the gradient is parallel or if it is nearly parallel or parallel to the direction of the gradient at the initial point. In the edge counting algorithm there are the two choices analogous to the two choices mentioned at the end of the previous discussion. The user of the program has similar choices of "perpendicular exactly or nearly perpendicular" versus "perpendicular exactly" to the gradient for the directions to search and "parallel exactly or nearly parallel" versus "parallel exactly" to make. Finally, there is the number of points which the "edge-counting" routine can skip.

3.5 Analysis

We tested the capability of our implementation of the Canny algorithm to distinguish between temperature anisotropy maps which arise from a pure Gaussian ΛCDM model and a model in which there is a contribution to the power spectrum coming from a scaling distribution of cosmic strings (and with the power of the Gaussian noise reduced to maintain the optimal fit to the CMB angular anisotropy power spectrum as described in Section 3.3).

Since we have applications to small-scale CMB anisotropy experiments in mind, we choose a simulation box of edge length 10^o and with angular resolution of $1.5'$. Both in the ΛCDM model and in the cosmic string model, the actual universe is a realization of a random process. Thus, in order to determine whether the Canny algorithm can distinguish between the predictions of the two theories, we have to run many realizations of the models. We ran 50

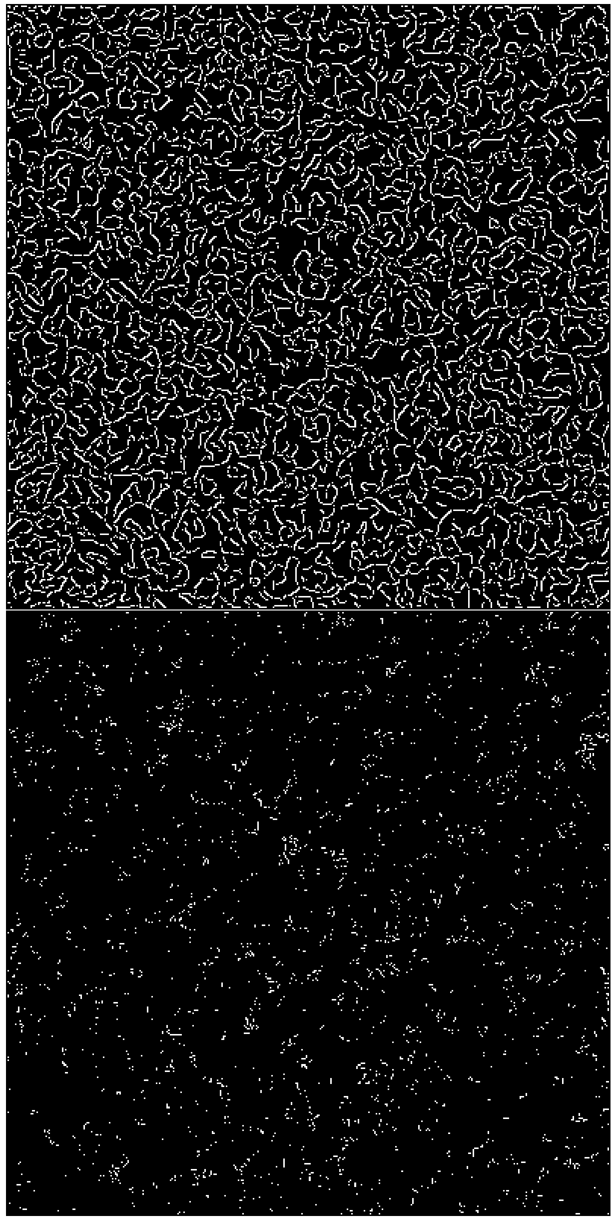

Figure 3.9: Edge maps for the gaussian map shown before. The first edge map is for a G_m and thresholds used in the analysis of an $N = 10$ gaussian map with strings for $G\mu = 3.5 \times 10^{-7}$. The thresholds are $t_c = 2$, $t_u = 0.25$, $t_l = 0.1$. The second edge map is made for the same gaussian map used in the analysis of an $N = 10$ gaussian map with strings for $G\mu = 2 \times 10^{-8}$. The thresholds are $t_c = 4$, $t_u = 0.25$, $t_l = 0.1$.

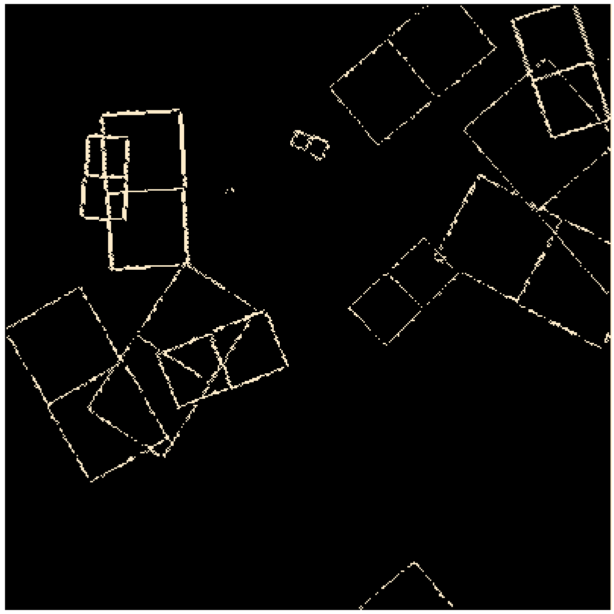

Figure 3.10: The test string edge map.

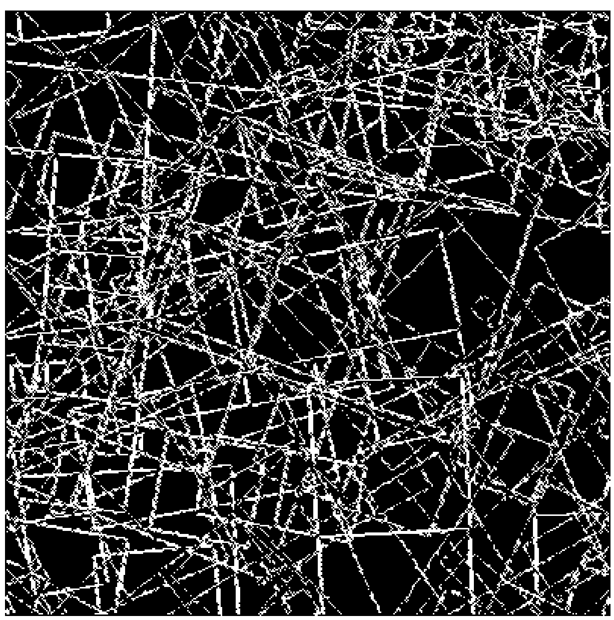

Figure 3.11: N=1 pure string edge map.

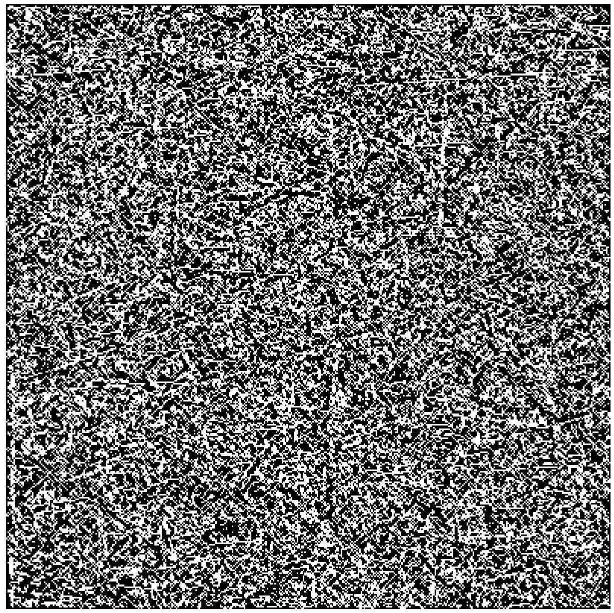

Figure 3.12: N=10 pure string edge map.

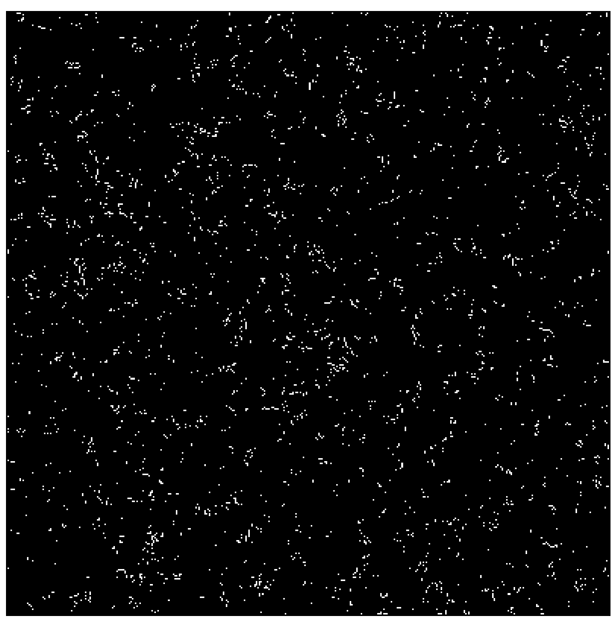

Figure 3.13: $G\mu = 2 \times 10^{-8}$ unsmoothed string plus gaussian noise edge map. N=10. The thresholds are $t_c = 4$, $t_u = 0.25$, $t_l = 0.1$.

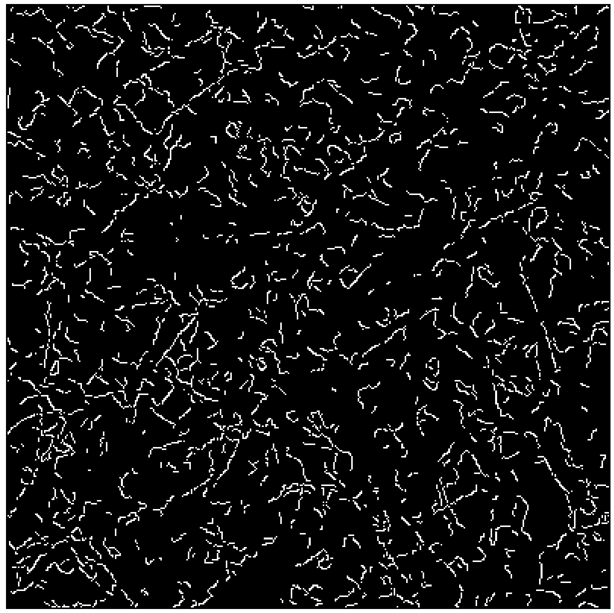

Figure 3.14: $G\mu = 3.5 \times 10^{-7}$ smoothed string plus gaussian noise edge map. N=10. The thresholds are $t_c = 2$, $t_u = 0.25$, $t_l = 0.1$.

simulations for both theories. This number was chosen since it is the number for which the resulting probabilities converge.

For small values of $G\mu$, we generated each cosmic string map independently. For larger values of $G\mu$ we generated the temperature maps by rescaling the temperature map for $G\mu = 6 \times 10^{-8}$. The value of G_m was scaled accordingly. The value of the scaling factor a was computed for each of the simulations for fixed value of $G\mu$ independently. Because of large fluctuations in the various random variables (e.g. the number of strings), there results a spread for the values of a, and some of the values of a^2 were negative for large values of $G\mu$. Thus, for large values of $G\mu$ we used a common value for a^2, namely the mean of the values of a^2 for $G\mu = 6 \times 10^{-8}$ and scaled according to (see [173]):

$$a^2 = 1 - \frac{\langle C_l^S \rangle_0}{\langle C_l^G \rangle_0} \left(\frac{G\mu}{G\mu_0} \right)^2 = 1 + (a_0^2 - 1) \left(\frac{G\mu}{G\mu_0} \right)^2 \tag{3.25}$$

$$a_0^2 = 1 - \frac{\langle C_l^S \rangle_0}{\langle C_l^G \rangle_0}, \tag{3.26}$$

where the subscript 0 indicates the reference value of $G\mu$.

Both the models and the Canny algorithm contain a number of parameters. As described in Section 3.3, we chose the best fit parameters of a ΛCDM model. For the cosmic string distribution, we considered $G\mu$ to be the free parameter of interest. We fixed the number of strings per Hubble volume to be $N = 1$ in some simulations and $N = 10$ in other simulations, the string segment length to be γH^{-1} with $\gamma = 1$, and the velocity parameter $\tilde{v} = 0.15$.

In this work we did a rough optimization of the various parameters which have to be chosen in the Canny algorithm. For a fixed value of $G\mu$ for which the effect of the strings is statistically significant we varied the parameters to find the parameter values which gave the best discriminatory power (see below). On this basis, we chose the various thresholds. Concerning the optimization of the "flags" in the routine, it proved advantageous to start with the pixels marked 1 in the edge finding algorithm, and to look in directions both perpendicular and near to perpendicular, and allowing the gradient at the neighboring point to be parallel or near to parallel in both the edge finding and the edge counting routines [7] .

We ran simulations both with and without smoothing of the maps. In the runs with smoothing, the smoothing was done in the final maps (after adding

[7] We ran the Canny algorithm on two different test maps to develop an intuition on how to optimize the flags. For both test maps, more edges were found when the number of allowed directions and gradients were greater. In one test map more edges were found when the algorithm started with points marked as 1/2 and in the other algorithm more edges were found when the algorithm started with points marked as 1 for some values of the flags. Since the algorithm is much slower when it starts with points marked as 1/2, in this paper we always start with points marked as 1. Longer edges were found when skipping points was allowed. This is consistent with the findings we have for the averages of the full 50 maps of gaussian temperatures and the combined maps with strings. Since skipping reduces the number of short edges, where the standard deviation is smaller compared to the mean, and thus increases the p-value, it increases the probability that the maps look the same.

the string maps to the Gaussian maps). Finally, we ran simulations allowing for skipping of points in the edge counting algorithm.

Discriminating power was quantified using the *Fisher combined probability test*. This test is applied to the two output histograms of edge lengths, one from the pure Gaussian simulations, the other from the strings plus Gaussian maps. For each length l, we are given the mean number of edges of that length and the corresponding standard deviation. Given the two means and corresponding standard deviations we can apply the t-test to compute the probability p_l that the two means come from the same distribution. The Fisher combined probability method then computes a χ^2 as follows

$$\chi^2_{2k} = -2\sum_{l=1}^{k} ln(p_l) \tag{3.27}$$

where k is the number of edge lengths being considered, and computes the corresponding probability value from a χ^2 distribution with $2k$ values. We chose k to be the last edgelength to have a nonzero standard deviation in either the string or gaussian distributions, whichever is smaller.

The Canny routine makes use of three thresholds. To find the cutoff or top threshold we ran a script to find the maximum average gradient of the fifty string maps and then compared the highest gradient to the highest average gradient. This threshold needs to increase as the $G\mu$ decreases because otherwise one throws out virtually all of the edges, since as $G\mu$ decreases G_m decreases. One needs to keep some edges with values greater than the maximum gradient in any string map because the signal from the gaussian map may add in the same location to the signal from the string map. To find the upper and lower thresholds we ran the Canny algorithm for various thresholds on a pure string map and determined by eye if enough strings could be seen but not so many that the overlap of the edges breaks apart the long string edges. In particular, for $N = 10$ if the thresholds are too small the images are saturated with short edges which break up the long edges. Thus, the thresholds need to be higher

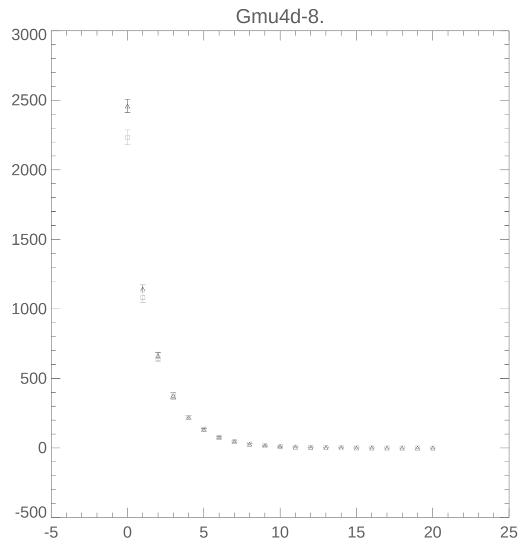

Figure 3.15: Histogram of the edge length distribution of the unsmoothed pure Gaussian maps and the strings plus smoothed Gaussian maps for a value of $G\mu = 4 \times 10^{-8}$. The number of edgelengths for strings plus gaussian maps are denoted by triangles and the squares denote the number of edgelengths for the pure gaussian maps. We plot the means and the standard deviation as the error. Note the systematically larger number of edges for maps with strings for short edgelengths.

for $N = 10$ than for $N = 1$. We leave a detailed optimization of the thresholds to future work.

As a test of the code, we ran the analysis algorithm on two independent sets of fifty Gaussian CMB maps and computed the probability that the two sets come from the same Gaussian ensemble. The resulting probability was typically of the order of 0.7, i.e. within the 1σ error range.

Our simulations show that maps originating from cosmic strings have a larger number of edges than the corresponding pure Gaussian maps. This is a consequence of the presence of the Kaiser-Stebbins edges, the signal we are looking for. Figure 3.15 shows a comparison of the two histograms for the value $G\mu = 4 \times 10^{-8}$. Since the Gaussian noise cuts up the long edges, the difference in edge lengths is statistically significant only for short edges.

Table 3.1 summarizes our results obtained by applying the Fisher combined probability method to the histograms of string edge lengths. The results are for $N = 10$ (10 strings per Hubble volume per Hubble time), for un-smoothed maps, without skipping in the edge drawing and edge counting routines. The statistical analysis includes edgelength 1 data. The first column gives the value of $G\mu$, the second the value of the top threshold (the other two thresholds are held fixed at the values $t_u = 0.25$ and $t_l = 0.1$), the third gives the probability that the histograms of the string and Gaussian maps come from the same Gaussian distribution. The fourth value gives the maximal edge length used in the analysis, and the last column lists the value of a. We see that the cosmic string signal can be detected [8] at a three sigma level down to a value $G\mu = 2 \times 10^{-8}$ which is almost two orders of magnitude better than the current bounds obtained by direct searches, and one order of magnitude better than the limits on $G\mu$ coming from the CMB angular power spectrum constraints. These results are for unsmoothed maps.

As can be expected from looking at the histograms of 3.15, the sensitivity of the algorithm decreases slightly if edges of length 1 are excluded from the analysis. The results excluding edges of length 1 are shown in Table 3.2.

Since smoothing dramatically reduces the number of short edges, and since the strength of the signal of our analysis comes from the number of short edges, it turns out that smoothing significantly weakens the ability of the algorithm to pick out strings. The results of our analysis applied to smoothed maps (smoothing length 3) are given in Table 3.3. The loss in discriminatory power is about a factor of 5. This is a serious concern when considering applications of our algorithm to real data.

In Table 3.4 we present the results for $N = 1$. Since there are an order of magnitude less string edges in this case, the limit on $G\mu$ which can be obtained is slightly weaker (about a factor of 3 weaker). To put this result into context, it is important to point out that limits on $G\mu$ from other studies implicitly

[8] More conservatively, we should say that the difference between the maps with cosmic strings and pure Gaussian maps can be detected.

or explicitly use $N = 10$. The limits on $G\mu$ from matching the angular CMB power spectrum would be weaker by about one order of magnitude.

The results of the previous tables were obtained from an algorithm which did not have any skipping in the edge counting routine. We allowed skipping of two points. Skipping of two points leads to a larger number of long edges. Skipping by four points leads to edge broadening, an unwanted feature. Hence, we only considered skipping two points. Including skipping turns out to reduce the number of short edges more significantly than it increases the number of longer edges. Thus, the power of our routine to discriminate between maps with and without strings slightly decreases when introducing skipping (which is the opposite of what we initially expected). The results are indicated in the following table. However, it is possible that further optimization of the routine parameters would reverse the results concerning the effectiveness of skipping.

Table 3.1:

Unsmoothed String Map versus Gaussian Map: N=10
Minimum Edge Length: 1
$t_u = 0.25$, $t_l = 0.1$, num. skipped points=0

Gmu	t_c	probability	max. edgelength	mean a
1.0000000e-08	7.00000	0.44757170	11.000000	0.99967664
2.0000000e-08	4.00000	0.0020638683	14.000000	0.99862559
4.0000000e-08	3.00000	0.0000000	21.000000	0.99447207
6.0000000e-08	3.00000	0	33	0.98754092

Table 3.2:

Unsmoothed String Map versus Gaussian Map: N=10
Minimum Edge Length: 2
$t_u = 0.25$, $t_l = 0.1$, skipped points=0

Gmu	t_c	probability	max. edgelength	mean a
1.0000000e-08	7.00000	0.56022527	11.000000	0.99967664
2.0000000e-08	4.00000	0.087458606	14.000000	0.99862559
4.0000000e-08	3.00000	4.8140603e-11	21.000000	0.99447207
6.0000000e-08	3.00000	0.0000000	33.000000	0.98754092

Table 3.3:

Minimum Edge Length: 1
Smoothed String Map versus Gaussian Map N=10
$t_u = 0.25$, $t_l = 0.1$, num. skipped points=0

Gmu	t_c	probability	max. edgelength	mean a
6.0000000e-08	3.00000	0.10701445	42.000000	0.98754092
8.0000000e-08	3.00000	0.059179809	46.000000	0.97932855
9.0000000e-08	3.00000	0.00012533417	46.000000	0.97174247
1.0000000e-07	3.00000	2.4759972e-11	52.000000	0.96499435
1.5000000e-07	2.50000	0.0000000	59.000000	0.91936485

Table 3.4:

Minimum Edge Length: 1
Unsmoothed String Map versus Gaussian Map: N=1
$t_u = 0.03$, $t_l = 0.005$, skipped points=0

Gmu	t_c	probability	max. edgelength	mean a
2.0000000e-08	4.00000	0.43985131	7.0000000	0.99986506
4.0000000e-08	3.00000	0.76437603	11.000000	0.99937157
6.0000000e-08	3.00000	0.0019923380	19.000000	0.99901436
8.0000000e-08	3.00000	8.7787192e-09	28.000000	0.99816180
9.0000000e-08	3.00000	3.8369308e-13	32.000000	0.99757307

3.6 Conclusions and Discussion

We have developed a new program to search for cosmic strings in CMB anisotropy maps making use of the Canny algorithm, and have tested it with simulated data corresponding to maps with specifications corresponding to those of current ground-based CMB experiments. The code contains a number of optimization parameters, and we have discussed the role of these parameters.

Our results (based on a rough optimization of the parameters) show that our algorithm has the potential to improve the bounds on the cosmic string tension from direct CMB observations by up to two orders of magnitude compared to existing limits, and by one order of magnitude from other more indirect limits. The limiting value of $G\mu$ decreases as N (the number of strings per Hubble volume per Hubble time) increases. For cosmic superstrings the intercommutation probability may be much lower than for Abelian field theory strings, thus leading to a larger value of N [142]. Hence, our method may

Table 3.5:

Minimum Edge Length: 1
Unsmoothed String Map versus Gaussian Map:N=10
$t_u = 0.25$, $t_l = 0.1$, skipped points=2

Gmu	t_c	probability	max. edgelength	mean a
1.0000000e-08	7.00000	0.43783402	41.000000	0.99967664
2.0000000e-08	4.00000	0.30944903	55.000000	0.99862559
4.0000000e-08	3.00000	5.4179907e-08	139.00000	0.99447207

be able to set more stringent limits of the value of $G\mu$ in the case of cosmic superstrings. [9]

A possible concern with our analysis is that our toy model of representing the effects of a string on the microwave sky introduces artificial edges. Although the presence of the central edge in the CMB pattern of a string is clearly physical, the edges perpendicular to this central edge are due to the toy model which considers finite length string segments rather than a network of infinite strings. Although the temperature perturbation clearly goes to zero at a perpendicular distance t from a string present at time t, the sharpness of the change given by [112] may be modulated by interactions between the time of formation of the string network and the time t [10] . Thus, one of our simulations with N strings per Hubble volume per Hubble time may contain as many edges as a "real" string map with $4N$ strings per Hubble volume per Hubble time. As can be seen by comparing Tables 3.4 and 3.5, the dependence of the limits on $G\mu$ on N is not large. The limit on $G\mu$ appears to scale as N^{-1}. Thus, the limit on $G\mu$ obtained from our analysis might be a factor of 3 too optimistic due to the larger number of edges. This point could

[9] While this manuscript was being prepared for submission, a preprint [69] appeared in which a novel method different from ours was proposed to search for cosmic strings. With this new method, improved limits on the cosmic string tension also appear to be possible.

[10] We thank the Referee for raising this issue.

also be addressed by a Canny algorithm analysis of more sophisticated string simulations, which we shall pursue as a follow-up study.

The results presented here are based on comparing simulations with and without cosmic strings of a known value of $G\mu$. However, we do not know the value of $G\mu$, and the goal of observations is to determine the value or to set limits on it. Hence, the way we plan to apply our algorithm to real data is to compare the edge histograms based on real data with those of a cosmic string plus Gaussian map with fixed $G\mu$, and varying $G\mu$, starting from the current limit for this quantity. Limits on $G\mu$ can be obtained if the histogram derived from the data is statistically different from that of a Gaussian plus strings map for the corresponding value of the normalized string tension. A candidate detection of cosmic strings would require the histogram derived from the real data to be statistically indistinguishable from that of a Gaussian plus strings map, and at the same time different from that of a pure Gaussian map. If there are indeed cosmic strings in the sky with a value of $G\mu$ for which our analysis gives a probability p that the histograms with and without strings are from the same distribution, then the probability that our statistical analysis would give a positive detection of these strings will be $1 - p$.

When applying the algorithm to real data, a serious concern is systematic errors introduced by the observing strategy - specifically lines in the maps due to the scanning strategy. In specific experiments such as the South Pole Telescope (SPT) experiment, lines introduced by the scanning will be in one specific direction, and thus the algorithm can be rendered immune to this effect by considering only edges which are not parallel to the direction of the scanning stripes. Foreground and instrumental noise are other important problems. Smoothing of the maps is supposed to reduce the latter problem, and the study of [173] confirms that instrumental noise such as that anticipated in the SPT telescope will not have a big effect on the power of the algorithm.

The next step of our research program will be to apply our code to existing data. The main challenge will be to take care of the systematic errors contained in the data. We plan to compare data for the actual sky map to Gaussian and

Gaussian plus strings simulations. In order to put the data in a format for which a statistical analysis is possible, we will divide the sky maps into sub-maps of equal size, and treat each sub-map as a different realization of the sky. In other words, we make the ergodic hypothesis and identify ensemble and spatial averaging. Thus, if we want to compare squares of edge length 10^0 in the sky, then we need a total survey area 50 times larger in order to be able to have 50 independent data sets for the sky. We also plan to apply our code to more realistic cosmic string simulations, such as those of [63].

3.7 Appendix A

In this Appendix we describe the maxima doubling problem which arises in our implementation of the Canny algorithm. Let us illustrate the problem in terms of an example.

If the temperature grid points are

$$\begin{array}{cccc} 6 & 8 & 10 & 20 \\ 3 & 5 & 12 & 14 \\ 4 & 6 & 9 & 11 \end{array} \tag{3.28}$$

and the points are labeled starting from 0 from left to right top to bottom, then the point at grid point 5 (temperature 5) is a local maximum with gradient 7 along the 0 direction. The grid point 6 (temperature 12) is a local maximum along the 1 direction with gradient 8. There aren't any doubles in this case.

However, if we had

$$\begin{array}{cccc} 6 & 8 & 10 & 15 \\ 3 & 5 & 12 & 14 \\ 4 & 6 & 9 & 11 \end{array} \tag{3.29}$$

then the grid point 5 (temperature 5) is a local maximum along the 0 direction with a gradient of 7 and the grid point 6 (temperature 12) is a local maximum along the 4 direction with gradient 7. We use a sorting routine to remove the first occurrence of a gradient of 7 (index 5) as we want there to be only one local maximum at this point.

3.8 Summary

In this chapter we explored simulated temperature maps of the CMB in position space to assess the viability of our cosmic string detection program. In the next chapter we shall extend this analysis to determine if cosmic superstrings can be differentiated from generic cosmic strings.

Chapter 4

Searching for Signatures of Cosmic Superstrings in the CMB

4.1 Preface

In this chapter, we include [53] which builds upon the last chapter by searching for signatures of cosmic superstrings via their influence on the CMB per the Kaiser-Stebbins effect. We do this by examining the density distributions of edges, as superstrings can form three-string junctions. Three-string junctions result in a distribution of edges featuring clustering and voids. Similar patterns can be found from different scaling solutions of cosmic strings also allowing us to distinguish among different scaling solutions.

4.2 Introduction

In recent years there has been a revival in interest in finding signatures of cosmic strings. One of the main reasons is that a large class of string inflationary models predict [157] a copious production of cosmic superstrings [193] - cosmic strings consisting of extended fundamental strings of cosmological scale - at the end of the period of inflation. Under certain conditions [47], these cosmic superstrings are stable on cosmological time scales.

Since gauge theories also predict the presence of cosmic strings [95, 198, 184, 97, 96] (see [187, 75, 28] for reviews), it is an important endeavor to distinguish between generic cosmic strings and cosmic superstrings. As we shall demonstrate in this note, the plethora of small scale Cosmic Microwave Background (CMB) experiments, such as the ground based Atacama Cosmology Telescope (ACT) [102] and the South Pole Telescope (SPT) [151] or the Planck satellite experiment [190, 125], will provide the observational means to make this distinction.

Both generic cosmic strings and cosmic superstrings leave imprints in the CMB. The key signature - the "Kaiser-Stebbins (KS) effect" [89] - consists of line discontinuities in the temperature map formed from a combination of gravitational lensing and the Doppler effect: photons from the last scattering surface streaming by either side of a moving cosmic string will be observed to have a temperature which differs by a small amount proportional to the string tension. The signature is manifest in position space - in Fourier space the phase information which is crucial to obtain a line discontinuity is lost. Therefore, to find evidence for the line discontinuities, new data analysis techniques are required which work directly in position space. One such technique is the Canny edge detection algorithm [37, 36]. As shown in [6, 173, 52], the Canny algorithm can be used to search for the line discontinuities produced by strings. In fact, it was shown that when applied to data with angular resolution comparable to that which will be obtained from the South Pole Telescope, the non-detection of KS lines will allow an improvement in the upper bound on the cosmic string tension by almost an order of magnitude compared to existing bounds.

One essential distinction between strings in simple gauge theory models and cosmic superstrings is that the latter come in different varieties [1] . There can

[1] For sufficiently complicated gauge theory models, it is also possible to obtain different types of strings [74, 35]. Fat strings arising in theories with

be fundamental strings (F-strings), one space-dimensional branes (D-strings), and bound states of the above. These flavors of cosmic superstrings can form junctions, points where three strings meet in the shape of a Y [47, 106, 82, 70, 73, 45, 46, 48, 181].

In the present paper we find that the Canny algorithm can be modified in order to allow a differentiation between string maps with and without string junctions. Since string junctions are generically predicted in models of brane inflation with cosmic superstrings but are not present for cosmic strings in simple gauge theory models, our work points towards a way of finding observational evidence which would favor cosmic superstrings over simple gauge theory strings.

To identify the line discontinuities predicted by cosmic strings, good angular resolution of a CMB experiment is crucial. It is for this reason that our simulations work with maps similar in angular extent and angular resolution which will be obtained by the ACT and SPT experiments, those with ideal angular resolution.

Our implementation of the Canny algorithm [52] finds line discontinuities produced by the KS effect and produces a map of edges. In contrast to previous work [138, 195, 62, 164, 18, 19, 8, 9] on constraining the cosmic string tension from CMB observations which focused on the angular power spectrum of CMB maps in which the KS signature is washed out, our work searches specifically for the line discontinuities predicted by the KS effect.

Our numerical work is based on simulations of the predicted CMB anisotropies in small patches of the sky (side length 10^o) with angular resolution of $1.5'$. We simulate maps predicted in pure string models (i.e. no "Gaussian noise")

---

light moduli fields also can give rise to junctions [49] - in this case due to mergings of strings with low winding number into strings of higher winding number. For simple gauge theory strings, strings with higher winding number are unstable to the fragmentation into strings of winding number 1, and hence these junctions do not arise.

with and without junctions, and also maps in which the "Gaussian noise" due to inflationary perturbations dominates the total amplitude of the power spectrum, and cosmic strings contribute a sub-dominant fraction consistent with the current upper bounds [138, 195, 62, 164, 18, 19, 8, 9]. The current upper bound on the contribution of strings to the angular power spectrum of CMB anisotropies corresponds to a value of the string tension μ which is $G\mu < 2 \times 10^{-7}$ in dimensionless units (G is Newton's gravitational constant).

Our implementation of the Canny algorithm consists of a set of routines which generate a map of edges in the sky corresponding to gradients in CMB maps which are in the range expected from the KS effect [52], and statistically analyze the resulting edge maps, with the goal of distinguishing between simulated CMB maps of pure Gaussian inflationary perturbations and maps combining simulated cosmic strings with Gaussian perturbations. In our studies [52] we showed that this distinction could be made up to a three sigma confidence level for strings with tensions as low as 2×10^{-8} for maps without the removal of point source noise (unsmoothed) and as low as 9×10^{-8} for maps with point source noise removed (smoothed).

Here we extend the use of the Canny algorithm to distinguish simulated maps of strings with and without junctions. Based on the edge maps which the Canny algorithm produces, we count the number of edges present in groups of pixels, thus determining the density of edges. We then use the distribution of densities to differentiate between maps with and without junctions. Specifically, we compare the shapes of the histograms (number of occurrences versus number of edges) in the two cases, using the "combined Fisher probability method".

The simulations contain various free parameters. Firstly, there is the cosmic string tension μ. Secondly, there is the number N of string segments per Hubble volume per Hubble time during the string scaling phase. The fraction of string segments which involve a junction is another choice which must be made. In order to ascertain that a deviation in the shape of an edge histogram from that in a theory with pure Gaussian noise is a consequence of strings with junctions, we must allow the parameters in the simulations with and without junctions to be different. For example, it is not sufficient to show that the histogram in a string simulation with junctions for $N = 10$ is different from that of a string simulation without junctions for the same value of N. We must also check that the change in the shape resulting from the addition of junctions cannot be masked by a change in the value of N. We have carefully studied this point and find that, with appropriately chosen number of boxes sampled in the observed window, we are able to differentiate string simulations with and without junctions. Without Gaussian noise the difference in the shape of the histogram is manifest. However, with Gaussian noise consistent with the cosmic strings contributing not more than they are allowed to by the limits of [138, 195, 62, 164, 18, 19, 8, 9] we find that the difference is no longer manifest. However, with sufficient care, we are still able to make the statistical distinction.

The outline of this paper is as follows: we first describe our simulated microwave sky patches resulting from models with cosmic strings junctions (Section 4.3). In Section 4.4 we review the application of the Canny algorithm and present the edge maps which result from our simulations. We present the density distribution analysis in Section 4.5. Finally, in Section 4.6 we conclude with a discussion of the results.

4.3 Simulations

We refer the reader to [52] for details on simulating the combined maps produced by the combination of cosmic strings and inflationary perturbations. In brief, the contribution of Gaussian inflationary perturbations to the CMB sky map is produced by Fourier transforming the angular power spectrum C_l obtained using the CAMB code [107], assuming random phases.

The temperature map from pure cosmic strings is constructed using an analytical toy model of the effects of strings on the microwave sky. This model was first introduced in [133, 134] to model the effects of long strings, and has been used widely since then. The model assumes that the distribution of cosmic strings obeys a scaling solution (i.e. the network looks the same at all times if distances are scaled to the Hubble radius). The string network consists of "long" strings (strings whose curvature radius is comparable or larger than the Hubble radius) and loops (of radius smaller than the Hubble length). Based on numerical simulations of the evolution of a cosmic string network [4, 16, 5, 150, 183] we assume that the long strings dominate. We also assume that the long strings are straight. Thus, according to the model of [133, 134], the network of strings can be modelled as a set of straight string segments of roughly Hubble length. The various cosmic string simulations all agree that there is a scaling solution for the network of long strings, but they do not agree on the density of strings. We will model this uncertainty with a free parameter N, an integer which gives the number of string segments per Hubble volume. Since the strings move relativistically, the network of strings looks uncorrelated on time scales larger than the Hubble time. Following [133, 134], we model this by taking the string segments to be statistically independent in each Hubble time step. The strings are laid down in Hubble time steps from the time of recombination to the present time.

Each string segment produces a characteristic rectangular temperature fluctuation pattern in the sky which is obtained by adding

$$\Delta T/T \;=\; 4\pi G\mu\tilde{v}r \tag{4.1}$$

on one side of the location of the string, affecting the sky to a depth of a Hubble length [2] and subtracting this value from the other side. Here μ is the string tension, $\tilde{v} \equiv v\gamma(v)$ where v is the transverse velocity of the string and its relativistic γ factor is $\gamma(v)$, and r is a random number between 0 and 1

[2] The range of the "deficit angle" [185] in the plane perpendicular to the string which leads to the KS effect is bounded from above by causality to be the Hubble length - assuming that the cosmic strings are produced in a phase transition in the early universe - and the work of [112] shows that the effect of the deficit angle in fact extends just about to the causality limit.

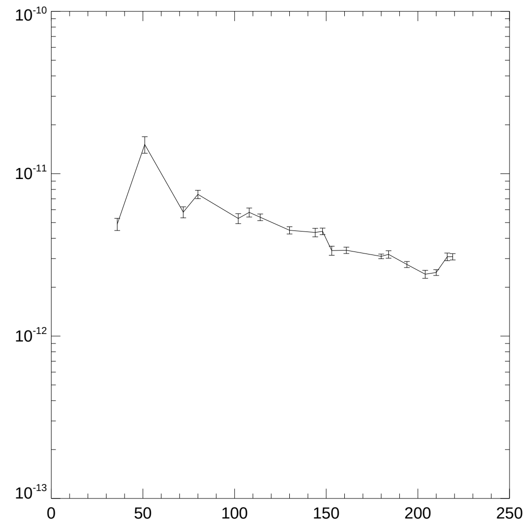

Figure 4.1: The angular power spectrum of the CMB anisotropy maps of pure cosmic string simulations with values N=10 and $G\mu = 1\times10^{-7}$. The horizontal axis is l, the vertical axis is $l(l+1)C_l$.

which is introduced to take into account projection effects and the fact that the velocities of different strings will vary - in (4.1) we use one fixed velocity v. We will speak in terms of a pattern of rectangular "boxes" (one on each side of the string) which a string produces in the CMB sky. One difference between this simulation and that of [52] is that in the former paper the length of the string segment laid down was the same length as the depth of the box perpendicular to the string. In this simulation we allow the depth of the box affected by the string to be a different random fraction of the Hubble length (as determined by projection effects). Our cosmic string toy model yields an approximately scale-invariant spectrum of CMB anisotropies (as expected from early analytical work on cosmic strings [180, 158, 171, 33, 179, 135, 118]). The C_l spectrum for 100 string simulations of string tension $G\mu = 1 \times 10^{-7}$ is shown in Figure 4.1.

Since we have applications to small angular scale CMB experiments such as ACT and SPT in mind, we take our window size to be 10 degrees and the resolution to be 1.5 arcminutes.

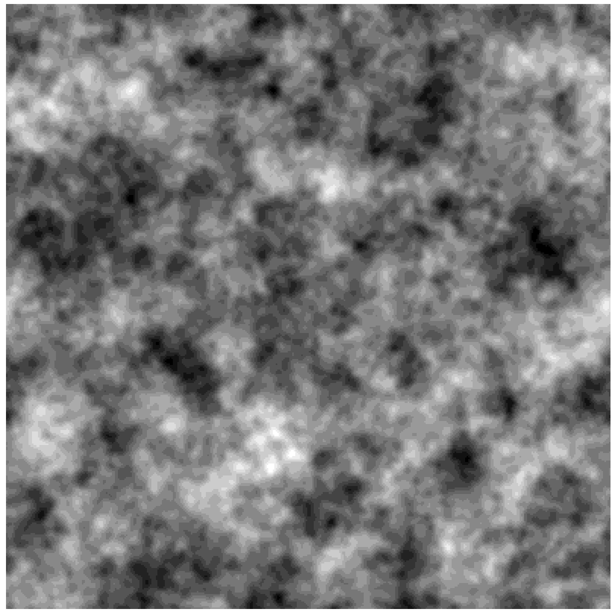

Figure 4.2: Temperature map in a model with both cosmic strings ($N = 10$ and $G\mu = 10^{-7}$, no junctions) and Gaussian fluctuations.

To sum the Gaussian and cosmic string maps we multiply the COBE-normalized Gaussian map by a coefficient a and add the cosmic string temperature map obtained for the value of $G\mu$ which we are interested in:

$$T_{(G+S)} \; = \; aT_{(G)} + T_{(S)}. \tag{4.2}$$

The coefficient a is obtained by demanding that the total map yields the best fit to the observed angular CMB correlation function.

We refer the reader to Figure 4.2 for the simulated map of cosmic strings (no junctions) plus Gaussian inflationary perturbations. The map is for a value $G\mu = 10^{-7}$.

Next we describe the simulations in the presence of junctions. The first difference is that not all strings have the same tension. By μ_i we will denote the tension of the i'th string. The vector $\boldsymbol{\mu_i}$ has magnitude μ_i and points in direction of the string. We will take the total number of string segments per Hubble volume to be $N = 10$. We assume junctions in the shape of a "Y", i.e. junctions with three legs each. Thus, there will be one string segment per Hubble volume which is not part of a junction.

As in the string simulation without junctions, the beginning of the first string in the junction is placed randomly within a window extending by one Hubble length in each direction around the observed window. This accounts for strings which might begin within the field of view and extend out of it and for strings which might begin outside the field of view and extend into the observed window. The first string's starting point in this simulation will be the point where the three strings meet. The angle and sign of its velocity vector as well as the direction of the string are randomly determined. The string's velocity angle and sign determine which of the two boxes around the string will be assigned a positive and which a negative temperature fluctuation compared to the average. The formula (4.3) taken from [24] to determine which side of the string has a positive temperature difference compared to the average is:

$$\frac{\delta T}{T} = 8\pi G\gamma|\boldsymbol{v} \cdot (\boldsymbol{\mu_i} \times \boldsymbol{k})| \tag{4.3}$$

in which $\boldsymbol{v}$ is the velocity vector of the string, and $\boldsymbol{k}$ is the line of sight unit vector perpendicular to the observation window.

The first string segment of a junction has a fixed input string tension. We use $G\mu = 8.7 \times 10^{-8}$ because when there are three junctions per Hubble volume this gives a coefficient $a = 0.976$. Recall that a is the coefficient used to sum the Gaussian contribution of the map with the string map. A value of $a = 0.976$ is obtained in the case of a simulation with $G\mu = 1 \times 10^{-7}$ for $N = 10$ without junctions. We want to compare different maps with the same contribution from the Gaussian perturbations. Therefore we fix a and compute the corresponding $G\mu$ for simulations with junctions and varying values of N. To determine the value of $G\mu$ for a simulation with junctions, we first perform a simulation with a given value $G\mu_0$ and compute the resulting value of a, denoted here by a_0. The value of $G\mu$ which yields the required value of a is

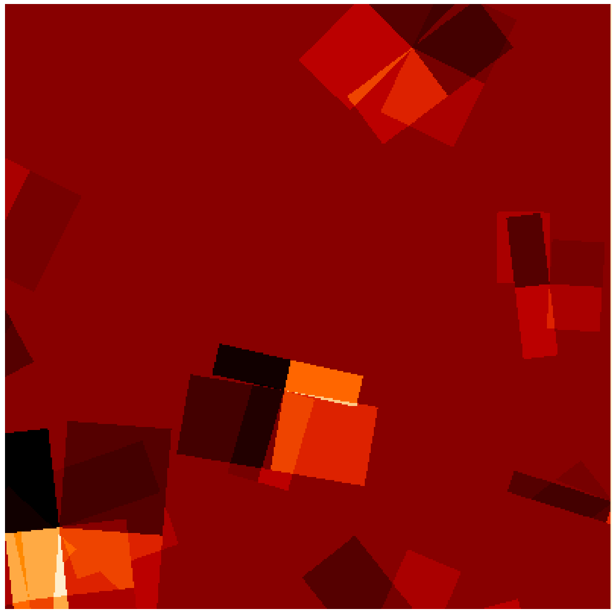

Figure 4.3: A few cosmic strings with junctions.

then given by:

$$G\mu^2 = \left(\frac{a^2-1}{a_0^2-1}\right)(G\mu_0^2)\,. \tag{4.4}$$

The value of a for a given string tension and given value of N will be higher than in our previous paper [52] since the boxes of altered temperature per the KS effect are smaller in this simulation where the depth can be less than the string width. Hence, the strings contribute less power.

When simulating junctions, we draw the second string at the same point as the beginning of the first string with a string tension given by a random fraction of the first string's tension. The direction of the second string is random. The third string's direction is chosen such that the vector sum equals zero for the three vectors with magnitudes given by the string tensions and directions given by the directions of the strings. The magnitude of this third vector indicating the direction of the third string gives the string tension for the third string. Figure 4.3 demonstrates the temperature signature for a few strings with junctions.

As in our previous paper [52] we lay down strings independently in each Hubble expansion time interval starting from recombination until the present

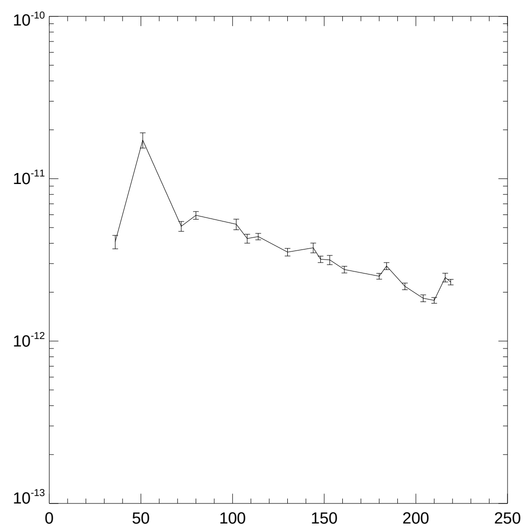

Figure 4.4: The angular power spectrum of the CMB anisotropy maps for cosmic string simulations with three junctions per Hubble volume and a scaling solution with $N = 10$ and $G\mu = 8.7\times10^{-8}$. The horizontal axis is l, the vertical axis is $l(l+1)C_l$.

time. Figure 4.4 shows the resulting angular power spectrum (C_l spectrum) for a scaling solution of $N = 10$, a string tension of the first string as $G\mu = 8.7 \times 10^{-8}$ and three junctions per Hubble volume. The value of the string tension without junctions was chosen to lie slightly below the current best upper limits; the string tension for simulations with junctions was then selected to have the same contribution of the background Gaussian perturbations.

4.4 Canny Algorithm

We refer the reader to [52] for a thorough discussion of our application of the Canny algorithm. In essence, we look for edges by searching for maximal gradients larger than a threshold t_u. These local maxima are perpendicular to the direction of the edge. Gradients larger than a cutoff value, t_c, are removed as these will likely be due to the underlying Gaussian perturbations. Gradients that are between the upper threshold and a lower threshold are marked with a value of one and counted as part of an edge if they are connected to a point in a satisfactory direction (perpendicular or near perpendicular) whose gradient is

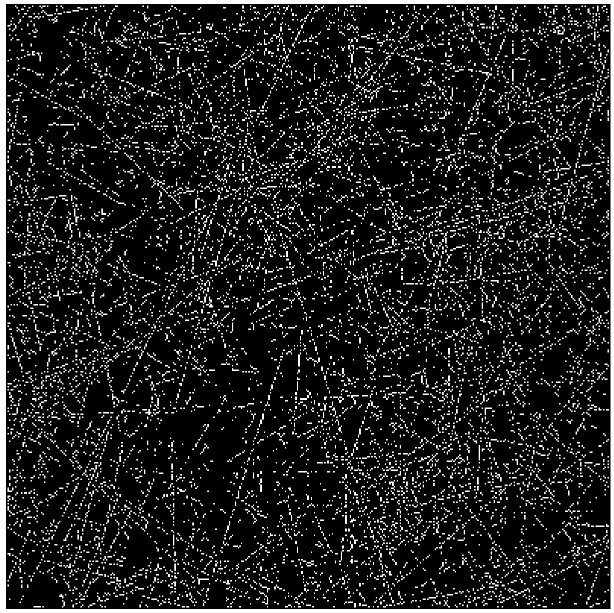

Figure 4.5: Pure string edge map without junctions obeying a scaling solution of N=10.

a local maximum greater than or equal to the upper threshold. Our algorithm creates a map of edges, or a map of points which are marked as one connected together in edges. These can be seen for strings without junctions obeying a scaling solution of $N = 10$ in Figure 4.5 and strings with three junctions per Hubble volume obeying a scaling solution of $N = 10$ in Figure 4.6. Once an edge map has been created the program counts the number of continuous points that satisfy the above criteria, thus counting the number of points in the edges.

In our simulations, we have chosen the following values of the cutoff parameters which enter the Canny algorithm: the top cutoff is $t_c = 3$ [3] , the upper cutoff is $t_u = 0.25$ and the lower cutoff is $t_l = 0.1$. These values were chosen based on the parameter optimization performed in our previous work [52].

[3] In units of the maximal gradient which can be produced in the simulation by a cosmic string.

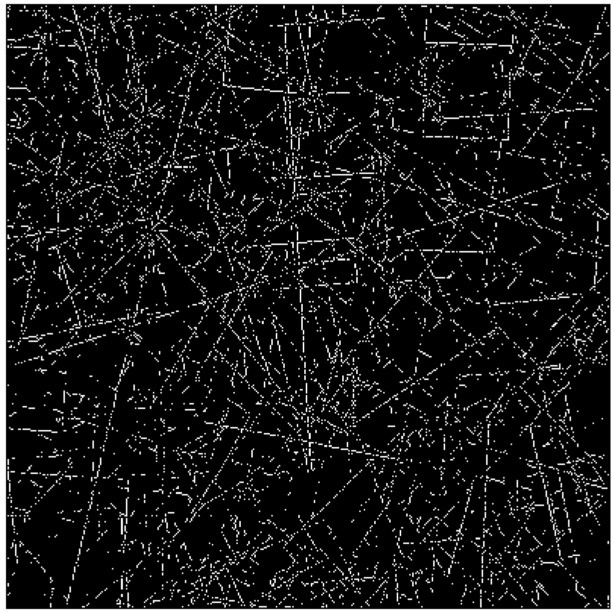

Figure 4.6: Cosmic string edge map with three junctions per Hubble volume obeying a scaling solution of N=10.

4.5 Density Distribution Analysis

Because strings with junctions are grouped together, we hypothesized that the distribution of edges with junctions would differ from the distribution without junctions. We divided the observation window by a grid into boxes and counted the number of edges and number of points marked as one (the number of pixels in edges) per grid box. The size of a grid box is a free parameter in our analysis. We then plotted the number of boxes versus the number of either edges or points marked as one per box. Using the number of edges or the number of points marked as one per box gives slightly different statistics.

When we count the number of edges in a given grid box, we need an algorithm to determine which box an edge falls within when edges cross boxes. We choose to assign an entire edge to the box containing a specific pixel of that edge. We could use the first pixel as the point denoting the edge, but this introduces a position bias because the algorithm counts edges starting from the bottom left of the window. However, when searching for pixels to include in an edge, the algorithm does not search in a linear fashion so the final pixel included in an edge does not have a biased position relative to the other pixels in the edge. Therefore, we assign the position of the edge to the final pixel.

We now discuss our numerical results. All of the simulations were for the same value of a. In all the following figures the blue (solid) curve is for $N = 10$ with three junctions per Hubble volume. The other curves correspond to cosmic string simulations without junctions, the red innermost (dash dot dot) curve is for $N = 1$, the yellow (dashed) one is for $N = 6$, the green (dot-dashed) one is for $N = 5$, and the outermost red (dotted) one is for $N = 10$. All curves correspond to the average over 100 edge maps. Note that the $N = 10$ curve with junctions is closest to the $N = 5$ curve without junctions.

The statistic we use to determine if the curves are distinguishable is a combination of the Student t-test and the Fisher combined probability test. For each value of the x-axis (the number of points marked as one or the number of edges) we are given the mean number of boxes that contain that number of points/edges and the standard deviation. With two means and corresponding standard deviations we can apply the t-test to compute the probability p_l that the two means originate from the same distribution. The Fisher combined probability method then computes χ^2 as follows:

$$\chi^2_{2k} = -2 \sum_{l=1}^{k} \ln(p_l) \tag{4.5}$$

where k is the maximal number of edges/points marked as one being which arise. We compute the probability value from the χ^2 distribution with $2k$ values. Bins with entries or standard deviations equal to zero are obviously not included in the sum.

Figures 4.7-4.10 are pure string (no Gaussian added) histograms. We see that for the different scaling solutions the peak and the width of the curves are shifted. We also see that it is difficult to distinguish by eye between the scaling solution $N = 5$ without junctions and $N = 10$ with junctions, but that using the Fisher probability method these curves are clearly distinguishable.

We also see that as we change the box size (or the number of boxes in the grid) the results differ. This opens up the possibility to probe the difference between two sky maps using a set of different statistics. One statistic may be more powerful at distinguishing the map with string junctions from a map without junctions for one value of N, while another statistic may yield a stronger discrimination for another value of N.

In Figure 4.7 we divide the observation window into 36 by 36 size boxes and plot the number of boxes for pure string maps (without Gaussian contribution) versus the number of *points marked as one* in each box. Table 4.1 shows the corresponding probabilities for the junction maps to have come from the same distribution as the corresponding string maps without junctions for various scaling solutions. In the table, each line corresponds to a different comparison. The first column gives the parameters of the simulation with junctions (which are always taken to be the same), the second column states the parameters of the simulation without junctions which the run indicated in the first column is compared to. The third line gives the probability that the two maps come from the same distribution. A probability of zero means that the numerical result is smaller than the numerical cutoff.

Figure 4.8 plots the same as above except that the grid is divided into 26 by 26 boxes. Table 4.2 displays the results for this figure.

Figure 4.9 plots the histogram of the number of boxes versus the number of *edges* for 36 by 36 boxes in the grid. Table 4.3 displays the statistical results for this figure. We see that using *edges* instead of *number of points* yields an improved discriminatory power.

Figure 4.10 plots the histogram for the number of boxes versus the number of edges for 26 by 26 boxes in the grid with Table 4.4 giving the corresponding statistical results.

Figures 4.11-4.14 with corresponding Tables 4.5-8 give the results for the string maps with Gaussian added. The string tensions are adjusted so that the a coefficient remains the same for each scaling solution, hence keeping the percentage of the Gaussian contribution constant. We choose the baseline a

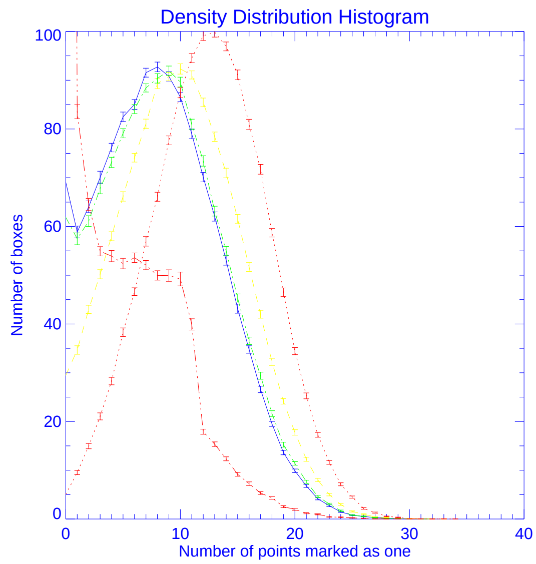

Figure 4.7: Pure string histograms for 36×36 boxes. Number of boxes versus the number of points marked as one. The red innermost curve (dash dot dot) is the average over 100 edge maps for $N = 1$, the blue curve (solid) is for $N = 10$ with three junctions per Hubble volume, the yellow curve (dashed) is for $N = 6$, the green curve (dash dot) is for $N = 5$, and the outermost red curve (dotted) is for $N = 10$. Only the blue curve includes the presence of junctions. See Table 4.1 for string tensions and a coefficient.

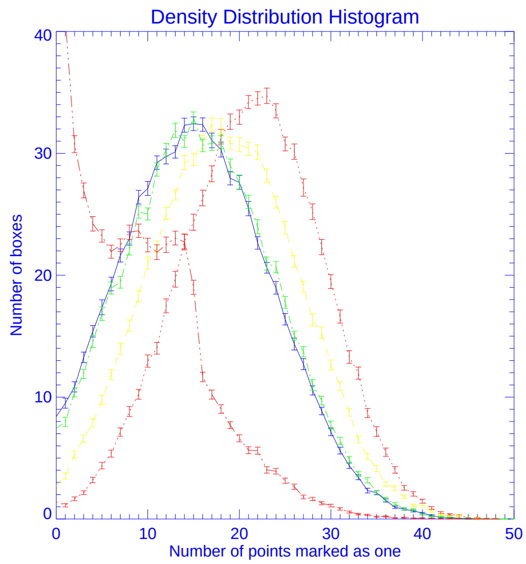

Figure 4.8: Pure string histograms for 26×26 boxes. Number of boxes versus the number of points marked as one. The red innermost curve (dash dot dot) is the average over 100 edge maps for $N = 1$, the blue curve (solid) is for $N = 10$ with three junctions per Hubble volume, the yellow curve (dashed) is for $N = 6$, the green curve (dash dot) is for $N = 5$, and the outermost red curve (dotted) is for $N = 10$. Only the blue curve includes the presence of junctions.

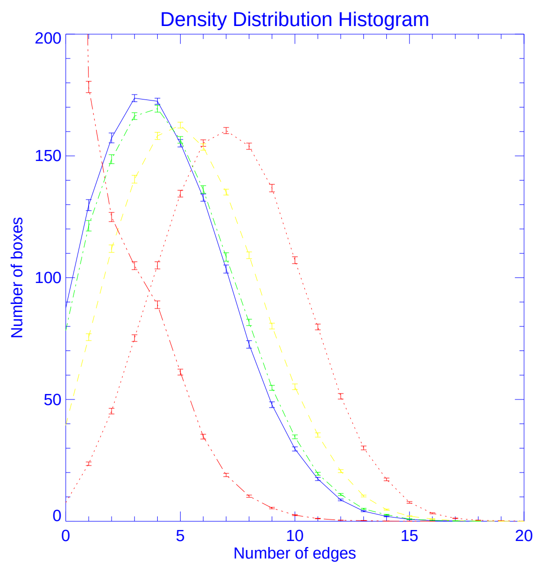

Figure 4.9: Pure string histograms for 36×36 boxes. Number of boxes versus the number of edges. The red innermost curve (dash dot dot) is the average over 100 edge maps for $N = 1$, the blue curve (solid) is for $N = 10$ with three junctions per Hubble volume, the yellow curve (dashed) is for $N = 6$, the green curve (dash dot) is for $N = 5$, and the outermost red curve (dotted) is for $N = 10$. Only the blue curve includes the presence of junctions.

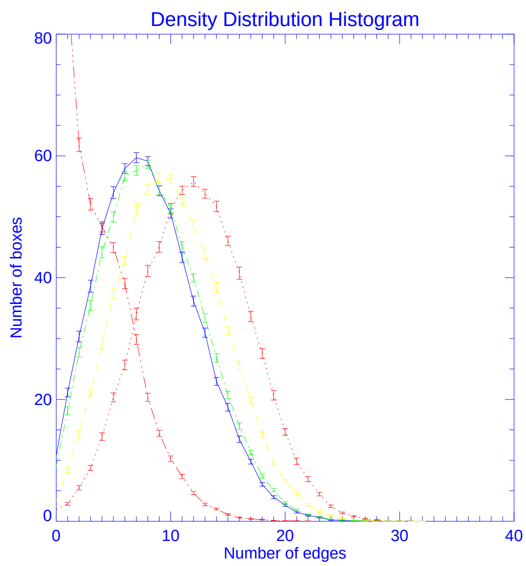

Figure 4.10: Pure string histograms for 26×26 boxes. Number of boxes versus the number of edges. The red innermost curve (dash dot dot) is the average over 100 edge maps for $N = 1$, the blue curve (solid) is for $N = 10$ with three junctions per Hubble volume, the yellow curve (dashed) is for $N = 6$, the green curve (dash dot) is for $N = 5$, and the outermost red curve (dotted) is for $N = 10$. Only the blue curve includes the presence of junctions.

Table 4.1:

Probabilities that Maps with Junctions come from same Distribution as Maps without Junctions for Pure Strings
Based on the distribution of points marked as 1
$a = 0.976$ 36x36 Boxes Per window

N	$G\mu$	junctions	N	$G\mu$	junctions	probability
10	8.7×10^{-8}	yes	10	1×10^{-7}	no	0
10	8.7×10^{-8}	yes	6	1.2×10^{-7}	no	0
10	8.7×10^{-8}	yes	5	1.37×10^{-7}	no	5×10^{-9}
10	8.7×10^{-8}	yes	1	3.12×10^{-7}	no	0

Table 4.2:

Probabilities that Maps with Junctions come from same Distribution as Maps without Junctions for Pure Strings
(Based on the distribution of points marked as 1)
$a = 0.976$ 26x26 Boxes Per window

N	$G\mu$	junctions	N	$G\mu$	junctions	probability
10	8.7×10^{-8}	yes	10	1×10^{-7}	no	0
10	8.7×10^{-8}	yes	6	1.2×10^{-7}	no	0
10	8.7×10^{-8}	yes	5	1.37×10^{-7}	no	3×10^{-6}
10	8.7×10^{-8}	yes	1	3.12×10^{-7}	no	0

coefficient to be consistent with the string tension limits given by Pogosian, Wasserman, and Wyman (see the corresponding reference in the list [138, 195, 62, 164, 18, 19, 8, 9]).

In Figure 4.11 the number of boxes versus number of points marked as one is plotted for 36 by 36 size boxes in a grid. We can easily distinguish between scaling solutions of $N = 10$, $N = 6$, and $N = 1$ of maps without junctions compared to maps with three junctions per Hubble volume. With fixed 36 by 36 boxes in a 10 degree window, maps with $N = 5$ are indistinguishable from maps of $N = 10$ with three junctions per Hubble volume, as can be seen in Table 4.5.

However, here is where our power of being able to use a set of different statistics comes in handy. In Figure 4.12, corresponding to Table 4.6, we use 26 by 26 size boxes in a grid. Now, the results for $N = 5$ are distinguishable from those in simulations with junctions, but the $N = 10$ junction simulation results

Table 4.3:

Probabilities that Maps with Junctions come from same Distribution as Maps without Junctions for Pure Strings
(Based on the distribution of edges)
$a = 0.976$ 36x36 Boxes Per window

N	$G\mu$	junctions	N	$G\mu$	junctions	probability
10	8.7×10^{-8}	yes	10	1×10^{-7}	no	0
10	8.7×10^{-8}	yes	6	1.2×10^{-7}	no	0
10	8.7×10^{-8}	yes	5	1.37×10^{-7}	no	0
10	8.7×10^{-8}	yes	1	3.12×10^{-7}	no	0

Table 4.4:

Probabilities that Maps with Junctions come from same Distribution as Maps without Junctions for Pure Strings
(Based on the distribution of edges)
$a = 0.976$ 26x26 Boxes Per window

N	$G\mu$	junctions	N	$G\mu$	junctions	probability
10	8.7×10^{-8}	yes	10	1×10^{-7}	no	0
10	8.7×10^{-8}	yes	6	1.2×10^{-7}	no	0
10	8.7×10^{-8}	yes	5	1.37×10^{-7}	no	8×10^{-16}
10	8.7×10^{-8}	yes	1	3.12×10^{-7}	no	0

and the $N = 6$ no junction scaling solution are no longer distinguishable. With the combined results for both 36 by 36 and 26 by 26 size boxes we can distinguish maps with junctions from maps without junctions for strings plus Gaussian fluctuations for all values of N. The explanation for our results is that the edges cluster differently on different length scales for simulations with and without junctions.

A slightly different analysis is to consider the distribution of edges versus the number of pixels in edges. With junctions we expect the edges to be longer and therefore less dense in number than the number of edges for maps without junctions. Figure 4.13 and its corresponding Table 4.7 indicate the results for number of boxes versus number of edges for 36 by 36 size boxes. From these results maps with junctions are indistinguishable from maps of a no-junction scaling solutions with $N = 6$. However, Figure 4.14 and its corresponding Table 4.8 show that by plotting the number of boxes versus number of edges

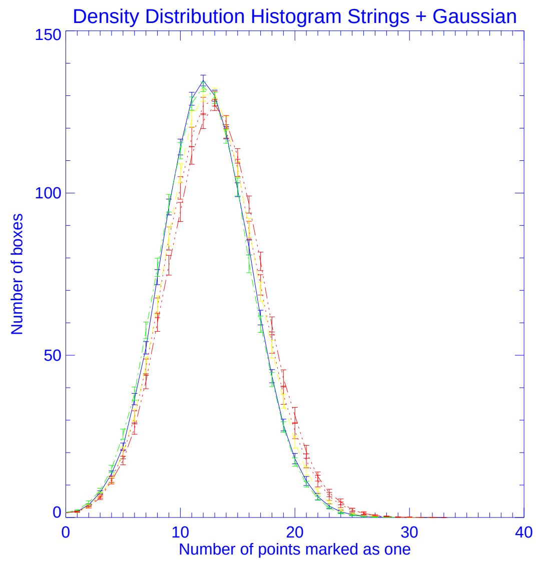

Figure 4.11: Strings plus Gaussian histogram for 36×36 boxes. Number of boxes versus the number of points marked as one. The red curve (dash dot dot) is the average over 100 edge maps for $N = 1$, the blue curve (solid) is for $N = 10$ with three junctions per Hubble volume, the yellow curve (dashed) is for $N = 6$, the green curve (dash dot) is for $N = 5$, and the outermost red curve (dotted) is for $N = 10$. Only the blue curve includes the presence of junctions.

for 26 by 26 size boxes, maps with junctions become distinguishable from maps without junctions for all scaling solutions we considered.

4.6 Conclusions

We have applied the Canny algorithm to simulated maps of CMB anisotropies induced by models with cosmic stings either containing or not containing string junctions. We proposed a statistic with which it should be possible to distinguish between the maps with and without junctions. This provides a method with which one can distinguish between the predictions of simple gauge field theory models with cosmic strings (which typically do not admit string junctions), and models such as those giving rise to cosmic superstrings, which are characterized by the presence of junctions.

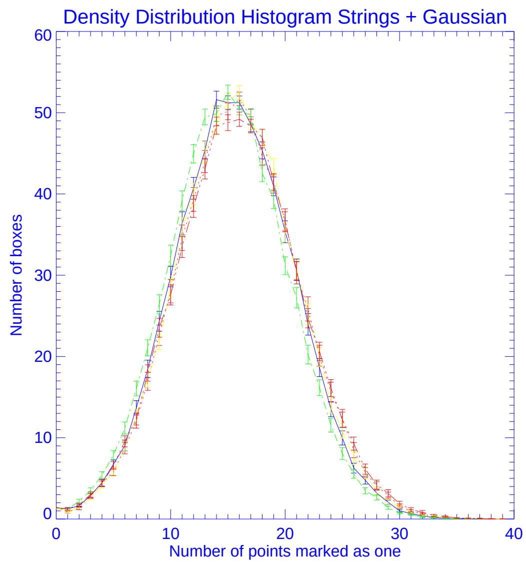

Figure 4.12: String plus Gaussian histogram for 26×26 boxes. Number of boxes versus the number of points marked as one. The red curve (dash dot dot) is the average over 100 edge maps for $N = 1$, the blue curve (solid) is for $N = 10$ with three junctions per Hubble volume, the yellow curve (dashed) is for $N = 6$, the green curve (dash dot) is for $N = 5$, and the outermost red curve (dotted) is for $N = 10$. Only the blue curve includes the presence of junctions.

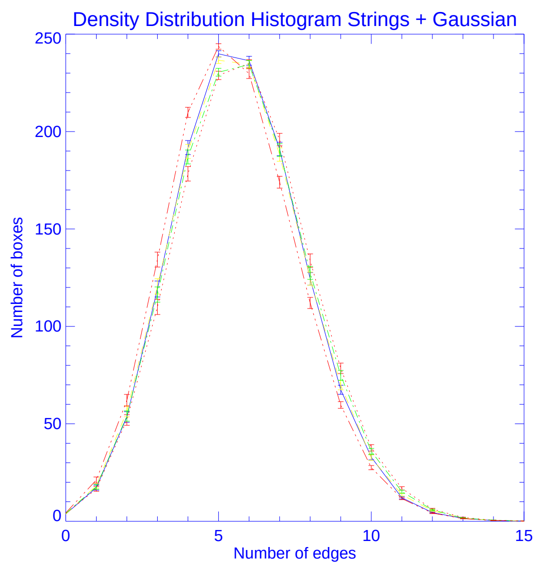

Figure 4.13: String plus Gaussian histogram for 36×36 boxes. Number of boxes versus the number of edges. The red curve (dash dot dot) is the average over 100 edge maps for $N = 1$, the blue curve (solid) is for $N = 10$ with three junctions per Hubble volume, the yellow curve (dashed) is for $N = 6$, the green curve (dash dot) is for $N = 5$, and the outermost red curve (dotted) is for $N = 10$. Only the blue curve includes the presence of junctions.

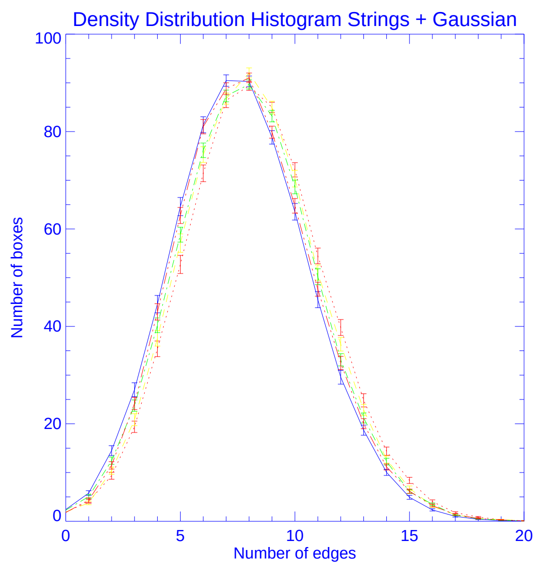

Figure 4.14: String plus Gaussian histogram for 26×26 boxes. Number of boxes versus the number of edges. The red curve (dash dot dot) is the average over 100 edge maps for $N = 1$, the blue curve (solid) is for $N = 10$ with three junctions per Hubble volume, the yellow curve (dashed) is for $N = 6$, the green curve (dash dot) is for $N = 5$, and the outermost red curve (dotted) is for $N = 10$. Only the blue curve includes the presence of junctions.

Table 4.5:

Probabilities that Maps with Junctions come from same Distribution as Maps without Junctions for Strings with Gaussian
(Based on the distribution of points marked as 1)
$a = 0.976$ 36x36 Boxes Per window

N	$G\mu$	junctions	N	$G\mu$	junctions	probability
10	8.7×10^{-8}	yes	10	1×10^{-7}	no	3.2×10^{-13}
10	8.7×10^{-8}	yes	6	1.2×10^{-7}	no	3.6×10^{-6}
10	8.7×10^{-8}	yes	5	1.37×10^{-7}	no	0.79
10	8.7×10^{-8}	yes	1	3.12×10^{-7}	no	0

Table 4.6:

Probabilities that Maps with Junctions come from same Distribution as Maps without Junctions for Strings with Gaussian
(Based on the distribution of points marked as 1)
$a = 0.976$ 26x26 Boxes Per window

N	$G\mu$	junctions	N	$G\mu$	junctions	probability
10	8.7×10^{-8}	yes	10	1×10^{-7}	no	0.069915751
10	8.7×10^{-8}	yes	6	1.2×10^{-7}	no	0.70260790
10	8.7×10^{-8}	yes	5	1.37×10^{-7}	no	7.7×10^{-7}
10	8.7×10^{-8}	yes	1	3.12×10^{-7}	no	0.00011939824

We first showed that our statistic is able to clearly differentiate between string maps with and without junctions in the absence of Gaussian noise. However, since we know that a cosmic string model without a dominant Gaussian contribution to the spectrum of fluctuations is not consistent with the latest data on the angular power spectrum of CMB anisotropies, we need to consider correctly normalized sky maps which contain strings with a tension sufficiently low such that its contribution to the power spectrum does not exceed the current limits [138, 195, 62, 164, 18, 19, 8, 9], with the bulk of the power coming from Gaussian noise. In this case it is more difficult to differentiate between maps where the strings have junction and where they do not.

Nevertheless, making use of our detailed statistics, we found a clear distinction in the shape (peak and width) of the density distribution (number of boxes sampled with varying numbers of edges or pixels in the edges) for the different scaling solutions. For example, $N = 1$ strings per Hubble volume had

Table 4.7:

Probabilities that Maps with Junctions come from same Distribution as Maps without Junctions Strings with Gaussians
(Based on the distribution of edges)
$a = 0.976$ 36x36 Boxes Per window

N	$G\mu$	junctions	N	$G\mu$	junctions	probability
10	8.7×10^{-8}	yes	10	1×10^{-7}	no	7.46×10^{-11}
10	8.7×10^{-8}	yes	6	1.2×10^{-7}	no	0.76527496
10	8.7×10^{-8}	yes	5	1.37×10^{-7}	no	0.00028340182
10	8.7×10^{-8}	yes	1	3.12×10^{-7}	no	4.2×10^{-10}

Table 4.8:

Probabilities that Maps with Junctions come from same Distribution as Maps without Junctions for Strings with Gaussian
(Based on the distribution of edges)
$a = 0.976$ 26x26 Boxes Per window

N	$G\mu$	junctions	N	$G\mu$	junctions	probability
10	8.7×10^{-8}	yes	10	1×10^{-7}	no	0
10	8.7×10^{-8}	yes	6	1.2×10^{-7}	no	0
10	8.7×10^{-8}	yes	5	1.37×10^{-7}	no	4.1×10^{-8}
10	8.7×10^{-8}	yes	1	3.12×10^{-7}	no	0.00076553716

a large number of boxes with just a few edges, as would be expected, whereas $N = 10$ strings per Hubble volume looked more Gaussian, as expected. We found a statistical difference between the curves for junctions and the curves of different scaling solutions without junctions.

Future work includes optimizing the Canny algorithm, and searching for the lowest value of the string tension for which maps with and without string junctions can be differentiated. It would also be very interesting to algorithms to "real" string simulations (those obtained via a numerical evolution of the Nambu-Goto equations) rather than just relying on the simple toy models for the distribution of strings which we have used. Maps of CMB anisotropies produced by strings without junctions coming from "real" simulations are available [63]. However, to our knowledge there are no corresponding results for networks with string junctions.

4.7 Summary

In this chapter we furthered the analysis from the previous chapter and found a method to distinguish cosmic superstrings from generic cosmic strings in simulated CMB temperature position space maps. We also found that we could distinguish among scaling solutions of cosmic strings. In the next chapter we shall continue to explore signatures of cosmic strings in the CMB but, in this case, in the polarization window.

Chapter 5

A Signature of Cosmic String Wakes in the CMB Polarization

5.1 Preface

In this section we look for the position space polarization signal of cosmic strings in the CMB. We do this by considering the non-linear structures formed by overdensities of matter behind strings, their wakes. This builds upon the previous two chapters as temperature was the first signal found from the CMB and its polarization became the next observational window to probe. More and more experiments are being planned today to probe polarization, hence this window represents the present and future exciting area of CMB physics.

5.2 Introduction

In recent years there has been renewed interest in the possibility that cosmic strings contribute to the power spectrum of curvature fluctuations which give rise to the large scale structure and cosmic microwave background (CMB) anisotropies which we see today. One of the reasons is that many inflationary models constructed in the context of supergravity models lead to the formation of gauge theory cosmic strings at the end of the inflationary phase [83, 84]. Second, in a large class of brane inflation models the formation of cosmic superstrings [193] at the end of inflation is generic [157], and in some cases (see [47]) these strings are stable (see also [55, 156] for reviews on fundamental cosmic strings). Cosmic superstrings are also a possible remnant of an early Hagedorn phase of string gas cosmology [34, 121, 31, 26]

In models which admit stable strings or superstrings, a scaling solution of such strings inevitably [97, 96] results as a consequence of cosmological dynamics (see e.g. [187, 75, 28] for reviews on cosmic strings and structure formation). In a scaling solution, the network of strings looks statistically the same at any time t if lengths are scaled to the Hubble radius at that time. The distribution of strings is dominated by a network of "infinite" strings [1] with mean curvature radius and separation being of the order of the Hubble radius. The scaling solution of infinite strings is maintained by the production of string loops due to the interaction of long strings. This leads to a distribution of string loops with a well defined spectrum (see e.g. [180, 158, 171]) for all radii R smaller than a cutoff radius set by the Hubble length. Whereas the scaling distribution of the infinite strings is reasonably well known as a result of detailed numerical simulations of cosmic string evolution (see [4, 16, 5, 150, 183] for some references), there is still substantial uncertainty concerning the distribution of string loops. It is, however, quite clear that the long strings dominate the energy density of strings. The distinctive signals of strings which we will focus on are due to the long strings.

Cosmic strings give rise to distinctive signatures in both the CMB and in the large-scale structure. These signatures are a consequence of the specific geometry of space produced by strings. As studied initially in [185], space perpendicular to a long straight string is locally flat but globally looks like a cone whose tip coincides with the location of the string (the smoothing out of the cone as a consequence of the internal structure of the cosmic string was

[1] Any string with a mean curvature radius comparable or greater than the Hubble radius or which extends beyond the Hubble radius is called "infinite" or "long".

worked out in [67]). The deficit angle is given by

$$\alpha \, = \, 8\pi G\mu \, . \tag{5.1}$$

where μ is the string tension and G is Newton's constant. Hence, a cosmic string moving with velocity v in the plane perpendicular to its tangent vector will lead to line discontinuities in the CMB temperature of photons passing on different sides of the string. The magnitude of the temperature jump is [89]

$$\frac{\delta T}{T} \, = \, 8\pi\gamma(v)vG\mu \, , \tag{5.2}$$

where γ is the relativistic gamma factor associated with the velocity v.

As a consequence of the deficit angle (5.1), a moving string will generate a cosmic string wake, a wedge-shaped region behind the string (from the point of view of its velocity), a region with twice the background density [166] (see Figure 5.2). Causality (see e.g. [177, 178]) limits the depth of the distortion of space due to a cosmic string. The details were worked out in [112] where it was shown that the deficit angle goes to zero quite rapidly a distance t from the string. Hence, the depth of the string wake is given by the same length. String wakes lead to distinctive signatures in the topology of the large-scale structure, signatures which were explored e.g. in [117, 30].

Wakes formed at arbitrarily early times are non-linear density perturbations. For wakes formed by strings present at times $t_i > t_{rec}$, where t_{rec} is the time of recombination, the baryonic matter inside the wake undergoes shocks [147] (see e.g. [168] for a detailed study). The shocks, in turn, can ionize the gas - although as it turns out the residual ionization from decoupling is larger. Photons passing through these ionized regions on their way from the last scattering surface to the observer can thus be polarized - and it is this polarization signature which we aim to study here.

The tightest constraints on the contribution of scaling strings to structure formation (and thus the tightest upper bound on the tension μ of the strings) comes from the analysis of the angular power spectrum of CMB anisotropies.

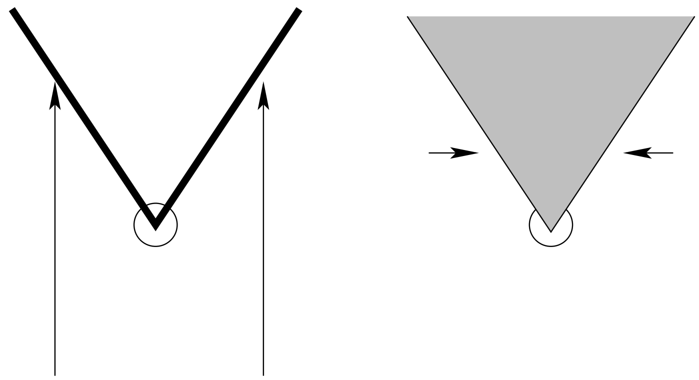

Figure 5.1: Sketch of the mechanism by which a wake behind a moving string is generated. Consider a string perpendicular to the plane of the graph moving straight downward. From the point of view of the frame in which the string is at rest, matter is moving upwards, as indicated with the arrows in the left panel. From the point of view of an observer sitting behind the string (relative to the string motion) matter flowing past the string receives a velocity kick towards the plane determined by the direction of the string and the velocity vector (right panel). This velocity kick towards the plane leads to a wedge-shaped region behind the string with twice the background density (the shaded region in the right panel).

As discussed in [135, 111, 130], the angular power spectrum does not have the acoustic ringing which inflation-seeded perturbations generate. The reason is that the string network is continuously seeding the growing mode of the curvature fluctuation variable on super-Hubble scales. Hence, the fluctuations are “incoherent” and “active” as opposed to “coherent” and “passive” as in the case of inflation-generated fluctuations. The contribution of cosmic strings to the primordial power spectrum of cosmological perturbations is thus bounded from above, thus leading to an upper bound [138, 195, 62, 164, 18, 19, 8, 9] on the string tension of between $G\mu < 3 \times 10^{-7}$ [138, 195] and $G\mu < 7 \times 10^{-7}$ [18, 19]. The analysis of [138, 195] is based on a toy model for the scaling distribution of strings whereas [18, 19] is based on numerical field theory simulations.

Past work on CMB temperature maps has shown that signatures of cosmic strings are easier to identify in position space than in Fourier space [89, 118, 108, 86, 87] and recent studies show that high angular resolution surveys such as the South Pole Telescope project [151] have the potential of improving the limits on the string tension by an order of magnitude [6, 173, 52, 53] (although it must be mentioned that these analyses are based on a toy model distribution of cosmic strings which does not contain some features which emerge from numerical string network simulations [63] and which may render the sharp position space features harder to detect).

To date there has been little work on CMB polarization due to strings. Most of the existing work focuses on the angular power spectra of the polarization. Based on a formalism [130] (see also [2]) to include cosmic defects as source terms in the Boltzmann equations used in CMB codes, the power spectra of temperature and temperature polarization maps were worked out [162] in the case of models with global defects such as global cosmic strings. Since in cosmic defect models vector and tensor modes are as important as the scalar metric fluctuations [130, 61], a significant B-mode polarization is induced. In fact, in the case of global strings with a tension close to the upper bound mentioned above, whereas the amplitude of the temperature and E-mode polarization power spectra are so small as to make the string signal invisible compared to the signal from the scale-invariant spectrum of adiabatic fluctuations (e.g. produced in inflation), the contribution of strings dominates the amplitude of the B-mode polarization power spectrum. In the case of local strings, these conclusions were confirmed in the more recent analyses of [138, 195, 163, 8, 9, 18, 19, 139, 140]. The maximal amplitude of the B-mode polarization power spectrum for strings with $G\mu = 3 \times 10^{-7}$ was shown to be taken on at angular harmonic values of $l \sim 500$ and to be of the order $0.3 \mu K^2$ [139, 140]. However, the analyses of [138, 195, 163, 8, 9, 18, 19, 139, 140] do not take into account the effects of the gravitational accretion onto cosmic string wakes. In related work, the conversion of E-mode to B-mode polarization via the gravitational lensing induced by cosmic strings was studied in [11] [2] .

Similarly to what was found in the analysis of CMB temperature maps from cosmic strings, we expect that a position-space analysis will be more powerful at revealing the key non-Gaussian signatures of strings in CMB polarization. Hence, in this work we derive the position space signature of a cosmic string wake in CMB polarization maps.

In the following section we briefly review cosmic string wakes. In Section 5.4 we then analyze the polarization signature of wakes, and we conclude with some discussion.

5.3 Cosmic String Wakes

Since the strings are relativistic, they generally move with a velocity of the order of the speed of light. There will be frequent intersections of strings. The long strings will chop off loops, and this leads to the conclusion that the string distribution will be statistically independent on time scales larger than the Hubble radius [3] .

[2] While this paper was being finalized for submission, a preprint appeared [66] computing the local B-mode polarization power spectrum from cosmic strings.

[3] Hence, to model the effects of strings we will make use of a toy model introduced in [133, 134] and used in most analytical work on cosmic strings and structure formation since then: we divide the time interval between recombination and the current time t_0 into Hubble expansion time steps. In each time step, we will approximate the infinite strings by a collection of finite straight string segments whose length is given by the curvature radius of the string network. On a Hubble time scale, the infinite strings will self-intersect. Hence, we take the distribution of string segments to be statistically independent on a Hubble time scale. Hence, in each time step there is a distribution of straight string segments moving in randomly chosen directions with velocities chosen at random between 0 and 1 (in units of the speed of light). The centers and directions of these string segments are random, and the string density corresponds to N strings per Hubble volume, where N is an integer which is

In this work, we place one string of length $c_1 t_i$ [4] at a specified time t_i and assume it is moving in transverse direction with a velocity v_s. This string segment will generate a wake, and it is the signal of one of these wakes in the CMB polarization which we will study in the following.

A string segment laid down at time t_i. will generate a wake whose dimensions at that time are the following:

$$c_1 t_i \times t_i v_s \gamma_s \times 4\pi G\mu t_i v_s \gamma_s \,, \tag{5.3}$$

In the above, the first dimension is the length in direction of the string, the second is the depth which depends on v_s (γ_s is the associated relativistic γ factor) , and the third is the average thickness. The geometry of a cosmic string wake is illustrated in Figure 5.2.

Once the wake is formed, its planar dimensions will expand as the universe grows in size, and the thickness (defined as the region of non-linear density) will grow by gravitational accretion. The accretion of matter onto a cosmic string wake was studied in [172, 32] in the case of the dark matter being cold, and in [32, 136] in the case of the dark matter being hot [5] We are interested in the case of cold dark matter.

---

of the order 1 according to the scaling of the string network. The distribution of string segments is uncorrelated at different Hubble times.

[4] The constant c_1 is of the order 1 and depends on the correlation length of the string network as a function of the Hubble radius and must be determined from numerical simulations of cosmic string evolution.

[5] If the strings have lots of small-scale structure then they will have an effective tension which is less than the effective energy density [41, 189]. This will lead to a local gravitational attraction of matter towards the string, a smaller transverse velocity, and hence to string filaments instead of wakes. The gravitational accretion onto string filaments was studied in [1].

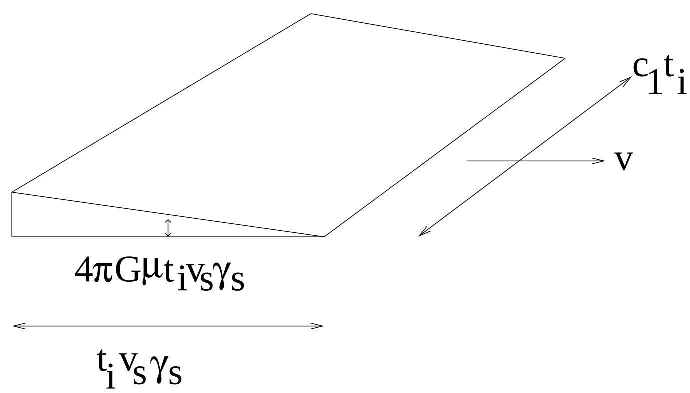

Figure 5.2: Sketch of the geometry of a cosmic string wake. The wake is the wedge-shaped region shown. The string is moving in horizontal direction towards the right, and is located along the line where the wake has vanishing thickness. The horizontal dimension of the wake is determined by the string velocity and the Hubble time when the wake is created (time t_i). The size of the wake in direction of the string is set by the curvature radius of the cosmic string network and is in our toy model taken to be the Hubble scale. The thickness of the wake perpendicular to the plane spanned by the tangent vector of the string and the string velocity vector changes as we move away from the tip of the string. The average wake thickness is indicated by the short vertical line with arrow signs in both directions.

We consider mass planes at a fixed initial comoving distance q above the center of the wake. The corresponding physical height is

$$h(q,t) \;=\; a(t)\big[q - \psi(q,t)\big]\,, \tag{5.4}$$

where $\psi(q,t)$ is the comoving displacement induced by the gravitational accretion onto the wake. For cold dark matter, the initial conditions for $\psi(q)$ are $\psi(q,t_i) = \dot{\psi(q},t_i) = 0$. The goal of the analysis is to find the thickness of the wake at all times $t > t_i$. The thickness is defined as the physical height h above the center of the wake of the matter shell which is beginning to fall towards the wake, i.e. for which $\dot{h(q},t) = 0$. In the Zel'dovich approximation, we first consider the equation of motion for h obtained by treating the source (the initial surface density σ of the wake) in the Newtonian limit, i.e.

$$\ddot{h} \;=\; -\frac{\partial\Phi}{\partial h}\,, \tag{5.5}$$

where Φ is the Newtonian gravitational potential given by the Poisson equation

$$\frac{\partial^2\Phi}{\partial^2 h} \;=\; 4\pi G\big[\rho + \sigma\delta(h)\big] \tag{5.6}$$

($\rho(t)$ being the background energy density), and then by linearizing the resulting equation in ψ. The mean surface density is

$$\sigma(t) \;=\; 4\pi G\mu t_i v_s \gamma_s \Big(\frac{t}{t_i}\Big)^{2/3}\rho(t)\,. \tag{5.7}$$

The result of the computation of the value of the comoving displacement q_{nl} which is "turning around" at the time t for a wake laid down at time t_i is [32]

$$q_{nl}(t,t_i) \;=\; \psi_0\Big(\frac{t}{t_i}\Big)^{2/3} \tag{5.8}$$

with

$$\psi_0(t_i) \;=\; \frac{24\pi}{5} G\mu v_s \gamma_s (z(t_i)+1)^{-1/2} t_0\,. \tag{5.9}$$

This corresponds to a physical height of

$$
\begin{aligned}
h(t,t_i) &= a(t)\big[q_{nl}(t,t_i) - \psi(q_{nl},t)\big] \simeq a(t)q_{nl}(t,t_i) \\
&= \psi_0 \frac{z_i+1}{(z+1)^2}\,,
\end{aligned}
\tag{5.10}
$$

where z_i and z are the redshifts corresponding to the times t_i and t, respectively. These formulae agree with what is expected from linear cosmological perturbation theory: the fractional density perturbation should increase linearly in the scale factor which means that the comoving width of the wake must grow linearly with $a(t)$.[6] It should be emphasized that the above result (5.10) assumes a wake created by an idealized straight string segment.

Let us return to the geometry of the string segment. The tangent vector to the string and the direction of motion of the string determine a surface in space (the "string plane"). If neither the string tangent vector nor the velocity vector have a radial component (radial with respect to the co-moving point of our observer), then the photons will cross each point of the string wake at the same time, and the wake will correspond to a rectangle in the sky whose planar dimensions are

$$
c_1 t_1 \times t_i v_s \gamma_s\,. \tag{5.11}
$$

However, if the normal vector of the string plane is not radial, then one of the planar dimensions will be reduced by a trigonometric factor $\cos(\theta)$ depending on the angle θ between the normal vector and the radial vector. In addition, photons which we detect today did not pass the wake at the same time. This will lead to a gradient of the polarization signal across the projection of the wake onto the CMB sky. To simplify the analysis, in the following we will assume that θ is small.

---

[6] This formula agrees within a factor of two with the numerical studies of [168].

In the following section we will need the expression for the number density $n_e(t, t_i)$ of free electrons at time t in a wake which was laid down at the time t_i. The initial number density is

$$n_e(t_i, t_i) \simeq f \rho_B(t_i) m_p^{-1} , \tag{5.12}$$

where f is the ionization fraction, ρ_B is the energy density in baryons, and m_p is the proton mass. Taking into account that for $t > t_i$ the number density redshifts as the inverse volume we get

$$n_e(t, t_i) \simeq f \rho_B(t_i) m_p^{-1} \Big(\frac{z(t) + 1}{z(t_i) + 1} \Big)^3 . \tag{5.13}$$

5.4 Analysis

If unpolarized cosmic microwave background radiation with a quadrupolar anisotropy scatters off free electrons, then the scattered radiation is polarized (see e.g. [79, 59] for reviews of the theory of CMB polarization). The magnitude of the polarization depends on the Thomson cross section σ_T and on the integral of the number density of electrons along the null geodesic of radiation. Our starting formula is

$$P(\mathbf{n}) \simeq \frac{1}{10} \Big(\frac{3}{4\pi} \Big)^{1/2} \tau_T Q , \tag{5.14}$$

where $P(\mathbf{n})$ is the magnitude of polarization of radiation from the direction $\mathbf{n}$, Q is the temperature quadrupole, and

$$\tau_T = \sigma_T \int n_e(\chi) d\chi , \tag{5.15}$$

where the integral is along the null geodesic in terms of conformal time.

Let us now estimate the contribution to the polarization amplitude from CMB radiation passing through a single wake at time t, assuming that the wake was laid down at the time t_i and has thus had time to grow from time t_i to the time t when the photons are crossing it. We assume that the photons cross in perpendicular direction. Since the wake is thin, we can estimate the integral in Eq. (5.15) by

$$\tau_T \sim 2\sigma_T n_e(t,t_i)\big(z(t)+1\big)h(t,t_i) \qquad (5.16)$$

where the factor 2 is due to the fact that the width of the wake is twice the height, and the redshift factor comes from the Jacobean transformation between χ and position. Inserting Eq. (5.16) into the expression (5.14) for the polarization amplitude and using the value for the height and the number density of electrons obtained in the previous section we find

$$\begin{aligned}\frac{P}{Q} &\simeq \frac{1}{5}\big(\frac{3}{4\pi}\big)^{1/2}\sigma_T f\rho_B(t_i)m_p^{-1} \\ &\quad\times\frac{(z(t)+1)^2}{(z(t_i)+1)^2}\psi_0(t_i)\,. \qquad (5.17)\end{aligned}$$

Inserting the formula for $\psi_0(t_i)$ from Eq. (5.9), expressing the baryon density at t_i in terms of the current baryon density, and the latter in terms of the baryon fraction Ω_B and the total energy density ρ_c at the current time t_0, we obtain

$$\begin{aligned}\frac{P}{Q} &\simeq \frac{24\pi}{25}\big(\frac{3}{4\pi}\big)^{1/2}\sigma_T fG\mu v_s\gamma_s \\ &\quad\times\Omega_B\rho_c(t_0)m_p^{-1}t_0\big(z(t)+1\big)^2\big(z(t_i)+1\big)^{1/2}\,. \qquad (5.18)\end{aligned}$$

From Equation (5.18) we see that the polarization signal is larger for wakes laid down early, i.e. close to the time of recombination. For fixed t_i, the signal is largest for configurations where the photons we observe today cross the wake at the earliest possible time, i.e. for the largest $z(t)$ (obviously, t is constrained to be larger than t_i, otherwise our formula for the height is not applicable). To get an order of magnitude estimate of the magnitude of the polarization signal, we take $z(t_i) \sim z(t) \sim 10^3$. Inserting the value of the Thomson cross section, the proton mass and the current time we get

$$\frac{P}{Q} \sim fG\mu v_s\gamma_s\Omega_B\big(\frac{z(t)+1}{10^3}\big)^2\big(\frac{z(t_i)+1}{10^3}\big)^3 10^7\,. \qquad (5.19)$$

The ionization fraction of baryonic matter drops off after recombination, but it does not go to zero. As already discussed in [124, 127] there is remnant residual ionization of the matter. As computed in [127] (see also [91]), the residual ionization fraction f tends to a limiting value of between 10^{-5} and 10^{-4} at late times after recombination.

Shocks inside the wake will lead to extra ionization. However, the resulting contribution to the ionization fraction is negligible for the range of string tensions we are interested in. To see this, we follow the analysis of [147]. A particle streaming towards a cosmic string wake has velocity

$$v_i = 4\pi G\mu v_s \gamma_s \tag{5.20}$$

and kinetic energy $\frac{1}{2}mv_i^2$. The particles will undergo shocks and thermalize. Equating the initial kinetic energy density with the final thermal energy density (assuming that the particles are distributed according to an approximate ideal gas law) yields a temperature inside the wakes of

$$T \simeq 7 \times 10^3 \left(\frac{G\mu}{2 \times 10^{-6}}\right)^2 (v_s \gamma_s)^2 \, K \, . \tag{5.21}$$

We then compute the Boltzmann factor to determine the ratio of ionized Hydrogen to ground state Hydrogen which is the ionization fraction. For string tensions of order 10^{-6} this results in ionization fractions of the order 10^{-9} which is considerably less than the residual ionization. For more realistic string tensions compatible with current bounds, 10^{-7}, the ionization fraction due to shocks is negligible compared to the residual ionization fraction. At the temperatures considered for a string tension of 10^{-7} at lower redshifts there would be star formation and hence an ionization fraction due to that effect since the wake would contain molecular hydrogen and satisfy the appropriate conditions. However, this is not an issue at redshifts under consideration.

Note that even though the extra ionization inside the wake is negligible compared to the overall ionization level, the wake is a locus of extra energy density. Thus, even if the ionization fraction is homogeneous in space, the inhomogeneous distribution of matter will lead to a specific polarization signature.

The position space signal of the polarization produced by a wake will be very specific: for a wake whose normal vector is in radial direction, it will be a rectangle in the sky with angular dimensions corresponding to the comoving size

$$c_1 t_i \big(z(t_i) + 1\big) \times v_s \gamma_s t_i \big(z(t_i) + 1\big) \tag{5.22}$$

(see Eq. (5.3)). If the angle of the normal of the string plane to the radial normal vector is $\theta \neq 0$, then one of the planar dimensions is reduced by a factor of $\cos(\theta)$. However, the light travel time through the wake is increased by a factor of $[\cos(\theta)]^{-1}$. Thus, the wake becomes a bit smaller but the signal strength increases. The average amplitude of the polarization is given by Eq. (5.18) - a value obtained using the average thickness of the wake. However, since the thickness of the wake increases linearly in direction of the string motion, the amplitude of the polarization signal will also increase linearly in this direction. A second source for the linear increase in the amplitude is the fact that $z(t_i)$ is increasing as we go away from the tip of the cone (by an amount corresponding to one Hubble expansion time when comparing the tip of the cone to the end). The direction of the polarization vector depends on the relative orientation between the string and the CMB quadrupole. In Figure 5.3 we give a sketch of the signal. The amplitude of the polarization is proportional to the length of the arrow, the direction of the polarization is given by the direction of the arrow. Since the direction of the variation of the polarization strength is determined by the string and is therefore uncorrelated with the direction of the CMB quadrupole, on the average the E-mode and B-mode strengths of the polarization signal will be the same.

Let us now discuss the magnitude of our effect. We will consider the value $G\mu = 3 \times 10^{-7}$ which is the current upper bound on the string tension [138, 195] (using the assumptions about the cosmic string scaling solution made in these papers). Wakes produced close to the time of recombination

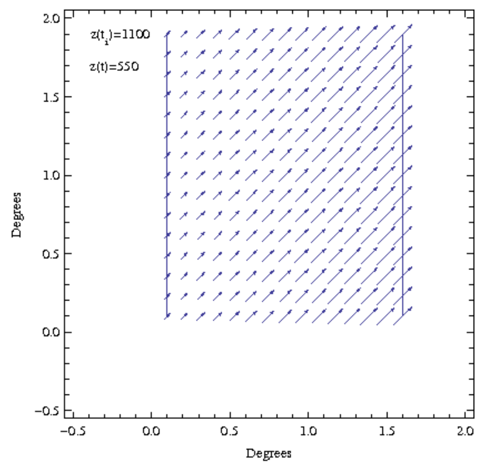

Figure 5.3: The polarization signal of a single wake which is taken to be perpendicular to the line of sight between us and the center of the string segment. The tip of the wake (position of the string at the time the wake is laid down) is the vertical edge of the rectangle, and the string velocity vector is pointing horizontally to the left. The length and direction of the arrows indicate the magnitude and orientation of the polarization vector. We have assumed that the variation of the quadrupole vector across the plane of the wake is negligible. Note that the angle between the velocity vector of the string and the CMB quadrupole is random. We have assumed that the quadrupole vector is at an angle relative to the plane of the wake. This determines the direction of the polarization vector we have drawn. The orientation we have chosen in this figure corresponds to an almost pure B-mode.

inherit the ionization fraction of the universe at that time. Taking a value of $f = 10^{-3}$ (which is smaller than the ionization fraction until redshift $z \simeq 600$ [91]), we obtain a polarization amplitude of $P \sim 10^{-2}\ \mu$K which is larger than the background in the B-mode polarization arising from weak lensing of the primordial perturbations [76, 78] for l-values of about 100.

It is instructive to compare our polarization signal from a cosmic string wake with the expected noise due to the Gaussian fluctuations. In Fig. 5.4 we have superimposed the map of the Q-mode polarization from a cosmic string wake laid down during the first Hubble time after recombination with a corresponding Q-mode map due to Gaussian noise of the concordance ΛCDM model. The string parameters are the same as mentioned in the previous paragraph. We chose the orientation of the string relative to the CMB quadrupole such that the power in the Q-mode is half the total power. As the value of the CMB quadrupole we used 30μK. To render the string signal visible in the Q-mode map (in which the noise is much larger than in a B-mode map) we multiplied the string signal by 100. In this case the string signal is clearly visible be eye. The brightest edge (the vertical edge on the right side) corresponds to the position of the string when it begins to generate the wake, not at the position at the end of the time interval being considered (the vertical edge on the left). Note the difference compared to the Kaiser-Stebbins effect in the CMB temperature maps: in this case the brightest edge corresponds to the location of the string when the photons are passing by it.

Without boosting the string signal by a large factor, it would not be visible by eye. However, the distinctive lines in the map can be searched for by edge detection algorithms such as the Canny algorithm which was used to study the string signal in CMB temperature maps. In the studies of [52, 53] it was found that the cosmic string lines in temperature maps can be picked out if the string signal accounts for less than 0.2% of the power. Thus, it should be able to easily pick out the string signal in the Q-mode polarization maps. In B-mode polarization maps the string signal would be much easier to detect.

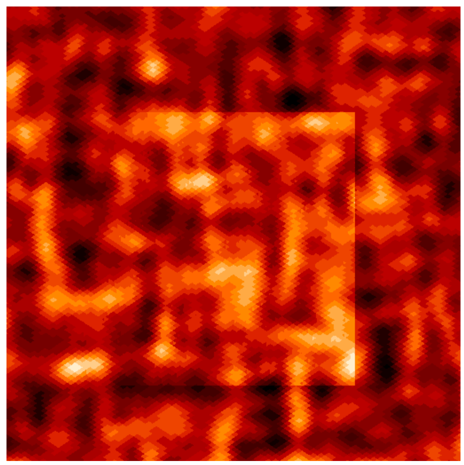

Figure 5.4: The Q-mode polarization signal of a single wake which is taken to be perpendicular to the line of sight between us and the center of the string segment, superimposed on the Gaussian noise signal which is expected to dominate the total power spectrum. The string signal is multiplied by a factor of 100 to render it visible by eye. The tip of the wake (position of the string at the time the wake is laid down) is the vertical bright edge of the right side, and the string velocity vector is pointing horizontally to the left. At the final string position the wake thickness vanishes and there is no polarization discontinuity line. We have assumed that the variation of the quadrupole vector across the plane of the wake is negligible and that the quadrupole vector is at an angle relative to the plane of the wake such that the Q-mode picks up half of the polarization power.

5.5 Conclusions and Discussion

In this Letter we have discussed a position space signal of a cosmic string wake in CMB polarization maps. In the same way that the line discontinuities in the CMB temperature maps predicted by the Kaiser-Stebbins (KS) effect yield a promising way to constrain/detect cosmic strings in the CMB (see e.g. [118, 108, 86, 87, 6, 173, 52, 53], we believe that the signal discussed in this paper will play a similar role once CMB polarization maps become available.

We have shown that a single wake will produce a rectangular patch in the sky of dimensions given by equation (5.22), average magnitude given by equation (5.18) and amplitude increasing linearly in one direction across the patch. For a value of the string tension $G\mu = 3 \times 10^{-7}$ (the current upper limit), the amplitude of the signal is within the range of planned polarization experiments for wakes produced sufficiently close to the surface of recombination. These wakes are also the most numerous ones. The brightest edge in the polarization map corresponds to the beginning location of the string, not the final location. Since the KS discontinuity in the CMB temperature map will occur along the line corresponding to the final position, the polarization signal discussed here provides a cross-check on a possible string interpretation of a KS signal.

A scaling distribution of strings will yield a distribution of patches in the sky, the most numerous ones and the ones with the largest polarization amplitude being set by wakes laid down at times close to the time of recombination which are crossed by the CMB photons at similarly early times.

5.6 Summary

In this section we continued our exploration of the CMB by examining the signature of cosmic strings in the polarization probe. We found that cosmic string wakes leave distinct imprints on simulated polarization data that could conceivably be detected with a method such as the Canny algorithm developed in the first chapter. In the next chapter we shall continue our analysis of cosmic string traces in observational windows, exploring the emerging window of the redshifted 21 cm spectrum.

Chapter 6

The 21 cm Signature of Cosmic String Wakes

6.1 Preface

If CMB temperature maps represent the past and present window of cosmology, and the polarization of the CMB is the present and future window, then the probe of 21 cm is certainly the future window of cosmology. In this section we examine the signature of cosmic strings on the 21 cm redshifted spectrum. Again, the overdense regions behind cosmic strings, wakes, provide the extra density of hydrogen in which the spin-flip could potentially be observed.

6.2 Introduction

Cosmic strings (see [198, 184, 97, 96, 180, 158, 171] for initial work on cosmic strings and structure formation) cannot be [111, 130] the dominant source of the primordial fluctuations, however they can still provide a secondary source of fluctuations. Over the past decade, the realization has grown that many inflationary scenarios constructed in the context of supergravity models lead to the formation of gauge theory cosmic strings at the end of the inflationary phase [83, 84]. Also, in a large class of brane inflation models the formation of cosmic superstrings [193] at the end of inflation is generic [157], and in some cases (see [47]) these strings are stable (see also [55, 156] for reviews on fundamental cosmic strings). Cosmic superstrings are also a possible remnant of an early Hagedorn phase of string gas cosmology [34, 121, 31, 26]. In all of these contexts, both a scale-invariant spectrum of adiabatic coherent perturbations and a sub-dominant contribution of cosmic strings is predicted. Hence, it is important to search for the existence of cosmic strings.

In this paper we study the signature of cosmic strings in 21 cm radiation maps (see e.g. [65] for an in-depth review of 21 cm cosmology). Observing the intensity of the cosmological background radiation at wavelengths corresponding to the red-shifted 21 cm transition line of neutral hydrogen has several potential advantages compared to the currently explored windows . First of all, it probes the distribution of the dominant form of baryonic matter and is thus not sensitive to our incomplete understanding of star formation and non-linear evolution, which is a problem when interpreting the results of optical redshift surveys. Secondly, it probes the universe at higher redshifts and allows us to explore the “dark ages” (the epoch before star formation and non-linear clustering set in). Related to this, it explores the distribution of matter in a regime when the amplitude of the fluctuations is smaller and linear theory is a better approximation. Finally, 21 cm surveys provide three-dimensional maps, a significant potential advantage over CMB anisotropy maps.

Cosmic strings are known to give rise to distinctive signatures in CMB temperature anisotropy maps [89], CMB polarization maps [54] and large-scale structure (LSS) maps [166, 147, 182, 172, 43, 72, 71]. These distinctive signatures come from moving long (compared to the Hubble radius) strings (see Section 2). In the CMB temperature maps, these strings lead to line discontinuities, in the polarization maps to (roughly) rectangular regions with extra polarization, and in LSS maps to thin planar regions of enhanced density. These signals are manifest in position space maps, but they become obscured when calculating power spectra. Hence, the lesson is to study the maps in position versus momentum space.

Here, we compute the signature of a single cosmic string wake in 21 cm emission. We find that strings with tensions μ somewhat below the current limits of $G\mu = 3 \times 10^{-7}$ could be detected in 21 cm maps where they would appear as wedges in 21 cm maps with either extra emission or extra absorption, depending on the tension and on the specific redshift. The planar dimensions are set by the direction of the string and its velocity vector, and the width of the wedges is proportional to the string tension. This signal must be searched for in position space maps. In Fourier space the distinctive phase information would be washed out.

The outline of this paper is as follows: In Section 6.3 we discuss how string wakes are generated and how these lead to distinctive signals for observations. We review gravitational accretion of matter onto cosmic string wakes and compute the temperature of the HI gas inside the wake. In Section 6.4 we then study the 21 cm emission signal from a single cosmic string wake. The generalization to the case of a network of string wakes will be addressed in a future publication. We compute the brightness temperature and describe the geometrical structure of the signal, a structure very characteristic for cosmic strings. In the final section we summarize our results and put them in the context of other work on the possible detection of cosmic strings. When computing the magnitude of the 21 cm signal, we use the same WMAP concordance values [170] for the cosmological parameters as used in the review [65].

6.3 Cosmic Strings and Large-Scale Structure

In many field theory models, the formation of a network of cosmic strings is an inevitable consequence of a phase transition in the early universe (for reviews on cosmic strings see e.g. [97, 95, 187, 75, 28]). This network of cosmic strings approaches a "scaling solution" which means that the statistical properties of the string network are the same at all times if distances are scaled to the Hubble radius [28]. The detailed form of the scaling solution must be obtained from numerical simulations [4, 16, 5, 150, 183] of the evolution of a network of cosmic strings (see also [144] for some recent analytical work).

There are two components of the string network - firstly a network of "long" strings with a mean curvature radius $\zeta = c_1 t$, where c_1 is a constant of order unity, and secondly a distribution of string loops with radii smaller than the horizon which results from the "cutting up" of the long string network as a consequence of string intersections. According to more recent cosmic string evolution simulations, the long string component is more important for cosmological structure formation.

Numerical simulations by different groups have clearly verified the scaling solution for the long string network. There is, however, still a large uncertainty concerning the distribution of string loops (the only agreement seems to be that the loops are less important than the long strings for cosmological structure formation). Hence, in order to obtain constraints in models with cosmic strings which are robust against the uncertainties in the numerical simulations, it is important to focus on signatures of long strings as opposed to signatures of string loops. The tightest current constraints on cosmic strings come from the shape of the angular power spectrum of CMB anisotropies, yielding a constraint of [138, 195] (see also [62, 164, 8, 9])

$$G\mu \, < \, 3 \times 10^{-7} \, , \tag{6.1}$$

where μ is the string tension and G is Newton's constant. However, it is important to keep in mind that this limit is based on an analytical description of the scaling solution which contains a number of parameters which can only be determined from comparisons with numerical simulations and whose values thus have a substantial uncertainty. Work based on a field theory simulation of strings [18, 19] gives a limit of twice the above value (see also [7] for a very recent analysis of the different bounds). Note that limits on the cosmic string tension which come from gravitational radiation from string loops [50, 51] are sensitive both to the large uncertainties in the distribution of string loops, and also to back-reaction effects on cosmic string loops (see e.g. [27]), and are hence not robust.

Direct limits on the cosmic string tension μ can be obtained by looking for specific signatures of individual long strings. These are limits which are insensitive to the parameters in the cosmic string scaling solution. Limits obtained from searching for the Kaiser-Stebbins signature of a long string in CMB temperature maps were derived in [108, 86, 87] using WMAP data. The limits obtained were weaker than the ones from (6.1). However, the angular scale of the WMAP experiment is too large to be able to effectively search for sharp features in position space maps such as those predicted by cosmic strings. It was pointed out [63] that the string signatures for values of $G\mu$ somewhat smaller than the limiting value of (6.1) should be clearly visible in smaller angular scale CMB anisotropy maps such as those provided by the ACT [102] and SPT [151] experiments. In recent work [6, 173, 52, 53] it was shown that limits up to an order of magnitude tighter than (6.1) might be achievable using SPT data. In the following, we will discuss direct signals of wakes created by long strings in 21 cm surveys.

As first pointed out in [166] and then further discussed in [182, 147, 147, 172, 43], long strings moving perpendicular to the tangent vector along the string give rise to "wakes" behind the string, i.e. in the plane spanned by the tangent vector to the string and the velocity vector. The wake arises as a consequence of the geometry of space behind a long straight string [185, 67] - space perpendicular to the string is conical with a deficit angle given by

$$\alpha \,=\, 8\pi G\mu \,. \tag{6.2}$$

From the point of view of an observer behind the string (relative to the string velocity vector), it appears that matter streaming by the string (from the point of view of the observer travelling with the string) obtains a velocity kick of magnitude

$$\delta v \,=\, 4\pi G\mu v_s\gamma_s \,\sim\, 4\text{km/s}(G\mu)_6 v_s\gamma_s \tag{6.3}$$

towards the plane behind the string. In the above, v_s is the velocity of the string (in units of the speed of light), γ_s is the corresponding relativistic gamma factor, and $(G\mu)_6$ is the value of $G\mu$ in units of 10^{-6}. This leads to a wedge-shaped region behind the string with twice the background density (see Figure 6.3).

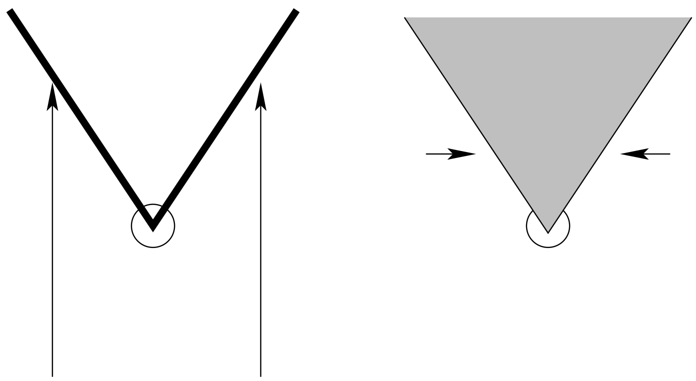

Figure 6.1: Sketch of the mechanism by which a wake behind a moving string is generated. Consider a string perpendicular to the plane of the graph moving straight downward. From the point of view of the frame in which the string is at rest, matter is moving upwards, as indicated with the arrows in the left panel. From the point of view of an observer sitting behind the string (relative to the string motion) matter flowing past the string receives a velocity kick towards the plane determined by the direction of the string and the velocity vector (right panel). This velocity kick towards the plane leads to a wedge-shaped region behind the string with twice the background density (the shaded region in the right panel).

Since the strings are relativistic, they generally move with a velocity of the order of the speed of light. There will be frequent intersections of strings. The long strings will chop off loops, and this leads to the conclusion that the string distribution will be statistically independent on time scales larger than the Hubble radius. Hence, to model the effects of strings we will make use of a toy model introduced in [133, 134] and used in most analytical work on cosmic strings and structure formation since then: we divide the time interval between the time of equal matter and radiation and the current time t_0 into Hubble expansion time steps. In each time step, we lay down a distribution of straight string segments moving in randomly chosen directions with velocities chosen at random between 0 and 1 (in units of the speed of light). The centers and directions of these string segments are also chosen randomly, and the string density corresponds to N strings per Hubble volume, where N is an integer which is of the order 1 according to the scaling of the string network. The distribution of string segments is uncorrelated at different Hubble times. Each string segment will generate a wake, and it is the signal of one of these wakes which we will study in the following.

A string segment laid down at time t_i will generate a wake whose dimensions at that time are the following:

$$c_1 t_i \times t_i v_s \gamma_s \times 4\pi G\mu t_i v_s \gamma_s \,, \tag{6.4}$$

where c_1 is a constant of order one. In the above, the first dimension is the length in direction of the string, the second is the depth. The fact that the string wake has a finite depth is due to the causality constraints on density fluctuations produced during a phase transition [177, 178]: The information about the formation of a string (and hence the information about the existence of a deficit angle) cannot have propagated farther than the horizon from the point of nucleation of the defect. It was shown in [112] that the deficit angle quite rapidly tends to zero as the horizon is approached.

The overdense region in the wake will lead to the gravitational accretion of matter above and below the wake towards the center of the wake. In this way, the wake will grow in thickness. The accretion of matter onto a cosmic string wake was studied in [172, 32] in the case of the dark matter being cold, and in [32, 136] in the case of the dark matter being hot. We are interested in the case of cold dark matter. As an aside, we mention that if the strings have lots of small-scale structure then they will have an effective tension which is less than the effective energy density [41, 189]. This will lead to a local gravitational attraction of matter towards the string, a smaller transverse velocity, and hence to string filaments instead of wakes. The gravitational accretion onto string filaments was studied in [1].

We will now review the computation of the width of the wake. We are interested in the distribution of baryons in the vicinity of the string. However, for $t > t_{rec}$ the baryons and cold dark matter feel the same gravitational attraction and will thus behave in the same way - modulo thermal velocity effects which will be discussed later - until the baryons undergo a shock. Thus, for the moment we focus on the onset of clustering of the cold dark matter. We are interested in wakes created after the time t_{eq} of equal matter and radiation (there is no gravitational clustering of cold dark matter before that time). For times between t_{eq} and recombination (t_{rec}), the baryons are coupled to the radiation. However, for $t > t_{rec}$ the baryons will rapidly fall into the potential wells created by the cold dark matter and thus, once again, it is legitimate to focus attention on the clustering of the cold dark matter. Note that wakes produced at the earliest time are the most numerous.

We consider a mass shell located at a comoving distance q above the wake. Its physical distance above the wake at time t is

$$h(q,t) \, = \, a(t)\big(q-\psi\big) \, , \tag{6.5}$$

where ψ is the comoving perturbation induced by gravitational accretion. If the wake is laid down at the initial time t_i (with corresponding redshift z_i), then the initial conditions for the cold dark matter fluctuation are

$$\psi(t_i) \, = \, \dot{\psi}(t_i) \, = \, 0 \, . \tag{6.6}$$

As a consequence of the initial wake planar overdensity $\sigma(t_i)$, the comoving displacement ψ will begin to increase. The clustering dynamics can be studied making use of the Zel'dovich approximation [197] in which the gravitational force is treated in the Newtonian limit. As reviewed recently in [54], we obtain

$$\psi(t) \, = \, \frac{18\pi G}{5}\sigma(t_i)\big(\frac{t_i}{t_0}\big)^{2/3}\big(\frac{t}{t_0}\big)^{2/3}t_0^2 \, , \tag{6.7}$$

where t_0 is the present time and $\sigma(t_i)$ is the initial wake planar density excess.

The mass shell with initial comoving distance q above the wake "turns around" when $\dot{h}(q,t) = 0$. At time t, this occurs for a value $q = q_{nl}(t)$ given by

$$q_{nl}(t) \ = \ \frac{24\pi}{5} G\mu v_s \gamma_s (z_i+1)^{-1/2} t_0 \bigl(\frac{t}{t_i}\bigr)^{2/3} . \tag{6.8}$$

It is easy to check that at the point of turnaround

$$\psi(q_{nl}, t) \ = \ \frac{1}{2} q \, , \tag{6.9}$$

and that hence the density inside the turnaround surface is twice the background density.

Once a matter shell reaches its maximal distance h_{max} from the center of the wake, it will start to collapse onto the wake. The infall of matter will halt as the shell hits other streams of matter. This will lead to a shock. In analogy with what can be shown analytically in the context of the spherical collapse model (see e.g. [128]) we assume that the shock occurs at approximately half the maximal distance. The hydrodynamical simulations of [168] confirm the applicability of this assumption. Since the distance at turnaround is half the width the shell would have without gravitational accretion onto the wake, the shock occurs at a distance 1/4 of that which the matter shell would have under unperturbed Hubble expansion. Hence, the average density inside the wake is four times the background density, a result which will be used several times in the computations of the following section.

The evolution of the mass shell between turnaround and shock can be followed using (6.5) and (6.7). The shock will occur when $h(q,t) = (1/2)h_{max}(q)$. A straightforward computation shows that at this point the velocity is given by

$$\dot{h}(q,t) \ = \ -\frac{4\pi}{5} G\mu v_s \gamma_s \bigl(\frac{z_i+1}{z+1}\bigr)^{1/2} . \tag{6.10}$$

It is this velocity which then determines the temperature inside the shocked region.

The shocks will lead to thermalization of the wake. The gas temperature will be given by

$$\frac{3}{2} k_B T \ = \ \frac{1}{2} m v^2 \, , \tag{6.11}$$

where m is the mass of a HI atom and v is the velocity of the in-falling particles when they hit the shock, which is given by

$$v = \dot{h}(q(t), t) , \tag{6.12}$$

where $q(t)$ is the comoving distance of the shell which starts to collapse at the time t.

Inserting the result (6.10) into (6.12) and then into (6.11) we obtain the following result for the temperature T_K of the HI atoms inside the wake

$$\begin{aligned} T_K &= \frac{16\pi^2}{75}(G\mu)^2(v_s\gamma_s)^2\frac{z_i+1}{z+1}k_B^{-1}m \\ &\simeq [20 \text{ K}](G\mu)_6^2(v_s\gamma_s)^2\frac{z_i+1}{z+1} , \end{aligned} \tag{6.13}$$

where in the second line we have written the result in degrees K and expressed $G\mu$ in units of 10^{-6} (and kept only one significant figure in reporting the final number). The wake temperature is largest for wakes produced at the earliest times since the initial wake density is then the highest, and increases as time increases because more matter has time to accrete.

Assuming values of $G\mu = 3 \times 10^{-7}$ (the current upper bound on the string tension), $z_i = 10^3$, (close to the time of recombination), $z + 1 = 30$ and $(v_s\gamma_s)^2 = 1/3$, Eq. (6.13) yields $T_K \sim 20K$. This temperature is smaller than the CMB temperature $T_\gamma \simeq 82K$ at this redshift. As we will see in the following section, this leads to an absorption signal in the 21 cm radiation.

The formation of a cosmic string wake and the thermalization which takes place inside the shocked region has been studied in [168] using an Eulerian hydro code [169] optimized to resolve shocks. The numerical simulations of [168] show that the density and temperature inside the shocked region are indeed roughly uniform and that the temperature obtained agrees with the values obtained here using analytical approximations.

Looking for signals from cosmic strings in 21 cm surveys is potentially more powerful than looking in large-scale optical redshift surveys. This is because firstly the non-Gaussian signatures from strings are more pronounced at higher redshifts, secondly because we are directly looking at the distribution of the baryons, and not just the distribution of stars, the latter being affected by non-linear and gas dynamics, and thirdly because the distribution of matter is more linear at higher redshifts and hence easier to follow analytically. Compared to CMB and CMB polarization maps, 21 cm surveys have the advantage of yielding three- rather than just two-dimensional maps, maps thus containing much more information. To our knowledge, there has been little previous work on 21 cm emission from strings. Two exceptions are [93] in which the angular power spectrum of 21 cm emission from a network of cosmic strings was considered, and [17], a recent study in which the correlation between 21 cm emission and CMB signals from cosmic strings was studied. In contrast to these works, we are looking for direct string signals in position space 21 cm maps.

In the following section we will briefly summarize some key features of 21 cm cosmology and apply the equations for the 21 cm brightness temperature to the case of emission from a string wake.

6.4 Cosmic Strings and 21 cm Maps

Neutral hydrogen is the dominant form of baryonic matter in the "dark ages", i.e. before star formation. Neutral hydrogen has a 21 cm hyperfine transition line which is excited if the hydrogen gas is at finite temperature. Hence, we expect redshifted 21 cm radiation to reach us from all directions in the sky, and the intensity of this radiation can tell us about the distribution of neutral hydrogen in the universe, as a function of both angular coordinates in the sky and redshift. Thus, in contrast to the CMB, 21 cm surveys can probe the three-dimensional distribution of matter in the universe (see [77, 159, 110] for pioneering papers on the cosmology of the 21 cm line and [65] for an in-depth review).

Let us now consider the equation of radiative transfer along the line of sight through a hydrogen gas cloud of uniform temperature- in the case of interest to us this gas cloud is the cosmic string wake. The brightness temperature

$T_b(\nu)$ at an observed frequency ν due to 21 cm emission is given by

$$T_b(\nu) \;=\; T_S\big(1 - e^{-\tau_\nu}\big) + T_\gamma(\nu) e^{-\tau_\nu}\,, \tag{6.14}$$

where T_S is the spin temperature, T_γ is the microwave radiation temperature, and τ_ν is the optical depth obtained by integrating the absorption coefficient along the light ray through the gas cloud. The frequency ν is the blue-shifted frequency at the position of the cloud corresponding to the observed frequency ν_o. The term proportional to T_S is due to spontaneous emission, while the term proportional to T_γ is due to absorption and stimulated emission.

As explained in [65], what is of observational interest is the comparison of the temperature coming from the hydrogen cloud with the "clear view" of the 21 cm radiation from the CMB.

$$\delta T_b(\nu) \;=\; \frac{T_b(\nu) - T_\gamma(\nu)}{1+z} \;\approx\; \frac{T_S - T_\gamma(\nu)}{1+z}\tau_\nu\,. \tag{6.15}$$

Note that the "clear view" of the CMB is hypothetical since even without a string wake's gas cloud the intergalactic medium is partly a less dense hydrogen gas. In the second part of the equation above we have expanded the exponential factor to linear order in the optical depth.

The spin temperature T_S is defined as the relative number density of atoms in the hyperfine energy states through $n_1/n_0 \;=\; 3\exp(-T_\star/T_S)$. Here n_1 and n_0 are the number densities of atoms in the two hyperfine states, and $T_\star = E_{10}/k_B = 0.068\text{K}$ is the temperature corresponding to the energy splitting E_{10} between these states.

The spin temperature is determined solely by the temperature T_K of the gas in the wake, as long as UV scattering is negligible (which is true in our case). The relationship between spin and kinetic gas temperatures is expressed through the collision coefficients x_c which describe the rate of scattering among hydrogen atoms and electrons:

$$T_S \;=\; \frac{1+x_c}{1+x_c T_\gamma/T_K} T_\gamma\,. \tag{6.16}$$

We will shortly discuss the numerical values of the x_c for a particular case of interest.

Combining (6.15) and (6.16) we find for the difference $\delta T_b(\nu)$ in brightness temperature induced by the interaction of the radiation with neutral hydrogen is

$$\delta T_b(\nu) \simeq T_S \frac{x_c}{1+x_c}\big(1 - \frac{T_\gamma}{T_K}\big)\tau_\nu (1+z)^{-1}\,, \tag{6.17}$$

where the last factor represents the red-shifting of the temperature between the time of emission and the present time. It is important to keep in mind that the brightness temperature from a region of space without density perturbations is nonzero. It is negative since the temperature of gas after redshift 200 is lower than that of the CMB photons, the former red-shifting as $(z(t)+1)^2$, the latter as $z(t)+1$. The optical depth of a cloud of hydrogen is

$$\tau_\nu = \frac{3c^2 A_{10}}{4\nu^2}\big(\frac{\hbar\nu_{10}}{k_B T_S}\big)\frac{N_{HI}}{4}\phi(\nu)\,, \tag{6.18}$$

where N_{HI} is the column density of HI.

Up to this point, the analysis has been general. Let us now specialize to the case where the gas cloud is the gas inside the cosmic string wake. In this case, the column density is the hydrogen number density n_{HI}^{wake} times the length that the light ray traversed in the cloud. This length will depend on the width h of the wake and the angle θ that the light ray makes relative to the vertical to the wake so that

$$N_{HI} = \frac{2 n_{HI}^{wake} h}{\cos\theta}\,. \tag{6.19}$$

The factor of 2 results since h is the width of the wake from the center.

The line profile $\phi(\nu)$ is due to broadening of the emission line. This broadening reflects the fact that not all photons resulting from the hyperfine transition will leave the gas cloud at the same frequency. Frequency differences are in general due to thermal motion, bulk motion and pressure effects. Since the pressures we are considering are small by astrophysical standards, pressure broadening is negligible. Since the gas temperature inside the wake is not much larger than the CMB temperature, thermal broadening will not be important, either. This leaves us with the effects of bulk motion, more specifically the expansion of the wake in planar directions. The line profile is normalized such that the integral of it over frequency is unity.

The origin of the line broadening due to the expansion of the wake is illustrated in Figure 6.4. Let us consider a point on the wake for which the photons travel to us at an angle which is not orthogonal to the plane of the wake. Then, relative to photons emitted at the central point on the photon path, photons emitted from the highest point and the lowest point obtain a relative Doppler shift of

$$\frac{\delta\nu}{\nu} = 2\sin(\theta)\tan\theta\frac{Hh}{c}, \tag{6.20}$$

where H is the expansion rate of space and h is the wake width computed in the previous section, both evaluated at the redshift z when the photons are emitted. The angle θ is indicated in Figure 6.4. It is the angle relative to the vertical to the wake. As a consequence of the normalization of $\phi(\nu)$ we hence find

$$\phi(\nu) = \frac{1}{\delta\nu} \text{ for } \nu \,\epsilon\, [\nu_{10} - \frac{\delta\nu}{2}, \nu_{10} + \frac{\delta\nu}{2}], \tag{6.21}$$

and $\phi(\nu) = 0$ otherwise.

In addition to its role in determining the brightness temperature, the frequency shift $\delta\nu$ is important since it determines the width of the 21 cm signal of strings in the redshift direction and is hence central to the issue of observability of the signal. From (6.20) and (6.8) (and setting the $2\sin\theta\tan\theta$ factor to one) we find that

$$\begin{aligned} \frac{\delta\nu}{\nu} &= \frac{24\pi}{15}G\mu v_s\gamma_s\big(z_i+1\big)^{1/2}\big(z(t)+1\big)^{-1/2} \\ &\simeq 3\times10^{-5}(G\mu)_6(v_s\gamma_s), \end{aligned} \tag{6.22}$$

where in the second line we have used the cosmological parameters mentioned at the end of the introductory section and inserted the representative redshifts $z_i + 1 = 10^3$ and $z(t) + 1 = 30$.

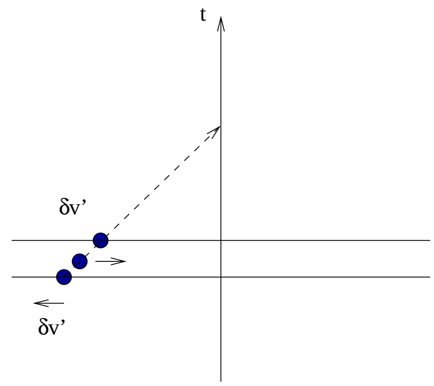

Figure 6.2: Photons reaching us from a particular direction given by the angle θ to the vertical to the wake are emitted at different points in the wake. Three such points are indicated in the Figure - the central point and two points on the bottom and top of the wake, respectively. Since the wake is undergoing Hubble expansion in its planar directions, there is a relative Doppler frequency shift $\delta\nu$ between the 21 cm photons from the top and the center of the wake.

Taking the formula (6.17) for the brightness temperature, inserting the results (6.18) for the optical depth and (6.20) and (6.21) for the line profile, we get

$$\begin{aligned}\delta T_b(\nu) &= 2\frac{x_c}{1+x_c}\big(1-\frac{T_\gamma}{T_K}\big)\frac{3c^3 A_{10}\hbar}{16\nu_{10}^2 k_B H_0 \Omega_m^{1/2}} \\ &\times n_{HI}^{bg}(t_0)\frac{n_{HI}^{wake}(t_0)}{n_{HI}^{bg}(t_0)} \\ &\times (2\sin^2(\theta))^{-1}(1+z)^{1/2}\,, \end{aligned} \tag{6.23}$$

where Ω_m is the fraction of the critical energy density which is in the form of matter. Here the ratio of the density inside the wake to the background density, $n_{HI}^{wake}/n_{HI}^{bg}$, is approximately 4. We have rescaled the Hubble constant and the background HI density to its current values H_0 and $n_{HI}^{bg}(t_0)$, respectively, and made use of $H(z) = H_0\Omega_m^{1/2}(1+z)^{3/2}$ in the re-scaling. Note that the width of the wake has cancelled out between the HI column density and the line profile. The width of the wake, however, has not disappeared completely from the calculation since it determines the wake temperature T_K, and since it yields the width of the signal in redshift direction.

Taking the values $A_{10} = 2.85\times10^{-15}\,\mathrm{s}^{-1}$, $T_\star = 0.068\,\mathrm{K}$, $H_0 = 73\,\mathrm{km\ s^{-1}\ Mpc^{-1}}$, $\nu_{10} = 1420$ MHz, $\Omega_b = 0.042$, $\Omega_m = 0.26$, $2\sin^2\theta = 1$, eq. (6.23) becomes

$$\delta T_b(\nu) \;=\; [0.07\ \mathrm{K}]\frac{x_c}{1+x_c}\big(1-\frac{T_\gamma}{T_K}\big)(1+z)^{1/2}\,. \qquad (6.24)$$

The collision coefficient x_c is dominated by the hydrogen-hydrogen collisions because of the very low fraction of free electrons. It is given by [199, 64]

$$x_c \;=\; \frac{n\kappa_{10}^{HH}}{A_{10}}\frac{T_\star}{T_\gamma}\,. \qquad (6.25)$$

where κ_{10}^{HH} is the de-excitation cross section and is approximately $2.7\times10^{-11}\mathrm{cm}^3\mathrm{s}^{-1}$ at a wake gas temperature of $T_K = 20K$ [199, 64]. This temperature corresponds to the parameter values we took at the end of Section 2, i.e. $(G\mu)_6 = 0.3$, $(v_s\gamma_s)^2 = 1/3$, $z_i = 10^3$ and $z{+}1 = 30$. Remembering that the density n inside the wake is four times the background density $n_{bg} = 1.9\times10^{-7}\mathrm{cm}^{-3}(1{+}z)^3$ we find for a redshift $1+z = 30$ that $x_c \simeq 0.16$ and hence (from (6.24)) $\delta T_b(\nu) \simeq -160$ mK. For a formation redshift $z_i = z_{eq} = 3200$ corresponding to the time of equal matter and radiation the corresponding temperature is $\delta T_b(\mu) \simeq -15$ mK. Note that the dependence of the above result on the cosmic string tension μ enters only through the wake temperature. Note also that in the large $G\mu$ limit ($G\mu \gg 10^{-6}$), the brightness temperature approaches a constant value of close to 400mK.

There is a critical value of the string tension (which depends on the redshift) at which the cosmic string signal changes from emission to absorption. This value is determined by $T_K = T_\gamma$ which yields

$$(G\mu)_6^2 \;\simeq\; 0.1(v_s\gamma_s)^{-2}\,\frac{(z+1)^2}{z_i+1} \;\simeq\; 0.4\,\frac{(z+1)^2}{z_i+1}\,, \qquad (6.26)$$

for the value $(v_s\gamma_s)^2 = 1/3$ which we are using throughout, and this corresponds to $(G\mu)_6 \simeq 0.6$ if we use $(z_i{+}1) = 10^3$ and insert our reference redshift of $z+1 = 30$. At a redshift of $z+1 = 20$ the critical value is $(G\mu)_6 \simeq 0.4$. For a formation time corresponding to the redshift of equal matter and radiation the critical value of $G\mu$ is a factor of two lower.

For lower values of the tension the cosmic string signal in the 21 cm maps shifts from an emission signal to an absorption signal. However, two effects must be taken into account when discussing the visibility of the string signal. The first is the fact that at very small values of $G\mu$ our calculation of the wake temperature breaks down. This occurs when the resulting wake temperature computed in (6.13) is smaller than the gas temperature obtained by taking the background gas temperature and computing its increase under adiabatic compression to the overdensity of the wake. In this case it is no longer justified to take the initial conditions (6.6). At redshifts z below 150 the cosmic gas is cooling adiabatically as

$$T_g \,=\, 0.02\mathrm{K}(1+z)^2 \tag{6.27}$$

because at this point Compton heating of the gas by the CMB is negligible [160, 161]. Setting $T_K = 2.5 \times T_g$ (the factor 2.5 being due to the fact that for adiabatic compression of a mono-atomic gas by a factor of 4 in volume, one expects a temperature increase by a factor of $4^{2/3} \sim 2.5$) yields (for our standard values of $1 + z_i = 10^3$ and $(v_s\gamma_s)^2 = 1/3$)

$$(G\mu)_6 \,\simeq\, 3 \times 10^{-3}(1+z)^{3/2} \tag{6.28}$$

which equals $(G\mu)_6 = 0.5$ at a redshift of $1 + z = 30$. For a formation redshift $z_i = z_{eq}$ the factor 3 in (6.28) is replaced by 2.

For values of $G\mu$ smaller than the one given in (6.28), the effects of thermal pressure start to become important, and this will effect both the density and temperature structure in the wake.

Our results are illustrated in Figure 6.3 which shows a comparison of the temperatures relevant to the above discussion and their dependence on redshift. The vertical axis is the temperature axis, the horizontal axis is inverse redshift. The magenta (dashed) line shows the CMB temperature T_γ, the orange (dotted) line is the gas temperature in a wake $2.5T_g$ after adiabatic contraction. The two solid lines with the positive slope represent T_K for two different values of $G\mu$. The upper curve is for $(G\mu)_6 = 1$, the lower curve for

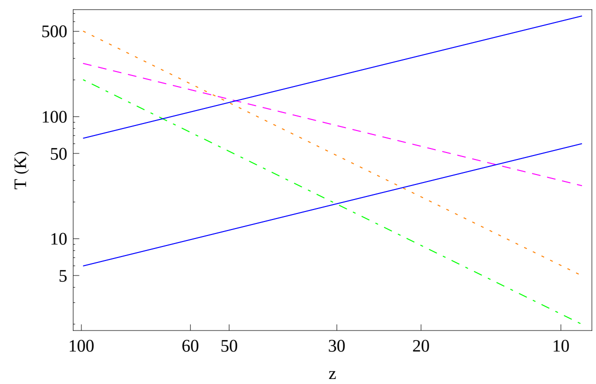

Figure 6.3: The redshift dependence of the relevant temperatures. The magenta dashed line is the CMB temperature T_γ, the orange dotted line is $2.5T_g$, the gas temperature after adiabatic contraction by a factor 4 in volume, and the green (dot-dashed) line is the T_g curve. The two solid curves with positive slope represent T_K for two different values of $G\mu$, $(G\mu)_6 = 1$ in the case of the upper curve and $(G\mu)_6 = 0.3$ in the case of the lower curve (in both cases for a formation redshift $z_i + 1 = 10^3$). Following one of the solid curves, we see that the 21 cm string signal is an emission signal above the magenta curve and an absorption signal below it. The wake temperature is given by T_K only above the orange curve. For higher redshifts, the initial gas temperature dominates the final temperature of the gas inside the wake, and the latter follows the orange curve. Once T_K drops below the green curve, there will no longer be any shock and our effect disappears.

$(G\mu)_6 = 0.3$. Along a fixed $G\mu$ curve, the 21 cm signal of a cosmic string is an emission signal above the T_γ curve and an absorption signal below it. Above the $2.5T_g$ curve, the temperature of the gas inside the wake is well approximated by the equation (6.13), below it the initial thermal gas temperature effects dominate and the wake temperature will follow the $2.5T_g$ curve. The wake temperature curves are for a formation redshift of $z_i + 1 = 10^3$.

The second issue is that the string signal must be compared to what would be seen if the wake region were replaced by unclustered neutral gas. In this case, the absorption signal has a temperature given by (6.24) with T_K replaced by T_g and the collision coefficient computed with T_g instead of T_K. Due to the overdensity of the wake, the signal of a string wake should persist. The overdensity in the string wake by a factor of 4 will lead to an enhancement in the magnitude of the brightness temperature by a factor of 16 compared to what would be seen if the wake region were replaced by unclustered gas. One factor of 4 comes from the fact that the collision coefficient is proportional to the gas density, the second from the fact that the optical depth is also proportional to the density. In addition, the temperature ratios in (6.24) are different.

However, for values of $G\mu$ so small that $T_K \ll T_g$ there will no longer be any shock and hence no well-defined wake region with overdensity 4. This will occur at a value of $G\mu$ which is smaller than the limit in (6.28) by a factor of $\sqrt{2.5}$. Note also that the thickness in redshift space (discussed below) of the signal decreases as $G\mu$ decreases, and hence improved sensitivity will be required to detect the signal.

The bottom line of the above analysis is that at a redshift of $z + 1 = 30$, strings with tensions below the current observational limit are predicted to be visible in absorption in 21 cm surveys. Strings with larger tensions would yield an emission signal. The critical value (6.26) of $G\mu$ at which the emission signal turns into an absorption signal decreases as z decreases, so that strings with tensions at the current observational limit would become visible in emission at a redshift of below 20. However, the value of z cannot be smaller than that corresponding to reionization since we have not considered how UV scattering affects the spin temperature.

The 21 cm signature of a cosmic string wake has a distinctive shape in redshift space. The string signal will be a wedge-like region of extra 21 cm emission. The signal will be wide in the two angular directions, and narrow in redshift direction [1] . The projection of this region onto the plane corresponding to the two angles in the sky (we are working in the limit of small angles and thus can use the flat sky approximation) corresponds to the projection of the wake onto the observer's past light cone. The orientation of the wedge in redshift

[1] The signal at a fixed redshift would be extended only in one angular direction.

space is given by the orientation of the wake relative to the observer's light cone. This is illustrated in Figure 6.4. The left panel is a space-time sketch of the geometry (with two spatial directions suppressed). The wake is created by a string segment which starts out at time t_i at the position x_1 and which at time $2t_i$ (roughly one Hubble time step later) has moved to the position x_2 (the arrow on the segment connecting the two events gives the direction of the velocity of the string segment. For the orientation of the string chosen, the past light cone intersects the "back" of the string wake at a later time than the front. Hence, the 21 cm signal has a larger red-shift for photons from the tip of the wake than from the back side of the wake. The width of the wake vanishes at the tip and increases towards the back. Hence, in redshift space the region of extra 21 cm emission has the orientation sketched on the right panel of Figure 6.4. The planar dimensions of the region of extra emission are in the angular directions, and their sizes are the angles corresponding to the comoving area (see (6.4))

$$c_1 t_i (z_i + 1) \times t_i v_s \gamma_s (z_i + 1)\,. \tag{6.29}$$

The amplitude of the emission signal depends on the orientation of the wake relative to us (through the redshift when our past light cone intersects the various parts of the wake). This is not correlated with the direction of string motion. The width in redshift space, on the other hand, depends on the emission point on the wake - the width is larger in the back and approaches zero at the tip, as given by $\delta\nu$ (see 6.20).

6.5 Conclusions and Discussion

In this paper we have calculated the 21 cm signal of a single cosmic string wake. We found that wakes leave a characteristic signal in 21 cm surveys - wedge shaped regions of extra emission or absorption, depending on the value of the string tension. There is an emission signal as long as the string tension exceeds the critical value given by (6.26) and as the tension increases the temperature approaches the value given by 200mK, a value larger by almost two

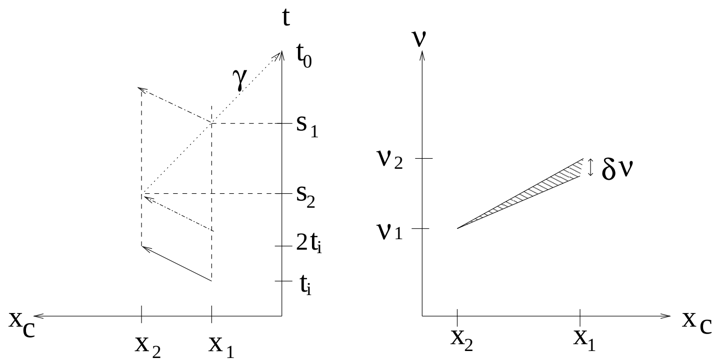

Figure 6.4: Geometry of the 21 cm signal of a cosmic string wake. The left panel is a sketch of the geometry of the wake in space-time - vertical axis denoting time, the horizontal axis one direction of space. The string segment producing the wake is born at time t_i and travels in the direction of the arrow, ending at the position x_2 at the time $2t_i$. The past light cone of the observer at the time t_0 intersects the tip of the wake at the time s_2, the back of the wake at time s_1. These times are in general different. Hence, the 21 cm radiation from different parts of the wake is observed at different red-shifts. The resulting angle-redshift signal of the string wake shown in the left panel is illustrated in the right panel, where the horizontal axis is the same spatial coordinate as in the left panel, but the vertical axis is the redshift of the 21 cm radiation signal. The wedge in 21 cm has vanishing thickness at the tip of the wedge, and thickness given by $\delta\nu$ at the back side.

orders of magnitude compared to the backgrounds from standard cosmology sources which the Square Kilometer Array (SKA) telescope project is designed to be sensitive to [38, 39]. For values of $G\mu$ below the critical value given by (6.26), the cosmic string wake signal changes to an absorption signal. This will persist down to a value of $G\mu$ a factor of $\sqrt{2.5}$ smaller than the value given in (6.28), at which point the material which is gravitationally attracted to the wake will no longer undergo a shock and hence our analysis ceases to be applicable. The width of the wedge in redshift space depends on the string tension via (6.20). The width increases from zero at the tip of the string to the value given by (6.20) at the midpoint of the wake.

The sensitivity of 21 cm surveys to cosmic strings is best at the lowest redshifts sufficiently higher than the redshift of reionization. This is due to the fact that the string wakes keep increasing in width as a function of time, leading to an increasing temperature of the gas in the wake and hence to a higher 21 cm signal. At the same time, the wakes become more stable towards thermal disruption.

As mentioned above, the brightness temperature shift which we predict will be large compared to that from the surrounding intergalactic medium. The fractional frequency width of the signal is given by (6.22) and is near the limit of the frequency resolution of radio telescopes for values of $G\mu$ close to the current upper bound. For example, the Square Kilometer Array will have a fractional spectral resolution of the order [38, 39] of 10^{-4}. In both angular directions, the signal will cover a rectangle whose side length is given by the comoving Hubble radius at the redshift z_i, which for redshifts close to recombination corresponds to a scale of about one degree. Thus, the signal of cosmic strings which we predict is clearly a possible target for future radio telescopes. For example, the angular resolution of the SKA is designed to be smaller than 0.1 arcsec, and the frequency range of the SKA will allow the detection of the 21 cm signal up to a redshift of 20.

We have focused on the signal of a single wake laid down at a time $t > t_{eq}$. The reader may worry that the signal of such a wake is masked by the "noise" due to wakes laid down at earlier times. Even though the baryons will stream out of these wakes due to their coupling with the photons, the dark matter wakes persist. For $t < t_{eq}$ the dark matter wakes do not grow in thickness until $t = t_{eq}$. After that, the thickness will begin to grow, and at $t > t_{rec}$ the baryons will start to fall into the dark matter potential wells. However, the width of such wakes (averaged over the length of the wake) is smaller than that of wakes at $t = t_{eq}$. In addition, due to their large number, on length scales of wakes laid down at $t \geq t_{eq}$, the earlier wakes will act like Gaussian noise. The coherent signature in position space of such a "late" wake can be picked out of the Gaussian noise even if the amplitude of the Gaussian noise is comparable to or slightly larger than the amplitude of the signal (as measured in terms of the contribution to the power spectrum). This has been studied in the context of picking out the signatures of late strings in CMB temperature maps in [6, 173, 52, 53], and we expect similar conclusions to hold here.

Let us end with a brief comparison of our work with that of [93] and [17] who also considered 21 cm signals of cosmic strings. What sets our work apart is that we focus on the specific position space signature of wakes rather than on the (Fourier space) power spectrum. In computing a power spectrum, one loses the information about the non-Gaussianities in the distribution of strings. It is these non-Gaussianities which most clearly distinguish the predictions of a string model from a model with only Gaussian fluctuations. Therefore, the sensitivity to the presence of cosmic strings will be much higher in a study like ours compared to what can be achieved by only computing power spectra.

6.6 Summary

In this section we found the 21 cm signature for cosmic string wakes, completing our survey of cosmic string signatures in the available observational windows. It is important to note that the galactic synchrotron radiation at high galactic latitudes follows:

$$T_{sky} \sim 180\mathrm{K} \left(\frac{\nu}{180\mathrm{MHz}} \right)^{-2.6}, \tag{6.30}$$

[65]. This means that it becomes difficult to search for 21 cm signals and foreground removal is necessary. However, analogous to how we were able to dig through the gaussian fluctuations for the Kaiser-Stebbins signal of cosmic strings in temperature maps with the Canny algorithm, we could dig through the galactic foreground signal to search for the 21 cm position space wedge signature generated by cosmic string wakes.

Chapter 7

Conclusion

The turn of the nineteenth to the twentieth century could be characterized as nothing short of a revolution in physics. The new century was marked by an influx of new ideas such as special relativity, the photoelectric effect, and breakthrough discoveries such as of radiation. After such a promising beginning to the century, high energy physics developed and evolved enormously in the course of the century from the development and verification of such theories as general relativity, quantum mechanics, and particle physics to the conception of string theory, a theory unifying gravity with the strong and electroweak forces, in the latter half of the twentieth century. Cosmology, too, underwent a revolution in the twentieth century with Hubble's discovery of the expansion of the universe in the first half of the century and ending with the birth of inflation in 1980 and the discovery of the accelerated expansion of the universe expansion in 1998. The development of physics in the twenty-first century bodes to be no less revolutionary with the emergence of experiments that could conceivably find evidence for string theory and early universe theories such as GUT symmetry breaking.

Cosmic strings provide one such prediction of early universe cosmology and string theory. In this thesis we explored the signature of cosmic strings in several observational probes to provide the foundation for experimental searches. We began our exploration in Chapter 3 by applying the Canny and edge counting algorithms to simulated CMB maps with simulated inflationary fluctuations, or Gaussian maps, as well as maps simulating cosmic strings superimposed on the Gaussian maps via their influence on the CMB per the Kaiser-Stebbins effect. We used statistics to distinguish between the maps and found that our algorithm could positively distinguish between the Gaussian maps and maps with added cosmic strings.

We continued to apply the Canny algorithm to CMB maps in Chapter 4 in distinguishing between maps with three-string junctions as predicted by string theory. The power to distinguish between maps of gauge strings (which lack three-string junctions) and maps of cosmic superstrings (that include junctions) would be strongly suggestive of string theory should cosmic strings be detected. Furthermore, our analysis enables us to distinguish among different scaling solutions of cosmic strings, which could lead to further understanding of cosmic string models.

Our analyses of the signatures of the overdense wakes of cosmic strings in the polarization and 21 cm probes are timely due to an influx of polarization and 21 cm data. In Chapter 5, we found that, given ideal circumstances, cosmic string polarization would contribute at most 0.4% compared to polarization due to weak lensing. Ideal circumstances include an alignment of the cosmic string with the quadrupole, the time of formation of the wake near recombination, and string tension at about the current limits. Furthermore, the signature of a cosmic string wake in polarization data would be, with an alignment of the string in the plane perpendicular to the line of sight, rectangular regions with a brightness gradient growing in the direction of where the string wake originates. We also found that the polarization would be distributed equally in B and E modes. When used in combination with schemes such as the Canny and edge counting algorithms, polarized string wakes could potentially be detected.

In Chapter 6, we found that the additional matter in string wakes typically leads to absorption features in the 21 cm redshifted spectrum. For string wakes observed before star formation, the differential brightness temperature is -160 mK, although particularly high string tensions could theoretically lead to an emission signal. Furthermore, the signature of a cosmic string wake takes the distinctive shape of a wedge with the thickness in redshift space and the planar directions corresponding to the wake's geometry.

Although this thesis explores the signature of cosmic strings in temperature and polarization CMB maps and the 21 cm redshifted spectrum, it also raises questions and hints at future work that can be done to follow-up the work in this thesis, which we shall now discuss.

The most intuitive future work to be done on searching for signatures of cosmic strings in the CMB is to apply the Canny and edge counting algorithms to more sophisticated cosmic string simulations and small angular scale experimental data. To begin this work, we need to explore whether the cosmic string signature would survive the experimental noise and errors. Furthermore, we would need to minimize the effects of scanning strategies and include only those gradients which are not in the direction that the telescopes scan.

For the polarization and 21 cm windows, the obvious work to follow-up this thesis would be to simulate maps of networks of cosmic strings. In our analyses we considered single strings in ideal conditions. Hence, it is important to simulate realistic string networks and their wake signatures to determine how this complicates the signal. Moreover, we would need to develop new techniques and apply new statistical measures to search for cosmic string signatures in these networks.

As we continue in our twenty-first century era of precision cosmology, current and future experiments offer promising means to search for the signatures of cosmic strings and the possible confirmation of Grand Unified Theories as well as string theory. In this thesis we have built bridges between specific fossils of high energy physics in the early universe — cosmic strings — and observation — their observational signal — and built the infrastructure to mine current and future observational data.

References

[1] Anthony N. Aguirre and Robert H. Brandenberger. Accretion of hot dark matter onto slowly moving cosmic strings. *Int. J. Mod. Phys.*, D4:711–722, 1995.

[2] Andreas Albrecht, Richard A. Battye, and James Robinson. A detail study of defect models for cosmic structure formation. *Phys. Rev.*, D59:023508, 1999.

[3] Andreas Albrecht, David Coulson, Pedro Ferreira, and Joao Magueijo. Causality and the microwave background. *Phys. Rev. Lett.*, 76:1413–1416, 1996.

[4] Andreas Albrecht and N. Turok. Evolution of Cosmic Strings. *Phys. Rev. Lett.*, 54:1868–1871, 1985.

[5] Bruce Allen and E. P. S. Shellard. Cosmic String Evolution: A Numerical Simulation. *Phys. Rev. Lett.*, 64:119–122, 1990.

[6] Stephen Amsel, Joshua Berger, and Robert H. Brandenberger. Detecting Cosmic Strings in the CMB with the Canny Algorithm. *JCAP*, 0804:015, 2008.

[7] Richard Battye and Adam Moss. Updated constraints on the cosmic string tension. *Phys. Rev.*, D82:023521, 2010.

[8] Richard A. Battye, Bjorn Garbrecht, and Adam Moss. Constraints on supersymmetric models of hybrid inflation. *JCAP*, 0609:007, 2006.

[9] Richard A. Battye, Bjorn Garbrecht, Adam Moss, and Horace Stoica. Constraints on Brane Inflation and Cosmic Strings. *JCAP*, 0801:020, 2008.

[10] Daniel Baumann et al. CMBPol Mission Concept Study: A Mission to Map our Origins. *AIP Conf. Proc.*, 1141:3–9, 2009.

[11] K. Benabed and F. Bernardeau. Cosmic string lens effects on CMB polarization patterns. *Phys. Rev.*, D61:123510, 2000.

[12] C. L. Bennett, M. Bay, M. Halpern, G. Hinshaw, C. Jackson, N. Jarosik, A. Kogut, M. Limon, S. S. Meyer, L. Page, D. N. Spergel, G. S.

Tucker, D. T. Wilkinson, E. Wollack, and E. L. Wright. The Microwave Anisotropy Probe Mission. *Astrophys. J.*, 583:1–23, January 2003.

[13] C. L. Bennett et al. First Year Wilkinson Microwave Anisotropy Probe (WMAP) Observations: Preliminary Maps and Basic Results. *Astrophys. J. Suppl.*, 148:1, 2003.

[14] C. L. Bennett, M. Halpern, G. Hinshaw, N. Jarosik, A. Kogut, M. Limon, S. S. Meyer, L. Page, D. N. Spergel, G. S. Tucker, E. Wollack, E. L. Wright, C. Barnes, M. R. Greason, R. S. Hill, E. Komatsu, M. R. Nolta, N. Odegard, H. V. Peiris, L. Verde, and J. L. Weiland. First-Year Wilkinson Microwave Anisotropy Probe (WMAP) Observations: Preliminary Maps and Basic Results. *Astrophys. J. Supp.*, 148:1–27, September 2003.

[15] C. L. Bennett, M. Halpern, G. Hinshaw, N. Jarosik, M. Limon, J. Mather, S. S. Meyer, L. Page, D. N. Spergel, G. Tucker, D. T. Wilkinson, E. Wollack, and E. L. Wright. The Microwave Anisotropy Probe (MAP) Mission. In *Bulletin of the American Astronomical Society*, volume 29 of *Bulletin of the American Astronomical Society*, pages 1353–+, December 1997.

[16] David P. Bennett and Francois R. Bouchet. Evidence for a Scaling Solution in Cosmic String Evolution. *Phys. Rev. Lett.*, 60:257, 1988.

[17] Aaron Berndsen, Levon Pogosian, and Mark Wyman. Correlations between 21 cm Radiation and the CMB from Active Sources. *Mon. Not. Roy. Astron. Soc.*, 407:1116, 2010.

[18] Neil Bevis, Mark Hindmarsh, Martin Kunz, and Jon Urrestilla. CMB power spectrum contribution from cosmic strings using field-evolution simulations of the Abelian Higgs model. *Phys. Rev.*, D75:065015, 2007.

[19] Neil Bevis, Mark Hindmarsh, Martin Kunz, and Jon Urrestilla. Fitting CMB data with cosmic strings and inflation. *Phys. Rev. Lett.*, 100:021301, 2008.

[20] J. R. Bond and G. Efstathiou. Cosmic background radiation anisotropies in universes dominated by nonbaryonic dark matter. *Astrophys. J.*, 285:L45–L48, 1984.

[21] J. R. Bond and G. Efstathiou. The statistics of cosmic background radiation fluctuations. *Mon. Not. Roy. Astron. Soc.*, 226:655–687, 1987.

[22] F. R. Bouchet, P. Peter, A. Riazuelo, and M. Sakellariadou. Is there evidence for topological defects in the BOOMERANG data? *Phys. Rev.*, D65:021301, 2002.

[23] Francois R. Bouchet and David P. Bennett. Does The Millisecond Pulsar Constrain Cosmic Strings? *Phys. Rev.*, D41:720–723, 1990.

[24] Robert Brandenberger, Hassan Firouzjahi, and Johanna Karouby. Lensing and CMB Anisotropies by Cosmic Strings at a Junction. *Phys. Rev.*, D77:083502, 2008.

[25] Robert H. Brandenberger. Inflationary cosmology: Progress and problems. Invited talk at IPM School on Cosmology 1999: Large Scale Structure Formation, Tehran, Iran, 23 Jan - 4 Feb 1999.

[26] Robert H. Brandenberger. String Gas Cosmology. String Cosmology, J.Erdmenger (Editor). Wiley, 2009. p.193-230.

[27] Robert H. Brandenberger. On the decay of cosmic string loops. *Nucl. Phys.*, B293:812, 1987.

[28] Robert H. Brandenberger. Topological defects and structure formation. *Int. J. Mod. Phys.*, A9:2117–2190, 1994.

[29] Robert H. Brandenberger, Rebecca J. Danos, Oscar F Hernandez, and Gilbert P. Holder. The 21 cm Signature of Cosmic String Wakes. *JCAP*, 1012:028, 2010.

[30] Robert H. Brandenberger, David M. Kaplan, and Stephen A. Ramsey. Some statistics for measuring large scale structure. 1993.

[31] Robert H. Brandenberger, Ali Nayeri, Subodh P. Patil, and Cumrun Vafa. String gas cosmology and structure formation. *Int. J. Mod. Phys.*, A22:3621–3642, 2007.

[32] Robert H. Brandenberger, Leandros Perivolaropoulos, and Albert Stebbins. Cosmic strings, hot dark matter and the large scale structure of the universe. *Int. J. Mod. Phys.*, A5:1633, 1990.

[33] Robert H. Brandenberger and Neil Turok. Fluctuations from cosmic strings and the microwave background. *Phys. Rev.*, D33:2182, 1986.

[34] Robert H. Brandenberger and C. Vafa. Superstrings in the Early Universe. *Nucl. Phys.*, B316:391, 1989.

[35] Martin Bucher and David N. Spergel. Is the dark matter a solid? *Phys. Rev.*, D60:043505, 1999.

[36] F. John Canny. A Computational Approach to Edge Detection. *IEEE Transactions On Pattern Analysis And Machine Intelligence*, 8(6):679–698, 1986.

[37] J. F. Canny. Finding edges and lines in images. Technical report, June 1983.

[38] C. L. Carilli and S. Rawlings. Motivation, key science projects, standards and assumptions. *New Astronomy Reviews*, 48:979–984, December 2004.

[39] Chris Carilli et al. Probing the Dark Ages with the Square Kilometer Array. *New Astron. Rev.*, 48:1029–1038, 2004.

[40] Sean M. Carroll. Spacetime and geometry: An introduction to general relativity. San Francisco, USA: Addison-Wesley (2004) 513 p.

[41] B. Carter. Integrable equation of state for noisy cosmic string. *Phys. Rev.*, D41:3869–3872, 1990.

[42] Tzu-Ching Chang, Ue-Li Pen, Kevin Bandura, and Jeffrey B. Peterson. Hydrogen 21-cm Intensity Mapping at redshift 0.8. *Nature*, 466:463–465, 2010.

[43] J. C. Charlton. Cosmic string wakes and large-scale structure. *Astrophys. J.*, 325:521–530, February 1988.

[44] H. C. Chiang et al. Measurement of CMB Polarization Power Spectra from Two Years of BICEP Data. *Astrophys. J.*, 711:1123–1140, 2010.

[45] E. J. Copeland, T. W. B. Kibble, and Daniele A. Steer. Collisions of strings with Y junctions. *Phys. Rev. Lett.*, 97:021602, 2006.

[46] E. J. Copeland, T. W. B. Kibble, and Daniele A. Steer. Constraints on string networks with junctions. *Phys. Rev.*, D75:065024, 2007.

[47] Edmund J. Copeland, Robert C. Myers, and Joseph Polchinski. Cosmic F- and D-strings. *JHEP*, 06:013, 2004.

[48] Edmund J. Copeland and P. M. Saffin. On the evolution of cosmic-superstring networks. *JHEP*, 11:023, 2005.

[49] Yanou Cui, Stephen P. Martin, David Edgar Morrissey, and James Daniel Wells. Cosmic Strings from Supersymmetric Flat Directions. *Phys. Rev.*, D77:043528, 2008.

[50] Thibault Damour and Alexander Vilenkin. Gravitational wave bursts from cosmic strings. *Phys. Rev. Lett.*, 85:3761–3764, 2000.

[51] Thibault Damour and Alexander Vilenkin. Gravitational wave bursts from cusps and kinks on cosmic strings. *Phys. Rev.*, D64:064008, 2001.

[52] Rebecca J. Danos and Robert H. Brandenberger. Canny Algorithm, Cosmic Strings and the Cosmic Microwave Background. *Int. J. Mod. Phys.*, D19:183–217, 2010.

[53] Rebecca J. Danos and Robert H. Brandenberger. Searching for Signatures of Cosmic Superstrings in the CMB. *JCAP*, 1002:033, 2010.

[54] Rebecca J. Danos, Robert H. Brandenberger, and Gil Holder. A Signature of Cosmic Strings Wakes in the CMB Polarization. *Phys. Rev.*, D82:023513, 2010.

[55] A. C. Davis and T. W. B. Kibble. Fundamental cosmic strings. *Contemp. Phys.*, 46:313–322, 2005.

[56] P. de Bernardis et al. A Flat Universe from High-Resolution Maps of the Cosmic Microwave Background Radiation. *Nature*, 404:955–959, 2000.

[57] R. H. Dicke, P. J. E. Peebles, P. G. Roll, and D. T. Wilkinson. Cosmic Black-Body Radiation. *Astrophys. J.*, 142:414–419, 1965.

[58] Scott Dodelson. Modern cosmology. Amsterdam, Netherlands: Academic Pr. (2003) 440 p.

[59] Olivier Dore et al. The Signature of Patchy Reionization in the Polarization Anisotropy of the CMB. *Phys. Rev.*, D76:043002, 2007.

[60] J. Dunkley et al. The Atacama Cosmology Telescope: Cosmological Parameters from the 2008 Power Spectra. 2010.

[61] R. Durrer, M. Kunz, and A. Melchiorri. Cosmic Microwave Background Anisotropies from Scaling Seeds: Global Defect Models. *Phys. Rev.*, D59:123005, 1999.

[62] Aurelien A. Fraisse. Limits on Defects Formation and Hybrid Inflationary Models with Three-Year WMAP Observations. *JCAP*, 0703:008, 2007.

[63] Aurelien A. Fraisse, Christophe Ringeval, David N. Spergel, and Francois R. Bouchet. Small-Angle CMB Temperature Anisotropies Induced by Cosmic Strings. *Phys. Rev.*, D78:043535, 2008.

[64] Steven Furlanetto and Michael Furlanetto. Spin Exchange Rates in Electron-Hydrogen Collisions. *Mon. Not. Roy. Astron. Soc.*, 374:547–555, 2007.

[65] Steven Furlanetto, S. Peng Oh, and Frank Briggs. Cosmology at Low Frequencies: The 21 cm Transition and the High-Redshift Universe. *Phys. Rept.*, 433:181–301, 2006.

[66] Juan Garcia-Bellido, Ruth Durrer, Elisa Fenu, Daniel G. Figueroa, and Martin Kunz. The local B-polarization of the CMB: a very sensitive probe of cosmic defects. *Phys. Lett.*, B695:26–29, 2011.

[67] R. Gregory. Gravitational stability of local strings. *Phys. Rev. Lett.*, 59:740, 1987.

[68] S. Gupta et al. Parameter Estimation from Improved Measurements of the CMB from QUaD. *Astrophys. J.*, 716:1040–1046, 2010.

[69] D. K. Hammond, Y. Wiaux, and P. Vandergheynst. Wavelet domain Bayesian denoising of string signal in the cosmic microwave background. 2008. arXiv 0811.1267.

[70] Amihay Hanany and Koji Hashimoto. Reconnection of colliding cosmic strings. *JHEP*, 06:021, 2005.

[71] T. Hara and S. Miyoshi. Flareup of the universe after z approximately 10**2 for cosmic string model. *Prog. Theor. Phys.*, 78:1081–1098, 1987.

[72] T. Hara and S. Miyoshi. Formation of the first systems in the wakes of moving cosmic strings. *Prog. Theor. Phys.*, 77:1152–1162, 1987.

[73] Koji Hashimoto and David Tong. Reconnection of non-abelian cosmic strings. *JCAP*, 0509:004, 2005.

[74] Christopher T. Hill, Alexander L. Kagan, and Lawrence M. Widrow. Are Cosmic Strings Frustrated? *Phys. Rev.*, D38:1100, 1988.

[75] M. B. Hindmarsh and T. W. B. Kibble. Cosmic strings. *Rept. Prog. Phys.*, 58:477–562, 1995.

[76] Christopher M. Hirata and Uros Seljak. Reconstruction of lensing from the cosmic microwave background polarization. *Phys. Rev.*, D68:083002, 2003.

[77] C. J. Hogan and M. J. Rees. Spectral appearance of non-uniform gas at high Z. *Mon. Not. Roy. Astron. Soc*, 188:791–798, September 1979.

[78] Gilbert P. Holder, Kenneth M. Nollett, and Alexander van Engelen. On Possible Variation in the Cosmological Baryon Fraction. *Astrophys. J.*, 716:907–913, 2010.

[79] Wayne Hu. Reionization Revisited: Secondary CMB Anisotropies and Polarization. *Astrophys. J.*, 529:12, 2000.

[80] Wayne Hu and Martin J. White. A CMB Polarization Primer. *New Astron.*, 2:323, 1997.

[81] J. D. Jackson. *Classical Electrodynamics, 3rd Edition.* July 1998.

[82] Mark G. Jackson, Nicholas T. Jones, and Joseph Polchinski. Collisions of cosmic F- and D-strings. *JHEP*, 10:013, 2005.

[83] Rachel Jeannerot. A Supersymmetric SO(10) Model with Inflation and Cosmic Strings. *Phys. Rev.*, D53:5426–5436, 1996.

[84] Rachel Jeannerot, Jonathan Rocher, and Mairi Sakellariadou. How generic is cosmic string formation in SUSY GUTs. *Phys. Rev.*, D68:103514, 2003.

[85] Frederick A. Jenet et al. Upper bounds on the low-frequency stochastic gravitational wave background from pulsar timing observations: Current limits and future prospects. *Astrophys. J.*, 653:1571–1576, 2006.

[86] Eunhwa Jeong and George F. Smoot. Search for cosmic strings in CMB anisotropies. *Astrophys. J.*, 624:21–27, 2005.

[87] Eunwhwa Jeong and G. F. Smoot. The Validity of the Cosmic String Pattern Search with the Cosmic Microwave Background. 2006.

[88] N. Kaiser. Small-angle anisotropy of the microwave background radiation in the adiabatic theory. *"Mon. Not. Roy. Astron. Soc."*, 202:1169–1180, March 1983.

[89] Nick Kaiser and A. Stebbins. Microwave Anisotropy Due to Cosmic Strings. *Nature*, 310:391–393, 1984.

[90] Marc Kamionkowski, Arthur Kosowsky, and Albert Stebbins. Statistics of Cosmic Microwave Background Polarization. *Phys. Rev.*, D55:7368–7388, 1997.

[91] M. Kaplinghat et al. Probing the Reionization History of the Universe using the Cosmic Microwave Background Polarization. *Astrophys. J.*, 583:24–32, 2003.

[92] V. M. Kaspi, J. H. Taylor, and M. F. Ryba. High - precision timing of millisecond pulsars. 3: Long - term monitoring of PSRs B1855+09 and B1937+21. *Astrophys. J.*, 428:713, 1994.

[93] Rishi Khatri and Benjamin D. Wandelt. Cosmic (super)string constraints from 21 cm radiation. *Phys. Rev. Lett.*, 100:091302, 2008.

[94] Justin Khoury, Burt A. Ovrut, Paul J. Steinhardt, and Neil Turok. The ekpyrotic universe: Colliding branes and the origin of the hot big bang. *Phys. Rev.*, D64:123522, 2001.

[95] T. W. B. Kibble. Topology of Cosmic Domains and Strings. *J. Phys.*, A9:1387–1398, 1976.

[96] T. W. B. Kibble. Some Implications of a Cosmological Phase Transition. *Phys. Rept.*, 67:183, 1980.

[97] T. W. B. Kibble. Phase transitions in the early universe. *Acta Phys. Polon.*, B13:723, 1982.

[98] Lloyd Knox and Lyman Page. Characterizing the peak in the cosmic microwave background angular power spectrum. *Phys. Rev. Lett.*, 85(7):1366–1369, Aug 2000.

[99] E. Komatsu et al. Five-Year Wilkinson Microwave Anisotropy Probe (WMAP1) Observations:Cosmological Interpretation. *Astrophys. J. Suppl.*, 180:330–376, 2009.

[100] E. Komatsu et al. Seven-Year Wilkinson Microwave Anisotropy Probe (WMAP) Observations: Cosmological Interpretation. 2010.

[101] Arthur Kosowsky. The Atacama Cosmology Telescope. *New Astron. Rev.*, 47:939–943, 2003.

[102] Arthur Kosowsky. The Atacama Cosmology Telescope Project: A Progress Report. *New Astron. Rev.*, 50:969–976, 2006.

[103] John Kovac et al. Detection of polarization in the cosmic microwave background using DASI. *Nature*, 420:772–787, 2002.

[104] Chao-lin Kuo et al. High Resolution Observations of the CMB Power Spectrum with ACBAR. *Astrophys. J.*, 600:32–51, 2004.

[105] Philip Lah et al. The HI content of star-forming galaxies at z = 0.24. *Mon. Not. Roy. Astron. Soc.*, 376:1357–1366, 2007.

[106] Louis Leblond and S. H. Henry Tye. Stability of D1-strings inside a D3-brane. *JHEP*, 03:055, 2004.

[107] Antony Lewis, Anthony Challinor, and Anthony Lasenby. Efficient Computation of CMB anisotropies in closed FRW models. *Astrophys. J.*, 538:473–476, 2000.

[108] Amy S. Lo and Edward L. Wright. Signatures of cosmic strings in the cosmic microwave background. 2005. astro-ph/0503120.

[109] A. N. Lommen. New limits on gravitational radiation using pulsars. 2002. Bad Honnef 2002, Neutron stars, pulsars and supernova remnants.

[110] Piero Madau, Avery Meiksin, and Martin J. Rees. 21-cm Tomography of the Intergalactic Medium at High Redshift. *Astrophys. J.*, 475:429, 1997.

[111] Joao Magueijo, Andreas Albrecht, David Coulson, and Pedro Ferreira. Doppler peaks from active perturbations. *Phys. Rev. Lett.*, 76:2617–2620, 1996.

[112] Joao C. R. Magueijo. Inborn metric of cosmic strings. *Phys. Rev.*, D46:1368–1378, 1992.

[113] C. J. A. P. Martins and E. P. S. Shellard. Fractal properties and small-scale structure of cosmic string networks. *Phys. Rev.*, D73:043515, 2006.

[114] P. D. Mauskopf et al. Measurement of a Peak in the Cosmic Microwave Background Power Spectrum from the North American test flight of BOOMERANG. *Astrophys. J.*, 536:L59–L62, 2000.

[115] M. P. McHugh, G. Zalamansky, F. Vernotte, and E. Lantz. Pulsar timing and the upper limits on a gravitational wave background: A Bayesian approach. *Phys. Rev.*, D54:5993–6000, 1996.

[116] J. J. McMahon, K. A. Aird, B. A. Benson, L. E. Bleem, J. Britton, J. E. Carlstrom, C. L. Chang, H. S. Cho, T. de Haan, T. M. Crawford, A. T. Crites, A. Datesman, M. A. Dobbs, W. Everett, N. W. Halverson, G. P. Holder, W. L. Holzapfel, D. Hrubes, K. D. Irwin, M. Joy, R. Keisler, T. M. Lanting, A. T. Lee, E. M. Leitch, A. Loehr, M. Lueker, J. Mehl, S. S. Meyer, J. J. Mohr, T. E. Montroy, M. D. Niemack, C. C. Ngeow, V. Novosad, S. Padin, T. Plagge, C. Pryke, C. Reichardt, J. E. Ruhl, K. K. Schaffer, L. Shaw, E. Shirokoff, H. G. Spieler, B. Stadler, A. A. Stark, Z. Staniszewski, K. Vanderlinde, J. D. Vieira, G. Wang, R. Williamson, V. Yefremenko, K. W. Yoon, O. Zhan, and A. Zenteno. SPTpol: an instrument for CMB polarization. In B. Young, B. Cabrera, & A. Miller, editor, *American Institute of Physics Conference Series*, volume 1185 of *American Institute of Physics Conference Series*, pages 511–514, December 2009.

[117] Diimitris Mitsouras, Robert H. Brandenberger, and Paul Hickson. Topological Statistics and the LMT Galaxy Redshift Survey. 1998. astro-ph/9806360.

[118] R. Moessner, L. Perivolaropoulos, and Robert H. Brandenberger. A Cosmic string specific signature on the cosmic microwave background. *Astrophys. J.*, 425:365–371, 1994.

[119] Thomas E. Montroy et al. A Measurement of the CMB Spectrum from the 2003 Flight of BOOMERANG. *Astrophys. J.*, 647:813–822, 2006.

[120] J. N. Moore and E. P. S. Shellard. On the evolution of abelian-Higgs string networks. 1998. hep-ph/9808336.

[121] Ali Nayeri, Robert H. Brandenberger, and Cumrun Vafa. Producing a scale-invariant spectrum of perturbations in a Hagedorn phase of string cosmology. *Phys. Rev. Lett.*, 97:021302, 2006.

[122] Holger Bech Nielsen and P. Olesen. Vortex-line models for dual strings. *Nucl. Phys.*, B61:45–61, 1973.

[123] M. D. Niemack et al. ACTPol: A polarization-sensitive receiver for the Atacama Cosmology Telescope. *Proc. SPIE Int. Soc. Opt. Eng.*, 7741:77411S, 2010.

[124] I. D. Novikov and Y. B. Zeldovic. Cosmology. *Ann. Rev. Astron. Astrophys.*, 5:627–649, 1967.

[125] Tauber, J. (on behalf of ESA and the Planck Science Collaboration). The planck mission. *Advances in Space Research*, 2004.

[126] L. Page et al. Three year Wilkinson Microwave Anisotropy Probe (WMAP) observations: Polarization analysis. *Astrophys. J. Suppl.*, 170:335, 2007.

[127] P. J. E. Peebles. Recombination of the Primeval Plasma. *Astrophys. J.*, 153:1, 1968.

[128] P.J.E. Peebles. *The Large-Scale Structure of the Universe*. Princeton Univ. Press, Princeton, (1980).

[129] U. Pen et al. 21 Cm Cosmography, An LRP White Paper. February 16, 2010.

[130] Ue-Li Pen, Uros Seljak, and Neil Turok. Power spectra in global defect theories of cosmic structure formation. *Phys. Rev. Lett.*, 79:1611–1614, 1997.

[131] Ue-Li Pen, Lister Staveley-Smith, Jeffrey Peterson, and Tzu-Ching Chang. First Detection of Cosmic Structure in the 21-cm Intensity Field. 2008.

[132] Arno A. Penzias and Robert Woodrow Wilson. A Measurement of excess antenna temperature at 4080- Mc/s. *Astrophys. J.*, 142:419–421, 1965.

[133] Leandros Perivolaropoulos. COBE versus cosmic strings: An Analytical model. *Phys. Lett.*, B298:305–311, 1993.

[134] Leandros Perivolaropoulos. Statistics of microwave fluctuations induced by topological defects. *Phys. Rev.*, D48:1530–1538, 1993.

[135] Leandros Perivolaropoulos. Spectral analysis of microwave background perturbations induced by cosmic strings. *Astrophys. J.*, 451:429–435, 1995.

[136] Leandros Perivolaropoulos, Robert H. Brandenberger, and Albert Stebbins. Dissipationless clustering of neutrinos in cosmic string induced wakes. *Phys. Rev.*, D41:1764, 1990.

[137] Francesco Piacentini et al. A measurement of the polarization-temperature angular cross power spectrum of the Cosmic Microwave Background from the 2003 flight of BOOMERANG. *Astrophys. J.*, 647:833–839, 2006.

[138] Levon Pogosian, S. H. Henry Tye, Ira Wasserman, and Mark Wyman. Observational constraints on cosmic string production during brane inflation. *Phys. Rev.*, D68:023506, 2003.

[139] Levon Pogosian, Ira Wasserman, and Mark Wyman. On vector mode contribution to CMB temperature and polarization from local strings. 2006. astro-ph/0604141.

[140] Levon Pogosian and Mark Wyman. B-modes from Cosmic Strings. *Phys. Rev.*, D77:083509, 2008.

[141] J. Polchinski. String theory. Vol. 1: An introduction to the bosonic string. Cambridge, UK: Univ. Pr. (1998) 402 p.

[142] Joseph Polchinski. Introduction to cosmic F- and D-strings. 2004. Cargese 2004, String theory: From gauge interactions to cosmology.

[143] Joseph Polchinski. Cosmic String Loops and Gravitational Radiation. 2007. Berlin 2006, Marcel Grossmann Meeting on General Relativity.

[144] Joseph Polchinski and Jorge V. Rocha. Analytic Study of Small Scale Structure on Cosmic Strings. *Phys. Rev.*, D74:083504, 2006.

[145] A. G. Polnarev. Polarization and Anisotropy Induced in the Microwave Background by Cosmological Gravitational Waves. *Sov. Astron.*, 29:607–+, December 1985.

[146] A. C. S. Readhead et al. Extended Mosaic Observations with the Cosmic Background Imager. *Astrophys. J.*, 609:498–512, 2004.

[147] M. J. Rees. Baryon concentration in string wakes at Z greater than about 200 - Implications for galaxy formation and large-scale structure. *Mon. Not. Roy. Astron. Soc*, 222:27P–32P, October 1986.

[148] C. L. Reichardt et al. High resolution CMB power spectrum from the complete ACBAR data set. *Astrophys. J.*, 694:1200–1219, 2009.

[149] Britt Reichborn-Kjennerud et al. EBEX: A balloon-borne CMB polarization experiment. 2010. arXiv:1007.3672.

[150] Christophe Ringeval, Mairi Sakellariadou, and Francois Bouchet. Cosmological evolution of cosmic string loops. *JCAP*, 0702:023, 2007.

[151] John E. Ruhl et al. The South Pole Telescope. *Proc. SPIE Int. Soc. Opt. Eng.*, 5498:11, 2004.

[152] Bertrand Russell. *The History of Western Philosophy.* New York, NY: Simon & Schuster Inc. (1945) 895.

[153] B. Ryden. Introduction to cosmology. San Francisco, USA: Addison-Wesley (2003) 244 p.

[154] R. K. Sachs and A. M. Wolfe. Perturbations of a Cosmological Model and Angular Variations of the Microwave Background. *Astrophys. J.*, 147:73–+, January 1967.

[155] R. K. Sachs and A. M. Wolfe. Perturbations of a cosmological model and angular variations of the microwave background. *Astrophys. J.*, 147:73–90, 1967.

[156] Mairi Sakellariadou. Cosmic Superstrings. *Phil. Trans. Roy. Soc. Lond.*, A366:2881–2894, 2008.

[157] Saswat Sarangi and S. H. Henry Tye. Cosmic string production towards the end of brane inflation. *Phys. Lett.*, B536:185–192, 2002.

[158] H. Sato. Galaxy formation by cosmic strings. *Prog. Theor. Phys.*, 75:1342, 1986.

[159] D. Scott and M. J. Rees. The 21-cm line at high redshift: a diagnostic for the origin of large scale structure. *"Mon. Not. Roy. Astron. Soc."*, 247:510–+, December 1990.

[160] Sara Seager, Dimitar D. Sasselov, and Douglas Scott. A New Calculation of the Recombination Epoch. *Astrophys. J.*, 523:L1–L5, 1999.

[161] Sara Seager, Dimitar D. Sasselov, and Douglas Scott. How exactly did the Universe become neutral? *Astrophys. J. Suppl.*, 128:407–430, 2000.

[162] Uros Seljak, Ue-Li Pen, and Neil Turok. Polarization of the Microwave Background in Defect Models. *Phys. Rev. Lett.*, 79:1615–1618, 1997.

[163] Uros Seljak and Anze Slosar. B polarization of cosmic microwave background as a tracer of strings. *Phys. Rev.*, D74:063523, 2006.

[164] Uros Seljak, Anze Slosar, and Patrick McDonald. Cosmological parameters from combining the Lyman-alpha forest with CMB, galaxy clustering and SN constraints. *JCAP*, 0610:014, 2006.

[165] Uros Seljak and Matias Zaldarriaga. A Line of Sight Approach to Cosmic Microwave Background Anisotropies. *Astrophys. J.*, 469:437–444, 1996.

[166] J. Silk and A. Vilenkin. Cosmic strings and galaxy formation. *Phys. Rev. Lett.*, 53:1700–1703, 1984.

[167] George F. Smoot et al. Structure in the COBE differential microwave radiometer first year maps. *Astrophys. J.*, 396:L1–L5, 1992.

[168] A. Sornborger, Robert H. Brandenberger, B. Fryxell, and K. Olson. The structure of cosmic string wakes. *Astrophys. J.*, 482:22–32, 1997.

[169] Andrew Sornborger, Bruce Fryxell, Kevin Olson, and Peter MacNeice. An Eulerian PPM & PIC Code for Cosmological Hydrodynamics. 1996. astro-ph/9608019.

[170] D. N. Spergel et al. Wilkinson Microwave Anisotropy Probe (WMAP) three year results: Implications for cosmology. *Astrophys. J. Suppl.*, 170:377, 2007.

[171] A. Stebbins. Cosmic strings and cold matter. *Astrophys. J. Lett.*, 303:L21–L25, April 1986.

[172] Albert Stebbins, Shoba Veeraraghavan, Robert H. Brandenberger, Joseph Silk, and Neil Turok. Cosmic String Wakes. *Astrophys. J.*, 322:1–19, 1987.

[173] Andrew Stewart and Robert Brandenberger. Edge Detection, Cosmic Strings and the South Pole Telescope. *JCAP*, 0902:009, 2009.

[174] R. A. Sunyaev and Ya. B. Zeldovich. Small scale fluctuations of relic radiation. *Astrophys. Space Sci.*, 7:3–19, 1970.

[175] J. A. Tauber, N. Mandolesi, J.-L. Puget, T. Banos, M. Bersanelli, F. R. Bouchet, R. C. Butler, J. Charra, G. Crone, J. Dodsworth, and et al. Planck pre-launch status: The Planck mission. *Astronomy & Astrophysics*, 520:A1+, September 2010.

[176] S. E. Thorsett and R. J. Dewey. Pulsar timing limits on very low frequency stochastic gravitational radiation. *Phys. Rev.*, D53:3468–3471, 1996.

[177] Jennie H. Traschen. Causal cosmological perturbations and implications for the sachs-wolfe effect. *Phys. Rev.*, D29:1563, 1984.

[178] Jennie H. Traschen. Constraints on stress energy perturbations in general relativitY. *Phys. Rev.*, D31:283, 1985.

[179] Jennie H. Traschen, N. Turok, and Robert H. Brandenberger. Microwave anisotropies from cosmic strings. *Phys. Rev.*, D34:919–930, 1986.

[180] Neil Turok and Robert H. Brandenberger. Cosmic Strings and the Formation of Galaxies and Clusters of Galaxies. *Phys. Rev.*, D33:2175, 1986.

[181] S. H. Henry Tye, Ira Wasserman, and Mark Wyman. Scaling of multitension cosmic superstring networks. *Phys. Rev.*, D71:103508, 2005.

[182] Tanmay Vachaspati. Cosmic Strings and the Large-Scale Structure of the Universe. *Phys. Rev. Lett.*, 57:1655–1657, 1986.

[183] Vitaly Vanchurin, Ken D. Olum, and Alexander Vilenkin. Scaling of cosmic string loops. *Phys. Rev.*, D74:063527, 2006.

[184] A. Vilenkin. Cosmological Density Fluctuations Produced by Vacuum Strings. *Phys. Rev. Lett.*, 46:1169–1172, 1981.

[185] A. Vilenkin. Gravitational Field of Vacuum Domain Walls and Strings. *Phys. Rev.*, D23:852–857, 1981.

[186] A. Vilenkin. Looking for cosmic strings. *Nature*, 322:613–+, August 1986.

[187] A. Vilenkin and E.P.S. Shellard. *Cosmic Strings and Other Topological Defects*. Cambridge Univ. Press, Cambridge, UK, (1994).

[188] Alexander Vilenkin. Cosmic Strings and Domain Walls. *Phys. Rept.*, 121:263, 1985.

[189] Alexander Vilenkin. Effect of small scale structure on the dynamics of cosmic strings. *Phys. Rev.*, D41:3038, 1990.

[190] Fabrizio Villa et al. The Planck Telescope. *AIP Conf. Proc.*, 616:224, 2002.

[191] Graham Vincent, Nuno D. Antunes, and Mark Hindmarsh. Numerical simulations of string networks in the Abelian- Higgs model. *Phys. Rev. Lett.*, 80:2277–2280, 1998.

[192] Martin J. White, John E. Carlstrom, and Mark Dragovan. Interferometric Observation of Cosmic Microwave Background Anisotropies. *Astrophys. J.*, 514:12, 1999.

[193] Edward Witten. Cosmic Superstrings. *Phys. Lett.*, B153:243, 1985.

[194] Edward L. Wright. Astronomy 275 lecture notes, spring 2009. http://www.astro.ucla.edu/ wright/cosmolog.htm.

[195] Mark Wyman, Levon Pogosian, and Ira Wasserman. Bounds on cosmic strings from WMAP and SDSS. *Phys. Rev.*, D72:023513, 2005.

[196] Matias Zaldarriaga and Uros Seljak. An All-Sky Analysis of Polarization in the Microwave Background. *Phys. Rev.*, D55:1830–1840, 1997.

[197] Ya. B. Zeldovich. Gravitational instability: An Approximate theory for large density perturbations. *Astron. Astrophys.*, 5:84–89, 1970.

[198] Ya. B. Zeldovich. Cosmological fluctuations produced near a singularity. *Mon. Not. Roy. Astron. Soc.*, 192:663–667, 1980.

[199] B. Zygelman. Hyperfine Level-changing Collisions of Hydrogen Atoms and Tomography of the Dark Age Universe. *Astrophys. J.*, 622:1356–1362, April 2005.